Analysis and Interpretation of Astrophysical Optical Emission-Line Spectra

Susan Ilani Loubser, B.Sc

Dissertation accepted in partial fulfilment of the requirements for the degree Master of Science in Physics at the North-West University

Supervisor: Prof. D.J. v d Walt

2005

Potchefstroom Campus

Abstract

This study consists of a quantitative optical emission-line analysis of spectra from five blue compact galaxies (Zw 0855, Mrk 1267, II Zw 33, Tol 2 & Tol 3), as well as a qualitative analysis of spectra from two galactic H II regions (NGC 3603 & NGC 3576). It serves a two-fold purpose: first, to understand the CCD reduction, spectra extraction and different nebular analysis methods, together with their applications and limitations, preparatory to studies using the Southern African Large Telescope (SALT) and second, to extend current star formation related research to include extragalactic starburst galaxies. The observations were carried out using the 1.9m telescope (equipped with a grating spectroscope and CCD detector) of the South African Astronomical Observatory (SAAO), during the period 1 to 7 March 2005. The necessary CCD data reduction, spectra extraction, wavelength and flux calibration, Doppler shift as well as reddening correction procedures were performed before the emission lines were identified and measured. A full nebular analysis, including temperature, density, metallicity (oxygen abundance) and other chemical abundance determinations, was performed on the blue compact galaxies (BCGs). Two different nebular analysis packages viz. `IRAF's nebular` and `SNAP` were used, with all the results well within the range of values expected for metal poor BCGs. Recommendations on the different methods and their applications are made.

Keywords: star formation, optical spectroscopy, emission-line spectra, blue compact galaxies, spectra reductions, nebular analysis.

Opsomming

Analise en interpretasie van astrofisiese optiese emissie-lyn spektra

Hierdie studie bestaan uit beide 'n kwantitatiewe optiese emissie-lyn analise op spektra van vyf blou-dwerg galaksies (Zw 0855, Mrk 1267, II Zw 33, Tol 2 & Tol 3), sowel as 'n kwalitatiewe analise op spektra van twee galaktiese H II gebiede (NGC 3603 & NGC 3576). Dit voldoen aan 'n tweevoudige oogmerk: eerstens om die CCD data reduksie, spektra-ekstraksie sowel as verskillende analise metodes vir warm gasnewels, tesame met hul toepassings en beperkinge, volledig te begryp hoofsaaklik ter voorbereiding van navorsingsprojekte op die Suider-Afrikaanse Groot Teleskoop (SALT), en tweedens dien dit ter uitbreiding van die huidige stervorming-verwante navorsing om ekstra-galaktiese stervormings-galaksies in te sluit. Die waarnemings is met die 1.9m teleskoop (toegerus met 'n roosterspektrograaf en 'n CCD kamera) van die Suid-Afrikaanse Astronomiese Observatorium (SAAO) te Sutherland, gedurende die periode 1 tot 7 Maart 2005, uitgevoer. Die nodige CCD data reduksie, spektra-ekstraksie, golflengte- en vloed-kalibrasie, Doppler verskuiwing sowel as uitdowingskorreksie prosedures is uitgevoer alvorens die emissie-lyne geidentifiseer en gemeet is. 'n Volledige analise is op die blou-dwerg galaksies uitgevoer en het die volgende behels: temperatuur, digtheid en metaal-inhoud bepalings asook die bepaling van die relatiewe voorkoms van chemiese elemente in die galaksies. Tydens hierdie analise is hoofsaaklik van twee sagteware pakkette, naamlik `nebular` ('n eksterne pakket in `IRAF`) en `SNAP`, gebruik gemaak en al die resultate stem ooreen met dit wat vir metaal-arm blou-dwerg galaksies verwag word. Ter afsluiting word verskeie aanbevelings oor die toepassing van die onderskeie metodes gemaak.

Sleutelwoorde: stervorming, optiese spektroskopie, emissie-lyn spektra, blou-dwerg galaksies, spektra reduksie prosedure, gasnewel-analise.

Acknowledgements

I wish to express my gratitude to the following persons and institutes:

Lecturers at the School of Physics of the North-West University who laid the foundation and who strengthened my fondness of astrophysics. Friends and students at the School of Physics who created an enlightening environment. I am also grateful to the School for the provision of financial resources.

The South African Astronomical Observatory (SAAO) for allocating the telescope time for this project. Stephen Potter of the SAAO whose assistance during the observations was indispensable. All the SAAO personnel for creating and facilitating learning opportunities and their readiness to help.

Conré Deale for his assistance with the observations.

Marshall McCall of York University for appropriation of his program, `SNAP`.

Peter Stocker for his kindness of tending to the spelling and grammar of this dissertation.

Faculty and students of the Vatican Observatory Summer School 2005 who broadened my horizons by introducing timely and interesting topics in astronomy, and the Vatican Observatory for making this voyage of discovery possible.

My mentor, Prof. Johan van der Walt, for his distinctive leadership and patience, and the selfless manner in which he placed his time and knowledge at my disposal.

My father, Jan, and sister, Ananka, pillars of strength.

In loving memory of my mother. She took a keen interest in this project.

Contents

Chapter 1

Introduction

This study has a two-fold purpose: (1) It is a continuation of observations and data reduction aimed at obtaining experience on CCD imaging and photometry as well as spectroscopy, in order to prepare for the Southern African Large Telescope (SALT) coming on line. (2) It is an extension of our current star formation related research to include extragalactic star formation regions such as starburst galaxies and metal poor blue compact galaxies (BCGs).

The optical emission-line spectra from these objects typically originate in hot photoionised gaseous nebulae and are used to determine various aspects of the gas as well as that of the high mass stars that provide the ionising photons. For example, line ratios can be used to derive densities, temperatures and optical depths while line profiles can be used to investigate the gas dynamics and the velocity field. Relative abundances of chemical elements, the star formation rates (SFRs) and initial mass functions of the star formation regions can also be inferred from these spectra.

To achieve this purpose, two high luminosity galactic H II regions viz. NGC 3603 and NGC 3576 as well as the blue compact (dwarf) galaxies Zw 0855 ($m_B \sim 14.5$), Mrk 1267 ($m_B \sim 14.5$), II Zw 33 ($m_B \sim 14.0$), Tol 2 ($m_B \sim 14.5$) and Tol 3 ($m_B \sim 13.3$) were observed, and the spectra were analysed to determine the physical conditions of these regions. BCGs contain gas clouds in which large numbers of hot stars are embedded, thus their spectra are similar to H II regions and can be treated using the same analysis methods.

1.1 Optical Astronomical Spectroscopy

1.1.1 Historical Background

Quantitative spectroscopy began with German optician Joseph von Fraunhofer. In 1814 he used a slit and a theodolite to produce a beam of sunlight, which was directed to fall onto a prism. This resulted in nearly 600 lines of the solar spectrum being discovered. These discoveries were not solely due to the use of a slit, but because he had developed a vastly improved way of casting glass; the prisms used were therefore better than any previously available. By 1823 Fraunhofer was able to measure wavelengths resulting in the mapping of 324 solar lines. He also labelled the nine most prominent lines, or groups of lines, with the capital letters of the alphabet and those lines are still to this day known as the Fraunhofer lines.

The solar spectrum was first photographed in 1842 by Alexandre Becquerel, and a decade later Jean Foucault demonstrated that light shone through a sodium flame contained dark lines coincident with the D lines in the solar spectrum. The next major development in understanding took a surprisingly long time after Fraunhofer's discoveries. It was not until 1859 that German physicist Gustav Kirchhoff, working with chemist Robert Bunsen, published the fundamental law of quantitative spectroscopy which we now know as Kirchhoff's law. This law states:

> *The ratio between the powers of emission and the powers of absorption for rays of the same wavelength is constant for all bodies at the same temperature.*

In modern mathematical terms,

$$\frac{\varepsilon_\lambda(T)}{\kappa_\lambda(T)} = B_\lambda(T) \tag{1.1}$$

(Dyson & Williams 1997), where $\varepsilon_\lambda(T)$ is the emission coefficient, $\kappa_\lambda(T)$ is the absorption coefficient of the substance at wavelength λ and temperature T. $B_\lambda(T)$ is the Planck function

$$B_\lambda(T) = \frac{2hc^2}{\lambda^5} \frac{1}{e^{hc/k\lambda T} - 1} \tag{1.2}$$

i.e. the radiation intensity from a black-body at temperature T, where h is Planck's constant, c the speed of light and k the Boltzmann constant.

To the fundamental law, we have the corollaries:

- *The wavelengths emitted by a substance depend upon that substance and its temperature,*
- *the absorption by a substance is a maximum at those wavelengths at which it tends to emit,*
- *a luminous solid or liquid (or a compressed gas) emits a continuous spectrum, whereas a gas gives a spectrum consisting of bright lines.*

With this new understanding, quantitative spectroscopy advanced rapidly.

Thereafter insights into all branches of spectroscopy came thick and fast with William Huggins, a self-taught amateur astronomer, making a remarkable series of discoveries by applying spectroscopy to astronomy. He observed some 70 nebulae in 1864, studied the composition of stars in 1866, and identified compounds of substances in comets. He also introduced an innovation, which almost every spectrograph from that day to this still incorporates, the ability to produce a comparison spectrum. This is a second spectrum produced by an artificial light source, the wavelengths of which are precisely known, and therefore the wavelengths of the object's lines may be found by comparison. In 1869 Norman Lockyer postulated the existence of an unknown element from the presence of its lines in the solar spectrum; this new element was named helium but it was not found on Earth for another three decades.

In addition to these astronomical discoveries big advances had been made in understanding the nature of atoms and hence of the physical processes underlying the production of spectra. These developments included the Balmer empirical law to predict the wavelengths of hydrogen lines in the visible spectrum, Sommerfeld's extension of Bohr's model, quantum mechanics, Pauli's exclusion principle, understanding the effects of ionisation, explaining molecular spectra and the explanation of the Zeeman effect.

While these developments in the observation and understanding of the optical spectrum were progressing, elsewhere the concept of the spectrum was being extended. In 1860 James Clerk Maxwell produced his theory predicting the properties of radiation associated with electrical and electromagnetic phenomena. In this theory, light becomes only a small component of the full spectrum, which stretches from X- and gamma rays towards microwaves and radio waves. The nature of the interaction of electromagnetic radiation with matter, varies with wavelength, even though there is no change in the fundamental nature of radiation. Thus simplistically, in the optical region we

are concerned primarily with electronic transitions in atoms and molecules. At longer wavelengths we have a direct induction of current in conductors as well as rotational and vibrational transitions in molecules, while at short wavelengths the interactions are with the inner electrons of atoms and their nuclei. The latter interactions were much less accessible than those in the optical region thus slowing the development of spectroscopy outside the optical region.

The fundamental spectroscopic techniques of interest to astronomers are atomic and molecular absorption, emission spectroscopy and fluorescence spectroscopy. The spectral properties of solids are of interest within the solar system and for the study of the interstellar medium (ISM).

1.1.2 Modern Nebular CCD Spectroscopy

Spectrophotometry of absorption and emission lines is the principal observational tool used for studying the physical conditions and compositions of stars, galaxies and gaseous nebulae. The development of low-noise charge coupled device (CCD) detectors in recent years converge towards the ideal detector for astronomical spectroscopy. The high quantum efficiency, linear and reproducible response, large dynamic range and panoramic format make the CCD the ideal detector for astronomical spectroscopy at low and high spectral resolution.

Ionised gases, referred to as gaseous nebulae, are ubiquitous in the Universe. They appear as H II regions wherever massive stars are forming and as planetary nebulae or supernovae remnants where stars are dying. They are also harboured in active galactic nuclei and quasars. Not only are they common but they are visible out to the furthest reaches of the Universe. The spectra can be used to answer fundamental questions about galaxy formation and evolution. With CCD detectors, it has become possible to spatially map the distribution of emission across a nebula in one dimension with a long slit and more recently in two dimensions with multiple slits, optical fibres or micro-lenses. The combination of spectral multiplexing with spatial mapping in two dimensions has led to unprecedented amounts of data and will continue to do so.

1.2 The Purpose of This Study

SALT (due to be fully operational November 2005) is currently the largest optical telescope in the southern hemisphere and one of the largest in the world. The spectroscopic study of the Universe is described as the main

objective of this world-class instrument. It is therefore of utmost importance to become conversant with the basic methods of astronomical spectroscopy to ensure the successful and optimal use of this new telescope.

Thus, the underpinning aim of this project is to master the basic methods and techniques of astronomical, optical spectroscopy preparatory to studies with SALT. All the way through, priority was given to obtaining, reducing and analysing CCD spectra, first hand, in the most optimal manner. It is imperative that these basic methods, together with their applications as well as limitations, are fully mastered before attempting to solve real scientific questions. This constituted the chief purpose of this study. The secondary purpose, namely to extend current star formation related research, gave the motivation for the choice of sources: two galactic H II regions and five extragalactic BCGs.

Chapter 2 consists of a theoretical background study of these diffuse objects and their spectra. The methods to determine the temperature, density, metallicity and chemical abundances of nebulae from their characteristic emission-line spectra are investigated. A brief introduction to the determination of the SFR of BCGs is also given.

Chapter 3 contains a description of the instrumentation used and the procedures followed during the observation of the sources using the 1.9m telescope of the South African Astronomical Observatory (SAAO) during the period 1 to 7 March 2005. This is followed by a detailed account of the data reduction and spectra extraction processes that were performed. Wavelength and flux calibration procedures are described, as well as the standard star spectra and sky spectra being presented.

Chapter 4 deals with the corrections made to the BCG spectra, in particular the reddening correction and Doppler shift correction, as well as the measurement and identification of the emission lines. This is followed by a discussion of the individual objects and the presentation of their spectra. This chapter also contains the nebular analysis which consists of the temperature, density, metallicity and chemical abundance calculations.

Chapter 5 is where conclusions and recommendations are stated and completes this study.

Chapter 2

Theoretical Background

Chapter 2 consists of two main sections. Section 2.1 introduces H II regions, their morphology and spectra and contains the theoretical description of the methods used to determine temperatures, densities, metallicities and chemical abundances of diffuse nebulae. Section 2.2 introduces BCGs and their spectra. BCGs, as extragalactic H II regions, are a subclass of diffuse nebulae and as a result, all of the methods described in section 2.1 can be applied to them. In addition, the SFR of BCGs can be determined from their optical spectra; this is also described in section 2.2.

2.1 H II Regions

In recent years, deep spectroscopic studies, coupled with new theoretical results in atomic physics, have cast new light on a well-established field of modern astrophysics — the study of elemental abundances in H II regions. An accurate knowledge of abundances in galactic and extragalactic H II regions is of paramount importance for constraining galactic chemical evolution models. Observations of H II regions provide accessible and important probes of physical conditions in other galaxies. They furnish information about the ISM from which they are formed, as well as the high-mass stars to which they give birth.

2.1.1 Morphology

Hydrogen atoms in an interstellar gas cloud located near a very hot star, for example a newborn O or B star, will be exposed to outpouring of ultraviolet (UV) radiation from such a star. UV photons with energy equal to 10.2 eV (or wavelength equal to 1216 Å) can excite hydrogen atoms from the 1s

energy state into the 2p energy state. UV photons with energies greater than the Lyman limit (energy greater than 13.6 eV or wavelength shorter than 912 Å) can ionise the hydrogen atoms, with the excess photon energy above the energy of the Lyman limit contributing to the kinetic energy of the freed electron.

Wien's[1] displacement law for thermal radiation states that: if the temperature, T, of a black-body increases, the peak of the emission spectrum shifts towards shorter wavelengths (higher energies). In particular, the wavelength of maximum emission λ_{max} shifts with changing temperature according to the law:

$$\lambda_{max} T = 3 \times 10^7 \text{ Å K} \tag{2.1}$$

Therefore, O and B stars (with typical temperatures in the range 11 000 K to 40 000 K) have large fluxes of photons with sufficient energy to ionise hydrogen atoms. In particular, stars with $T > 33\,000$ K have their maximum emission in the wavelength range shorter than 912 Å.

An H II region is a region of interstellar hydrogen that is ionised. Each ionised hydrogen atom contributes two particles to the gas, namely a proton and an electron. These hot regions are usually found around massive young O and B stars, the strong UV light from which ionises the gas, causing it to shine. The Roman numeral II distinguishes once-ionised hydrogen, H II, from neutral atomic hydrogen, H I. Inside the H II region, the hydrogen plasma is constantly trying to recombine to form neutral hydrogen atoms but the plasma is kept almost completely ionised by the continued outpouring of UV photons from the central source. The part of the H II region where the UV output of the central star is able to keep a balance between recombination and ionisation is called the Stromgren sphere. This is after Bengt Stromgren who showed that the division between H I and H II is quite sharp if the surrounding gas cloud is so massive that all the UV photons from the central stars are used up before the H II region can encompass the entire cloud.

The size of a spherically symmetrical ionisation-bounded nebula (as the Stromgren sphere), can be found by equating the total number of recombinations to the total emission rate of ionising photons from the central star(s):

$$\frac{4}{3}\pi R^3 \epsilon N_e N_p \alpha(T_e) = Q(N, T_{eff}, L) \tag{2.2}$$

where the fraction ϵ of the volume has a uniform electron density N_e, and proton density $N_p \simeq N_e$. The recombination coefficient is α, which is a slowly varying function of the electron temperature T_e, and the rate Q of ionising photon production by the embedded star(s) is a function of their number N,

[1] German physicist Wilhelm Wien (1864-1928).

effective temperature and luminosity L (Pagel 1997). The production rate of ionising photons is a function of luminosity and thus a function of the mass of the ionising stars by the mass-luminosity relation. For stars less than $0.4M_{\odot}$, that are fully convective, the luminosity varies as the square of its mass. For stars of mass similar to or slightly less than the Sun, the luminosity is approximately proportional to the mass raised to the fifth power. For more massive stars, the luminosity varies approximately as the mass cubed (Taylor 1994).

Optical H II regions have densities which range from 10 to 10^3 cm^{-3} (Shu 1982). Lower-density H II regions do exist but the low emission of diffuse H II regions make them difficult to observe. Higher-density H II regions have also been inferred to exist but the large obscuration due to the dust that usually accompanies compact H II regions makes them difficult to observe optically. The chemical composition of galactic H II regions turns out to be similar to that of Population I stars. This agrees with the evidence that indicates that most newborn stars are formed out of gas with the same chemical composition as that which now surrounds the O and B stars in H II regions. H II regions in our Galaxy are strongly concentrated to the galactic plane, because except for the nearest, they all lie in the disc. The disc defines where the galactic equator is. External H II regions in observed galaxies are concentrated toward the spiral arms of these galaxies.

2.1.2 The Spectra of Nebulae

Emission Lines

The basic optical spectrum of hot nebulae, such as H II regions, is that of an emission-line spectrum. The strongest of the emission lines, however are the forbidden lines, such as [O III]$\lambda\lambda$4959, 5007 and λ4363.[2] The ground state configuration of an atom may give rise to more than one term (a configuration is the arrangement of electrons in an atom and a term is a set of values of L, S and J, with L being the orbital angular momentum, S the spin angular momentum and J the total angular momentum). If one of the upper terms of the ground state is excited, a radiative transition may be made to the ground term but this will be a forbidden electric dipole transition, since $\Delta l = 0$ (an emitted photon carries off angular momen-

[2]These lines were once attributed to an unknown element "nebulium" before they were identified by Ira S. Bowen in 1928.

The standard notation is used, where the ion identification is written between two square brackets for forbidden lines and a square bracket to the right of the ion identification for a semi-forbidden line.

tum and this requires at least one electron to change its angular momentum, giving rise to the selection rule $\Delta l = \pm 1$). In the laboratory such an excited term will be collisionally de-excited long before there is time for a forbidden radiative decay but under the low density conditions in a nebula where collisional de-excitations are rare, the forbidden line may be seen. Since the terms of the ground state are not very far apart in energy, collisional excitation of the upper terms of the ground state are relatively easy and the subsequent photons produced by the forbidden downward transitions might lie in the visible. Examples include the $^2D \rightarrow {}^4S$ transition in O II which produces the [O II]$\lambda\lambda$3726, 3729 doublet. Similarly, O III has the ground state configuration $1s^2 2s^2 2p^2$ and the two outer p electrons give rise to the terms ^1S, ^1D and ^3P in order of decreasing excitation energy. Fine-structure splitting divides the lowest term into levels $^3P_2$, $^3P_1$ and $^3P_0$ (see Figure 2.1). The transitions $^1D_2 \rightarrow {}^3P_2$ and $^1D_2 \rightarrow {}^3P_1$ produce the doublet [O III]$\lambda\lambda$4959, 5007 (J=2 $\rightarrow$ J=0 is additionally forbidden by the selection rule ΔJ=0,$\pm$1).

The main excitation mechanism, in the case of forbidden lines, is that of collisions between the electrons with ground-level ions. Once excited, an atom will quickly cascade back towards its ground level through allowed radiative transitions. However, if a metastable level exists (an energy level with only forbidden transitions down to lower energy levels) then the electron may become trapped at that level. Since all excitation mechanisms, including collisions, which would enable the electron to escape from the metastable level by a transition to a higher level are very rare, over time the population of the metastable level can become large compared to its Local Thermodynamic Equilibrium (LTE) value (as determined by the Boltzmann equation). The forbidden lines may thus become the strongest lines in the spectrum. The transitions which then take place are the much slower magnetic dipole or electric quadrupole transitions (transition rates of typically 1 s^{-1} compared to 10^8 s^{-1} for electric dipole transitions (Dyson & Williams 1997)).

In the ordinary optical region, all of the collisionally excited lines in the spectra of gaseous nebulae are forbidden lines, with the other characteristic features being the recombination lines. Thus, the permitted emission lines arise from recombination in atoms or ions without metastable levels to trap the electrons and are predominantly produced by hydrogen and helium (Osterbrock 1989)[3]. In comparison, the permitted emission arising from cascades following recombination tends to be extremely weak. Cross-sections are such

[3]In H I, He I and He II there are metastable levels, but they do not usually affect the recombination spectrum by much. The H and He recombination lines are usually the strongest recombination lines in a spectrum simply because of their abundance relative to other elements.

that a free electron colliding with a heavy ion is more likely to collisionally excite the ion than it is to recombine with it. A few lines of doubly ionised nitrogen and oxygen arise through selective fluorescence. This latter process occurs when a line from one element coincides with a strong emission line from another. The upper level of the first element becomes overpopulated through absorption of the emission-line photons and in turn produces the emission lines as the electrons cascade back to the ground state. The UV emission lines such as Lyman-α, are frequently the precursors in this process.

Recombination leads to a process whereby a gas cloud surrounding a hot bright star or a group of such stars, can shine in the visual part of the spectrum. The radiative recombination of a proton and an electron might form an excited state of neutral hydrogen, which subsequently cascades to the ground state by the emission of additional photons. As gaseous nebulae are so rarefied and the radiative processes are so efficient, the vast majority of hydrogen atoms are in the ground electronic state.

The balance of ionisation and recombination in H II regions leads to a heating of the hydrogen plasma (a result of the excess energy the liberated electrons carry in the form of kinetic energy), which in turn yields additional radiation processes. In a steady state, this heat input is balanced by the following heat output. The thermal distributions of electrons and ions suffer continual collisions. A fraction of such collisions are inelastic and raise an incompletely ionised atom or ion (see Tables 2.4 and 2.5 for the ionisation energy required to fully ionise some of the ions), like say singly or doubly ionised oxygen, to an exited electronic state. These atoms may de-excite radiatively by the emission of a photon. This line photon may be free to leave the system because the absorption cross-section (and hence the chance of it being reabsorped) is very small. The mean free path of the photon is much greater than the size of the nebula. The loss of its energy constitutes a net cooling of the region. The balance of heating and cooling leads to an equilibrium temperature of about 10^4 K for galactic H II regions. Such a temperature is two orders of magnitude greater than the approximately 10^2 K characteristic of H I regions which do not have access to the ionising radiation of hot bright stars.

The integrated fluxes of the emission lines can be measured and used to determine the temperature, density, internal reddening of emission-line regions, as well as the element abundances. Emission-line fluxes are not only the primary tracers of the SFRs but they also provide the various metallicity indices of these regions. For example, the index

$$R_{23} = \frac{I([\text{O II}]\lambda 3727) + I([\text{O III}]\lambda\lambda 4959, 5007)}{I(\text{H}\beta)} \tag{2.3}$$

introduced by Pagel et al. (1979), and the ratio

$$\frac{I([\text{N II}]\lambda 6583)}{I([\text{O II}]\lambda 3727)} \tag{2.4}$$

can be used to derive the metallicity of these star formation regions, as illustrated later in this study.

Absorption Lines

The equivalent widths of absorption lines and the continuum colours provide information about the stellar populations and physical parameters of nebulae. It is convenient to define this property, an equivalent width (EW) for the line, which measures the net flux removed from the incident beam by the absorption line, using:

$$EW = \int_0^\infty depth\, d\lambda \tag{2.5}$$

$$EW = \int_0^\infty \frac{F_C - F_\nu}{F_C} d\lambda = -\frac{\lambda^2}{c} \int_0^\infty \frac{F_C - F_\nu}{F_C} d\nu \tag{2.6}$$

where F_ν is the flux in the line at frequency ν and F_C is the flux at the neighbouring continuum point and for a wavelength λ and speed of light c, $d\nu = (-c/\lambda^2)d\lambda$ (Emerson 1997). The line occupies such a small proportion of the frequency range from 0 to ∞ that λ^2 can be taken out of the integral. This quantity is useful because it can be measured even when the spectrograph used to observe it does not have the resolution needed to resolve the details of the actual line profile. Equivalent widths for emission lines can be measured in a similar manner and the method used to measure EWs in this study is described in chapter 4.

Window (Å)	Main Absorber	Identification
3908-3952	Ca II, K	Ca, K
3952-3988	Ca II, H+Hϵ	Ca, H
4082-4124	Hδ	Hδ
4150-4214	CN	CN
4284-4318	G Band	G Band
5156-5196	MgI+ MgH	Mg
5880-5914	NaI	NaI

Table 2.1: Absorption lines.

The absorption spectrum of a nebula is produced by the sum of the spectral characteristics of its stellar content. Observations of the integrated spectra of extragalactic H II regions can be used to determine the distribution in age and metal abundance of the stellar population in these systems and hence to determine their epoch of formation and subsequent star formation history. To this aim, some strong, easily identified absorption features can be measured, which should include some age and metallicity sensitive absorption features. Examples of such lines are shown in Table 2.1 taken from Kong et al. (2002b).

As well as the absorption features, the 4000 Å Balmer break can also be measured. It is the strongest discontinuity in the optical spectrum of a galaxy and arises because of the accumulation of a large number of spectral lines in a narrow wavelength region. The main contribution to the opacity comes from ionised metals. In hot stars, the elements are multiply ionised and the opacity decreases, so the 4000 Å break will be small for young stellar populations and large for old metal-rich galaxies.

2.1.3 The Electron Temperature

A fundamental parameter for the derivation of all other physical and chemical quantities in a photoionised diffuse plasma is the electron temperature (hereafter referred to as temperature), since virtually all the observables are strong functions of temperature. It should be noted that the radiation field from an emission nebula may not be characterised by a single temperature, as it can be composed of light from more than one distant source (such as the stars in an OB association), as well as diffuse radiation emitted by the gas itself. As a result the gas is not in LTE and populations of energy levels are not described by a Boltzmann distribution, therefore, at any instant, most of the ions are in the ground state. The Saha, Boltzmann and Maxwell equations are therefore inapplicable. Nonetheless, it is still possible to determine temperatures and densities for the material in hot nebulae from their spectra.

There exists various methods that can be used to determine the temperature from astronomical spectra, three of these methods are described below.

Method 1: Collisional Excitation Method

The most common means of estimating the electron temperature uses two emission lines of the same element which have different thresholds for collisional excitation. For example, the temperature can be found from the

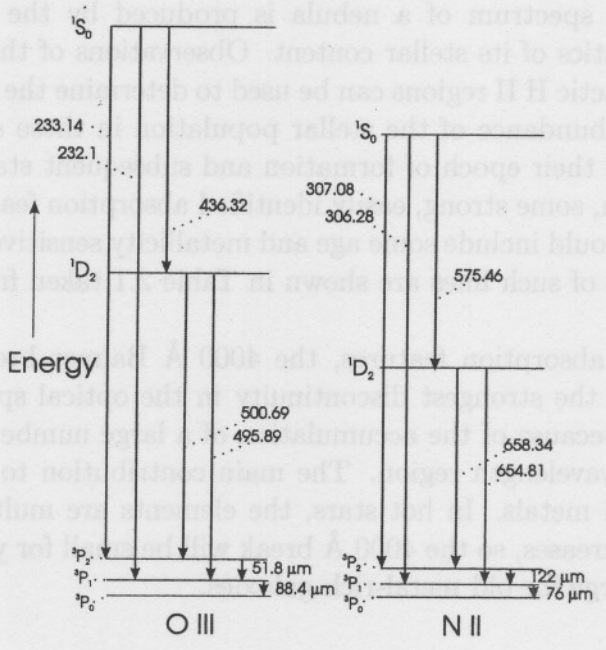

Figure 2.1: Energy level diagrams of the terms in the $2p^2$ ground state configuration of O III and N II. Optical wavelengths are in nm, infrared transitions in μm. Figure obtained from Emerson (1997).

oxygen and nitrogen optical forbidden emission-line intensities[4]. These diagnostic line ratios are derived from the observed line fluxes and must be corrected for interstellar reddening. The reddening corrected line flux I is derived from the observed line flux F by

$$I(\lambda) = F(\lambda) \times 10^{-cf_\lambda} \tag{2.7}$$

where c is an extinction constant. The extinction function f_λ can be taken from a few possible known extinction functions (the choices of different galactic and extragalactic extinction functions are summarised in Shaw & Dufour (1995)). In this study, the reddening corrected line fluxes were derived from the observed line fluxes by applying the interstellar reddening correction by Cardelli, Clayton & Mathis (1989). This procedure is fully described in chapter 4.

[4]Although the temperature and density are found from the emission-line intensities, line fluxes can be used for this purpose since the ratio of two line fluxes will be the same as the ratio of two line intensities. Thus, the symbol I is used for line fluxes to concur with standard notation.

Estimations of kinetic temperatures from line ratios make use of the fact that the relative collisional excitation rates of levels with considerably different excitation potentials are strongly dependent on temperature. The following derivation is done following the discussion in Emerson (1997), Dopita & Sutherland (2003) as well as Osterbrock (1989).

To understand how temperature can be estimated from the collisional excitation by electron impact consider the O III and N II configurations in Figure 2.1, which has ^3P as the ground state, the term ^1D as the first excited state and the ^1S term as the second excited state. The excited states can radiate back down to the lower states. Electron impacts can collisionally excite an atom into an upper level. Once there, if left alone, it will return to a lower state by a radiative transition. If, on the other hand, it suffers another collision with an electron while still in the excited state, it may collisionally de-excite back down to a lower state. The most conveniently observed transitions (in the visible for O III and N II) are $^1S_0$ to $^1D_2$ and the doublet $^1D_2$ to $^3P_2$ and $^3P_1$. These three are all forbidden electric dipole transitions. Singlet to doublet transitions are additionally forbidden because they break the weak rule $\Delta S = 0$, and $^1D_2 \rightarrow {}^3P_0$ is much weaker than its two companion transitions because $\Delta J = 2$ and can be neglected in what follows. The definition of a line intensity is

$$I_\nu = \frac{A_{ji}}{4\pi} h\nu \int N_j \, dx \tag{2.8}$$

where ν is the frequency, h is Planck's constant, N_j is the density in level j, dx is along the line of sight and A_{ji} is the Einstein probability for spontaneous emission. The integral represents a column density with units cm^{-2}. With this definition, the ratio of these transitions can be written as

$$\frac{I(^1S \rightarrow {}^1D)}{I(^1D \rightarrow {}^3P_2) + I(^1D \rightarrow {}^3P_1)} = \frac{N(^1S)A(^1S \rightarrow {}^1D)h\nu(^1S \rightarrow {}^1D)}{N(^1D)A(^1D \rightarrow {}^3P)h\nu(^1D \rightarrow {}^3P)} \tag{2.9}$$

First, suppose the electron density is low so that collisional de-excitation from ^1D and ^1S can be neglected, as can collisional excitation from ^1D to ^1S. Suppose also that the population of ^1D due to radiative decays from ^1S is unimportant. In statistical equilibrium, the rate of population of a level by the combination of radiative and collisional processes exactly balances the rate of de-population by such processes. The equations of statistical equilibrium then give

$$N(D)A(D \rightarrow P) = N(P)C(P \rightarrow D) \tag{2.10}$$

$$N(S)[A(S \rightarrow P) + A(S \rightarrow D)] = N(P)C(P \rightarrow S) \tag{2.11}$$

with A being the Einstein probability for spontaneous emission and C the rate of collisional excitation.[5]

Then

$$\frac{N(S)}{N(D)} = \frac{C(P \to S)}{C(P \to D)} \frac{A(D \to P)}{A(S \to P) + A(S \to D)} \tag{2.12}$$

which, when substituted in (2.9) delivers

$$\frac{I(S \to D)}{I(D \to P)} = \frac{C(P \to S)}{C(P \to D)} \frac{\nu(S \to D)}{\nu(D \to P)} \frac{A(S \to D)}{A(S \to P) + A(S \to D)} \tag{2.13}$$

The collisional excitation rate is given by

$$C \propto 8.6 \times 10^{-12} N_e \frac{\Omega}{g} \frac{e^{-E/kT}}{T^{1/2}} \tag{2.14}$$

where the statistical weight $g = 2J + 1$, k is the Boltzmann constant and Ω is the collision strength (an integral with respect to E of the cross section σ, i.e. $\Omega \propto \int \sigma(E)\, dE$). With this definition, the intensity ratio becomes

$$\frac{I(S \to D)}{I(D \to P)} = \frac{\Omega(P \to S)}{\Omega(P \to D)} e^{-\Delta E/kT} \frac{g_D}{g_S} \frac{\nu(S \to D)}{\nu(D \to P)} \frac{A(S \to D)}{A(S \to P) + A(S \to D)} \tag{2.15}$$

with $\Delta E = E(S) - E(D)$. Thus, measurement of the line ratio will provide a value for the kinetic temperature.

In the case of high electron density N_e, collisional de-excitation will be important as well as collisional excitation from ^1D to ^1S. Following the same reasoning as in the simplified method above but incorporating this into the derivation gives the equations of statistical equilibrium as

$$N(P)C_{PD} + N(S)[C_{SD} + A_{SD}] = N(D)[C_{DS} + C_{DP} + A_{DP}] \tag{2.16}$$

$$N(P)C_{PS} + N(D)C_{DS} = N(S)[C_{SD} + C_{SP} + A_{SD} + A_{SP}] \tag{2.17}$$

where the notation was changed from $Z(X \to Y)$ to Z_{XY} for the sake of compactness.

Hence

$$\frac{N(S)}{N(D)} = \frac{\left[\{C_{DS} + C_{DP} + A_{DP}\}\frac{C_{PS}}{C_{PD}} + C_{DS}\right]}{\left[C_{SD} + C_{SP} + A_{SD} + A_{SP} + \frac{\{C_{SD}+A_{SD}\}C_{PS}}{C_{PD}}\right]} \tag{2.18}$$

[5]The Einstein B probabilities for stimulated emission and for absorption are very small for these collisionally excited lines and are not taken into account. Transitions to the ground state generally do not stimulate the excitation of other ions in that state because oscillator strengths are too small.

Substituting the collisional excitation rate, while setting $r = 8.6\times10^{-12}N_e/T^{\frac{1}{2}}$ and removing C_{PS}/C_{PD} from the square brackets, the equation becomes

$$\frac{N(S)}{N(D)} = \frac{\Omega_{PS}e^{-\Delta E/kT}\left[A_{DP} + \frac{r}{5}\{\Omega_{PD} + \Omega_{DS}e^{-\Delta E/kT} + \frac{\Omega_{DS}\Omega_{PD}}{\Omega_{PS}}\}\right]}{\Omega_{PD}\left[A_{SP} + A_{SD} + A_{SD}\frac{\Omega_{PS}}{\Omega_{PD}}e^{-\Delta E/kT} + r\{\Omega_{PS} + \Omega_{DS} + \Omega_{DS}\frac{\Omega_{PS}}{\Omega_{PD}}e^{-\Delta E/kT}\}\right]} \tag{2.19}$$

where $g_D = 5$ and $g_S = 1$ was used.

This gives the line intensity ratio as

$$\frac{I_{SD}}{I_{DP}} = I_R\frac{\left[1 + \frac{r}{5A_{DP}}\{\Omega_{PD} + \Omega_{DS}e^{-\Delta E/kT} + \Omega_{DS}\frac{\Omega_{PD}}{\Omega_{PS}}\}\right]}{\left[1 + \frac{A_{SD}}{A_{PS}+A_{SD}}\frac{\Omega_{PS}}{\Omega_{PD}}e^{-\Delta E/kT} + \frac{r}{A_{SP}+A_{SD}}\{\Omega_{PS} + \Omega_{DS} + \Omega_{DS}\frac{\Omega_{PS}}{\Omega_{PD}}e^{-\Delta E/kT}\}\right]} \tag{2.20}$$

with

$$I_R = \frac{\Omega_{PS}}{\Omega_{PD}}\frac{\nu_{SD}}{\nu_{DP}}e^{-\Delta E/kT}\frac{A_{SD}}{A_{SP} + A_{SD}} \tag{2.21}$$

Then, if the terms with $e^{-\Delta E/kT}$ inside the square brackets can be neglected, the ratio becomes

$$\frac{I_{SD}}{I_{DP}} = \frac{\Omega_{PS}}{\Omega_{PD}}\frac{\nu_{SD}}{\nu_{DP}}e^{-\Delta E/kT}\frac{A_{SD}}{A_{SP} + A_{SD}}\frac{\left[1 + \frac{r}{5A_{DP}}\Omega_{PD}(1 + \frac{\Omega_{DS}}{\Omega_{PS}})\right]}{\left[1 + r\frac{(\Omega_{PS}+\Omega_{DS})}{A_{SP}+A_{SD}}\right]} \tag{2.22}$$

Thus at high electron densities, an electron density dependence (via r) appears in the ratio. If N_e is known, for example from a density sensitive line ratio, then the temperature can be computed.

Consider the two main applications of (2.22) to the [O III] and [N II] forbidden lines (all atomic data from Emerson (1997) except the A-value for [O III]λ2331 which is from Osterbrock (1989)).

For [O III]:

[O III]				
$^1S_0 \rightarrow {}^1D_2$	4363 Å	A_{SD}=1.8 s^{-1}		$\Omega_{DS} = 0.62$
$^1D_2 \rightarrow {}^3P_2$	5007 Å	$A = 2.0 \times 10^{-2}$ s^{-1}		
$^1D_2 \rightarrow {}^3P_1$	4959 Å	$A = 6.7 \times 10^{-3}$ s^{-1}	$A_{DP} = 2.67 \times 10^{-2}$ s^{-1}	$\Omega_{PD} = 2.17$
$^1S_0 \rightarrow {}^3P_2$	2331 Å	$A = 7.8 \times 10^{-4}$ s^{-1}		
$^1S_0 \rightarrow {}^3P_1$	2321 Å	$A = 2.2 \times 10^{-1}$ s^{-1}	$A_{SP} = 2.21 \times 10^{-1}$ s^{-1}	$\Omega_{PS} = 0.28$

Table 2.2: Atomic data for [O III].

For [N II]:

[N II]				
$^1S_0 \rightarrow {}^1D_2$	5755 Å	$A_{SD} = 1.1\ \mathrm{s}^{-1}$		$\Omega_{DS} = 0.41$
$^1D_2 \rightarrow {}^3P_2$	6583 Å	$A = 3.0 \times 10^{-3}\ \mathrm{s}^{-1}$	$A_{DP} = 4.00 \times 10^{-3}\ \mathrm{s}^{-1}$	$\Omega_{PD} = 2.68$
$^1D_2 \rightarrow {}^3P_1$	6548 Å	$A = 1.0 \times 10^{-3}\ \mathrm{s}^{-1}$		
$^1S_0 \rightarrow {}^3P_2$	3071 Å	$A = 1.5 \times 10^{-4}\ \mathrm{s}^{-1}$	$A_{SP} = 3.42 \times 10^{-2}\ \mathrm{s}^{-1}$	$\Omega_{PS} = 0.35$
$^1S_0 \rightarrow {}^3P_1$	3063 Å	$A = 3.4 \times 10^{-2}\ \mathrm{s}^{-1}$		

Table 2.3: Atomic data for [N II].

Thus, for [O III]:

$$\frac{I(4363)}{I(5007)+I(4959)} = 0.1316e^{-32990/T}\frac{[1+4.49\times10^{-10}\frac{N_e}{T^{1/2}}]}{[1+3.83\times10^{-12}\frac{N_e}{T^{1/2}}]} \tag{2.23}$$

where the square bracket in the denominator can be neglected except at very high electron densities or very low temperatures.

For [N II]:

$$\frac{I(5755)}{I(6583)+I(6548)} = 0.1447e^{-25010/T}\frac{[1+2.50\times10^{-9}\frac{N_e}{T^{1/2}}]}{[1+5.78\times10^{-12}\frac{N_e}{T^{1/2}}]} \tag{2.24}$$

where the square bracket in the denominator can once again be neglected except at very high electron densities or very low temperatures.

These equations are usually used in the following form:

$$\frac{I(5007)+I(4959)}{I(4363)} = 7.6e^{32990/T}\left[1+4.49\times10^{-10}\frac{N_e}{T^{1/2}}\right]^{-1} \tag{2.25}$$

and

$$\frac{I(6583)+I(6548)}{I(5755)} = 6.91e^{25010/T}\left[1+2.50\times10^{-9}\frac{N_e}{T^{1/2}}\right]^{-1} \tag{2.26}$$

The above, together with other diagnostic line ratios are given in Table 2.4. The table lists the ion, spectrum designation, diagnostic line ratio and the ionisation potential of the ion. The line ratios are given as $I(\lambda_1)/I(\lambda_2)$, where λ_1 and λ_2 are in units of Å. All the ratios in this table involve sums of line strengths and are indicated as $I(\lambda_1+\lambda_2)/I(\lambda_3+\lambda_4)$.

Ion	Spectrum	Line Ratio	Ionisation Potential (eV)
O^0	[O I]	I(6300+6363)/I(5577)	—
S^+	[S II]	I(6716+6731)/I(4068+4076)	10.4
O^+	[O II]	I(3726+3729)/I(7320+7330)	13.6
N^+	[N II]	I(6548+6583)/I(5755)	14.5
Si^{+2}	Si III]	I(1883+1892)/I(1206)	16.3
S^{+2}	[S III]	I(9069+9532)/I(6312)	23.4
Ar^{+2}	[Ar III]	I(7136+7751)/I(5192)	27.6
O^{+2}	[O III]	I(4959+5007)/I(4363)	35.1
Cl^{+3}	[Cl IV]	I(7530+8045)/I(5323)	39.9
Ar^{+3}	[Ar IV]	I(4711+4740)/I(2854+2868)	40.9
Ne^{+2}	[Ne III]	I(3869+3969)/I(3342)	41.1
Ar^{+4}	[Ar V]	I(6435+7006)/I(4626)	59.8
Ne^{+4}	[Ne V]	I(3426+3346)/I(2975)	97.0

Table 2.4: Electron temperature diagnostics. The ionisation potentials indicated are the energy required to create the ion from the lower ionisation state. Standard notation is used where the spectrum designation is written between two square brackets for forbidden lines and a square bracket to the right of the spectrum designation for a semi-forbidden line.

The above mentioned line intensity ratio for doubly ionised oxygen changes from a value of almost 1 000 at a temperature of 7 000 K to less than 100 at 15 000 K. The ratio for the nitrogen lines changes from about 300 down to about 40 over the same temperature range (Figure 2.2). This, however, causes an observational problem because very high quality spectra are required to give an adequate signal-to-noise ratio to measure the fainter line. This method also systematically overestimates the electron temperature. This is because normal H II regions are not homogeneous but contain temperature gradients which can lead to colliding supersonic flows in which the density and electron temperatures may be raised as a result of shocks. The line emissivity in such regions can be raised by a factor N_e^2. Thus, the temperature estimate provided by the forbidden line ratio is dominated by the line ratio characterising these overdense inclusions, rather than providing a measure of electron temperature of the nebula as a whole.

The collisional excitation method was used to estimate the temperatures, together with the densities, of most of the objects in this project. The application of this method, using a software package, is described in chapter 4.

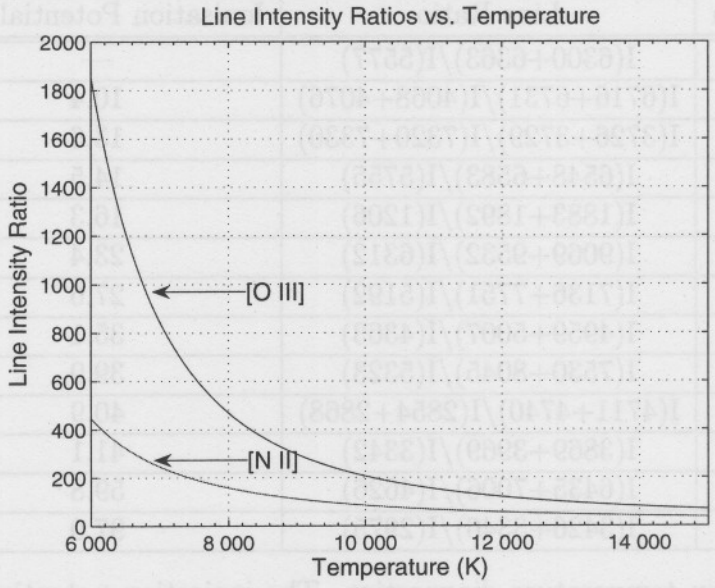

Figure 2.2: Line intensity ratios versus temperature for [O III] (equation 2.25) and [N II] (equation 2.26). The density was taken as 100 cm^{-3}, although the line ratio is not very sensitive to density.

Method 2: Recombination Line Method

A second technique is to use the ratio of a recombination line such as Hβ to the nebular continuum. Because the absolute value of the nebular continuum is difficult to determine in the presence of contamination from scattered stellar continuum, the change in the continuum across the Balmer discontinuity (also called the Balmer jump) at 3646 Å is used instead. He III in recombination also produces a bound-free continuum with a jump at the Balmer series limit and must therefore also be taken into account[6]. For a given source, if ΔF_{BL} is the measured size of the change in the continuum flux density (erg $cm^{-2}s^{-1}Hz^{-1}$) across the Balmer jump and $F_{H\beta}$ is the Hβ flux (erg $cm^{-2}s^{-1}$) from the nebula, then to a good approximation

$$\frac{F_{H\beta}}{\Delta F_{BL}} = 4.498 \times 10^{13} \left(1 + \frac{N_{\mathrm{He}^{+2}}}{N_{\mathrm{H}^{+}}}\right) t_e^{0.645} Hz \qquad (2.27)$$

where t_e is the electron temperature in units of 10^4K, thus $t_e = T_e/10^4$K. This technique (discussed in Dopita & Sutherland (2003) as well as Osterbrock (1989)) also requires good spectral resolution and a high signal-to-noise ratio.

[6]In H II regions, there is not much He III that are ionised by O and B stars, whereas in planetary nebulae the He III continuum is very important.

Method 3: Ionic Temperature Method

A third technique for measuring temperature does not yield the electron temperature, T_e, but the ionic temperature, T_i (this technique is briefly discussed in Dopita & Sutherland (2003)). The quantity that is observed is the thermal motions of ions along the line of sight. Consider measuring the full width at half maximum of the line profile, $\Delta\nu_{obs}$, in a line at frequency ν_0 belonging to a particular ion with mass m_i. At a given ionic temperature T_i, the fraction of ions with mass m_i in the velocity range v to $v + dv$ is given by the one dimensional Maxwell distribution (making the assumption of thermodynamic equilibrium):

$$dN(v) = \left(\frac{m_i}{2\pi k T_i}\right)^{\frac{1}{2}} e^{\left(-\frac{m_i v^2}{2kT}\right)} dv \tag{2.28}$$

where k is the Boltzmann constant. By themselves, the line-of-sight thermal motions will generate a Gaussian line profile with a shape function $\Phi(v)$ given by

$$\Phi(v) = \left(\frac{m_i c^2}{2\pi k T_i}\right)^{\frac{1}{2}} \exp\left[-\frac{m_i c^2(\nu - \nu_0)^2}{2kT_i\nu_0^2}\right] \tag{2.29}$$

and the Doppler line width (full width half maximum) is:

$$\Delta\nu^2_{therm} = 8\ln 2 \frac{kT_i}{m_i c^2}\nu_0^2 \tag{2.30}$$

A light element such as hydrogen or helium should be observed to provide sufficient thermal width, as can be seen from the $\frac{1}{m_i}$ dependence of $\Delta\nu^2_{therm}$. The observed line width is the resultant of this thermal broadening, the Doppler line width associated with turbulent motions, $\Delta\nu_{turb}$ and any line width resulting from unresolved fine-structure or hyperfine line splitting, $\Delta\nu_{FS}$. Assuming that these add in quadrature,

$$\Delta\nu^2_{therm} = \Delta\nu^2_{obs} - \Delta\nu^2_{turb} - \Delta\nu^2_{FS} \tag{2.31}$$

In order to derive the temperature therefore, we require an independent determination of $\Delta\nu_{turb}$. This is provided by means of bright forbidden lines of the heavier ions, for example the O^+ or the O^{+2} ions, provided that they sample a sufficient fraction of the ionised volume to provide a proper representation of the turbulence in this volume. It can be seen from the $\frac{1}{m_i}$ dependence of $\Delta\nu_{therm}$ that the line width of these forbidden lines from the heavier ions depend to a large extent on the turbulence in this volume. This technique is little used at optical frequencies, as it requires both high spectral and spatial resolution and low turbulence in the H II region to provide sufficiently accurate results.

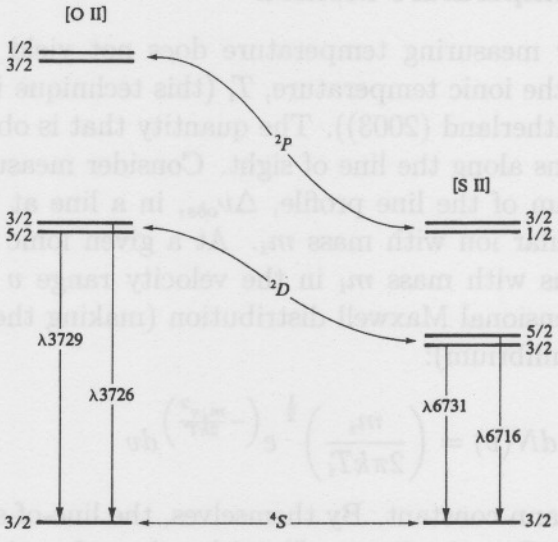

Figure 2.3: Energy level diagram of the $2p^3$ ground state configuration of [O II] and the $3p^3$ configuration of [S II]. Figure obtained from Osterbrock (1989).

2.1.4 The Density

Densities of hot nebulae may also be obtained from forbidden line intensity ratios. If the upper levels of two forbidden lines have similar energies (see Figure 2.3), then in the low density limit their intensity ratio will be close to unity. This is because the line strength will depend only upon the energy level populations and these will be in the ratio of the level's statistical weights, g (because the collisional rate between atoms and electrons is much slower than the radiative de-excitation rate of the excited levels). At higher densities, the radiative lifetimes of the levels will become longer than the mean time between collisions, which results in a Boltzmann distribution description of the gas. The line strengths will then additionally be proportional to the radiative transition probabilities (Einstein A probabilities) from the levels. The ratios of the line strengths will thus vary with density. In both the low and high density case, the relative populations of the levels are only in the ratio of the statistical weights because $\Delta E/kT \ll 1$ and thus, the factor $\exp(-\Delta E/kT) \rightarrow 1$.

The line ratios usually used for this purpose are I([O II]λ3729)/I([O II]λ3726) and I([S II]λ6716)/I([S II]λ6731), although other lines may also be employed. Consider the example of the [O II] forbidden lines in the low

density limit, in which every collisional excitation is followed by emission of a photon. Since the relative excitation rates of the $^2D_{5/2}$ and $^2D_{3/2}$ levels are proportional to their statistical weights, the ratio of the strengths of the two lines is simply $\frac{g(^2D_{5/2})}{g(^2D_{3/2})} = \frac{2(\frac{5}{2})+1}{2(\frac{3}{2})+1} = \frac{3}{2}$. On the other hand, in the high density limit, collisional excitations and de-excitations dominate and set up a Boltzmann population ratio. Thus, the relative populations of the two levels $^2D_{5/2}$ and $^2D_{3/2}$ are in the ratio of their statistical weights. Therefore the relative strengths of the two lines are in the ratio of their statistical weights as well as their radiative probabilities as shown by:

$$\frac{I(\lambda 3729)}{I(\lambda 3726)} = \frac{g(^2D_{5/2})}{g(^2D_{3/2})}\frac{A(3729)}{A(3726)} = \left(\frac{3}{2}\right)\frac{3.6 \times 10^{-5}}{1.8 \times 10^{-4}} = 0.30 \qquad (2.32)$$

(Osterbrock 1989). The transition between the high- and low-density limit occurs in the neighbourhood of the critical densities (defined as the density where the radiative depopulation rate matches the collisional de-excitation rate), which are $N_c = 3.1 \times 10^3$ cm^{-3} for $^2D_{5/2}$ and $N_c = 1.6 \times 10^4$ cm^{-3} for $^2D_{3/2}$ (Osterbrock 1989).

The full solution of the statistical equilibrium equations, which also takes into account all transitions, including excitation to the ^2P levels with subsequent cascading downward, gives the detailed variation of the intensity ratio with electron density. The collisional excitation rates once again bring the factor $N_e/T^{1/2}$ into these equations. The density-sensitive line ratios vary from about 1.5 in the low density limit to about 0.35 at high densities but the manner of the variation is complex (Dopita & Sutherland 2003). Just as the temperature equations are not very sensitive to density variations, the density equations are not very sensitive to temperature variations. This is because the small gap between the second and third level has the effect of suppressing the temperature dependence, since $\Delta E/kT \ll 1$, $\exp(-\Delta E/kT) \rightarrow 1$. The full statistical equilibrium equations also imply that the line ratios at both low and high density tend to limiting values.

A similar treatment holds for the [S II] line ratio. The [S II]$\lambda\lambda$6716, 6731 emission lines are easier to measure than the [O II]$\lambda\lambda$3726, 3729 emission lines, which can only be distinguished from each other by using a spectrograph with extremely good resolution.

These and other diagnostic line ratios are given in Table 2.5. Once again the table lists the ion, spectrum designation, diagnostic line ratio and ionisation potential of the ion. The line ratios are given as $I(\lambda_1)/I(\lambda_2)$, where λ_1 and λ_2 are in units of Å.

Ion	Spectrum	Line Ratio	Ionisation Potential (eV)
N^0	[N I]	I(5200)/I(5198)	—
S^+	[S II]	I(6716)/I(6731)	10.4
C^+	C II]	I(2326)/I(2328)	11.3
O^+	[O II]	I(3726)/I(3729)	13.6
Si^{+2}	Si III]	I(1883)/I(1892)	16.3
Cl^{+2}	[Cl III]	I(5517)/I(5537)	23.8
N^{+2}	N III]	I(1749)/I(1752)	29.6
Ar^{+3}	[Ar IV]	I(4711)/I(4740)	40.9
C^{+2}	C III]	I(1907)/I(1909)	47.9
O^{+3}	O IV]	I(1401)/I(1405)	54.9
Ne^{+3}	[Ne IV]	I(2423)/I(2425)	63.5

Table 2.5: Electron density diagnostics. The ionisation potentials indicated are the energy required to create the ion from the lower ionisation state.

Some of the forbidden lines can be used to form both temperature-sensitive and density-sensitive line ratios. Observation of both line ratios allows for a simultaneous solution of both temperature and density in the nebular zone containing these ions. An example of such a pair of line ratios is, in the [O II] ion, the $I(\lambda\lambda 7318, 7329)/I(\lambda\lambda 3726, 3729)$ and the $I(\lambda 3726)/I(\lambda 3729)$ line ratio. Another example is provided by the [S II] $I(\lambda\lambda 4069, 4076)/I(\lambda\lambda 6716, 6731)$ and the $I(\lambda 6731)/I(\lambda 6716)$ line ratio.

The determination of the densities of the objects in this project was similar to that of the temperatures; the description of this procedure follows in chapter 4.

2.1.5 Abundance Diagnostic Diagrams

The permitted hydrogen and helium lines observed at UV, optical and infrared wavelengths in ionised nebulae arise as a result of radiative recombination, followed by radiative cascade to lower levels. The recombination line spectrum is fundamental to an understanding of the physics of H II regions. In particular, the ratio of the intensities of the forbidden lines of heavier elements to the recombination lines of hydrogen provides us with our principal means of determining chemical abundances in ionised plasmas. Plotting pairs of emission-line ratios such as the ratio of a forbidden line to a Balmer line against an excitation-dependent ratio such as [O II]/[O III] can separate different classes of photoionised nebulae. The utility of such diagnostic

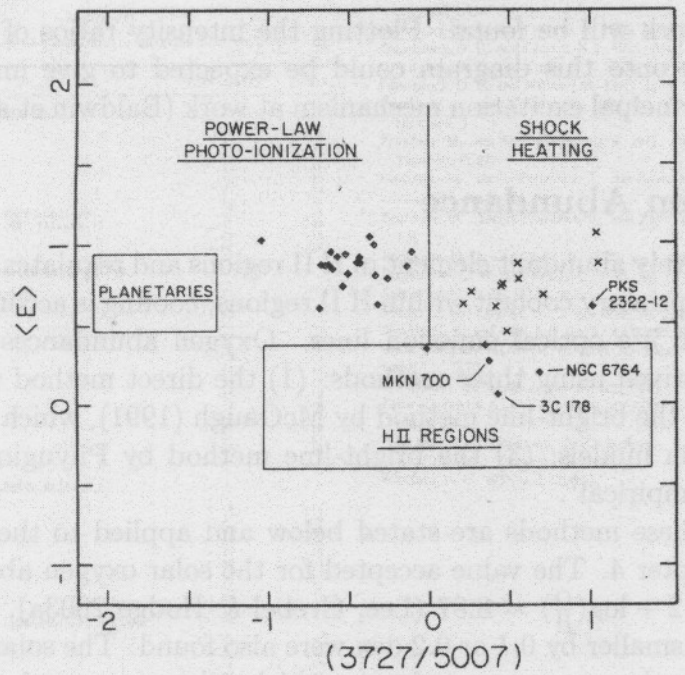

Figure 2.4: Abundance diagnostic diagram.

diagrams has been used for many years in the separation of H II regions from shock-excited plasmas and for abundance diagnostics in emission-line nebulae (Dopita & Sutherland 2003).

The factor that can be used to separate these objects is the excitation mechanism operating on the line-emitting gas. The predominant excitation mechanism, in extragalactic objects (such as the BCGs in this study), is almost always one of the following: (a) photoionisation by O and B stars (for example H II regions), (b) photoionisation by power-law continuum source (for example active galactic nuclei), or (c) shock-wave heating. A fourth excitation class is the planetary nebulae, which are photoionised by stars that are in most cases very much hotter than normal galactic O stars. Since the different classes of objects have characteristically different spectra, a classification system based on the relative strengths of emission lines can distinguish between the four possibilities. Figure 2.4 shows a diagnostic diagram from Baldwin, Phillips & Terlevich (1981), where the $\langle E \rangle$ on the y-axis is the excitation difference defined by four equations given in the above mentioned paper.

In plotting lots of extragalactic objects on a diagnostic diagram as in the one described above, four distinct zones corresponding to the four excitation

mechanisms at work will be found. Plotting the intensity ratios of a newly discovered object onto this diagram could be expected to give immediate insight into the principal excitation mechanism at work (Baldwin et al. 1981).

2.1.6 Oxygen Abundance

Oxygen is a relatively abundant element in H II regions and regulates physical conditions as the primary coolant within H II regions; cooling is accomplished primarily through it's optical emission lines. Oxygen abundances in H II regions can be derived using three methods: (1) the direct method using [O III] λ4363; (2) the bright-line method by McGaugh (1991), which is based on photoionisation models; (3) the bright-line method by Pilyugin (2000), which is purely empirical[7].

All three of these methods are stated below and applied to the data in this study in chapter 4. The value accepted for the solar oxygen abundance in this study is $12 + \log(\frac{\mathrm{O}}{\mathrm{H}}) = 8.87$ (Lee, Grebel & Hodge 2003a), however referenced values smaller by 0.1 or 0.2 dex were also found. The solar oxygen abundance frequently serves as a value to which other oxygen abundances can be compared.

Method 1: [O III]λ4363

For the direct conversion of emission-line intensity ratios into ionic abundances reliable estimates of the electron temperature and density in the ionised gas are required. The ionic abundances, relative to H^+, can be derived from the observed ratio of a forbidden-line intensity relative to the line intensity of Hβ. This is usually done with the aid of computer software packages or programs written to solve the equations of statistical equilibrium.

In general, for a given emission line, the emission rate of line photons resulting from a downward transition from $i \rightarrow k$, $j(i,k)$ is given by:

$$4\pi j(i,k) = A_{ij} N(\mathrm{X}^l) N_i h \nu_{ik} \qquad (2.33)$$

where N_i is the relative population in the upper level of the ion X^l, h is Planck's constant, ν_{ik} is the frequency of the photon emitted in the transition and A_{ij} is the Einstein probability for spontaneous emission (Shaw & Dufour 1995). When computing line emissivity ratios, for a given ion, $N(\mathrm{X}^l)/4\pi$ divides out and the expression depends only on the relative populations of the two levels and the atomic constants.

[7]These two methods are the most popular empirical methods in use. Other methods for example that of Zaritsky, Kennicutt & Huchra (1994) are also in existence.

Aller (1984) provides a convenient fitting formula for the Hβ emissivity (indicated by $j(\mathrm{H}\beta)$), which is accurate to within 4% for densities less than 10^6 cm^{-3}. The formula

$$4\pi j(\mathrm{H}\beta) = 1.387 \times 10^{-25} N_e N(\mathrm{H}^+) t_e^{-0.983} 10^{-0.0424/t_e} \tag{2.34}$$

in units of (erg cm^{-3}s^{-1}), is used in the nebular analysis routines, where $t_e = T_e/10^4$ K and N_e is the electron density.

The Hβ emissivity is calculated for the same temperature as the emissivity of the specified ion and the ionic abundance ratio is then calculated from

$$\frac{N(\mathrm{X}^l)}{N(\mathrm{H}^+)} = \frac{I(\lambda)}{I(\mathrm{H}\beta)} \times \frac{j(\mathrm{H}\beta)}{j(\lambda)} \tag{2.35}$$

where $I(\lambda)/I(\mathrm{H}\beta)$ is the observed line ratio. To see where this relation comes from, consider once again the definition of line intensity

$$I_\nu = \frac{A_{ji}}{4\pi} h\nu \int N_j \, dx \tag{2.36}$$

which together with equation (2.33), gives the appropriate relationship.

Note that the computed line emissivities are usually per unit ion density per unit electron density. That is, the true volume emissivity (j_{true}) is related to that computed by

$$4\pi j_{true} = N_e N(\mathrm{X}^i) j_{computed} \tag{2.37}$$

(Shaw & Dufour 1995).

In the case of the oxygen abundance, where the O^+ and O^{+2} ions are designated by [O II] and [O III], respectively, the total oxygen abundance by number is given by

$$\frac{\mathrm{O}}{\mathrm{H}} = \frac{\mathrm{O}^0}{\mathrm{H}} + \frac{\mathrm{O}^+}{\mathrm{H}} + \frac{\mathrm{O}^{+2}}{\mathrm{H}} + \frac{\mathrm{O}^{+3}}{\mathrm{H}} \tag{2.38}$$

For conditions found in typical H II regions very little O^0 is expected. Since the ionisation potential of He III is very similar to that of O^{+3}, the He II λ4686 emission (a measure of the He III abundance) is indicative of the presence of O^{+3}, which is also generally considered to be a small contributor to the oxygen abundance (Lee & Skillman 2004). The general procedure by which oxygen abundances are derived as in this direct method, also called the standard method, is summarised in Dinerstein (1990).

Given the temperature and density, an oxygen abundance can be determined from strong emission arising from singly and doubly ionised oxygen in the following manner (an application of equation 2.35):

$$\frac{N(\mathrm{O}^{+})}{N(\mathrm{H}^{+})} = \frac{I([\mathrm{O\ II}]\lambda 3727)}{I(\mathrm{H}\beta)} \frac{j(\mathrm{H}\beta; \mathrm{N_e}, \mathrm{T_e})}{j([\mathrm{O\ II}]\lambda 3727; \mathrm{N_e}, \mathrm{T_e})} \tag{2.39}$$

$$\frac{N(\mathrm{O}^{+2})}{N(\mathrm{H}^{+})} = \frac{I([\mathrm{O\ III}]\lambda 5007)}{I(\mathrm{H}\beta)} \frac{j(\mathrm{H}\beta; \mathrm{N_e}, \mathrm{T_e})}{j([\mathrm{O\ III}]\lambda 5007; \mathrm{N_e}, \mathrm{T_e})} \tag{2.40}$$

where I is the intensity of the line at wavelength λ, j is the volume emissivity of the line at density N_e and temperature T_e, and $N(\mathrm{X}^{+l})$ is the abundance by number of the atomic species in the l ionised state responsible for the line. The total oxygen abundance by number, $N(\mathrm{O})/N(\mathrm{H})$, is obtained from the sum

$$\frac{N(\mathrm{O})}{N(\mathrm{H})} = f\left[\frac{N(\mathrm{O}^{+})}{N(\mathrm{H}^{+})} + \frac{N(\mathrm{O}^{+2})}{N(\mathrm{H}^{+})}\right] \tag{2.41}$$

where f is an ionisation correction factor to account for unobserved oxygen ions. When little or no He II emission is detected, the ionisation correction factor could be assumed to be unity (Lee et al. 2003b).

Method 2: Bright-Line Method

The bright-line method is so called because the oxygen abundance is given in terms of the bright [O II] and [O III] lines. Pagel et al. (1979) suggested using

$$R_{23} = \frac{I([\mathrm{O\ II}]\lambda 3727) + I([\mathrm{O\ III}]\lambda\lambda 4959, 5007)}{I(\mathrm{H}\beta)} \tag{2.42}$$

as an abundance indicator. McGaugh (1991) developed a grid of photoionisation models and suggested using R_{23} and

$$O_{32} = \frac{I([\mathrm{O\ III}]\lambda\lambda 4959, 5007)}{I([\mathrm{O\ II}]\lambda 3727)} \tag{2.43}$$

to estimate the oxygen abundance. However, the calibration is degenerate such that for a given value of R_{23}, two values of the oxygen abundance are possible. This can be seen in Figure 2.5, where the relationship between the metallicity and R_{23} is illustrated.

Fortunately,

$$\frac{I([\mathrm{N\ II}]\lambda 6583)}{I([\mathrm{O\ II}]\lambda 3727)} \tag{2.44}$$

or the [N II]/[O II] ratio, as it is often called, was suggested (McCall, Rybski & Shields 1985) as the discriminant to choose between the high or low oxygen

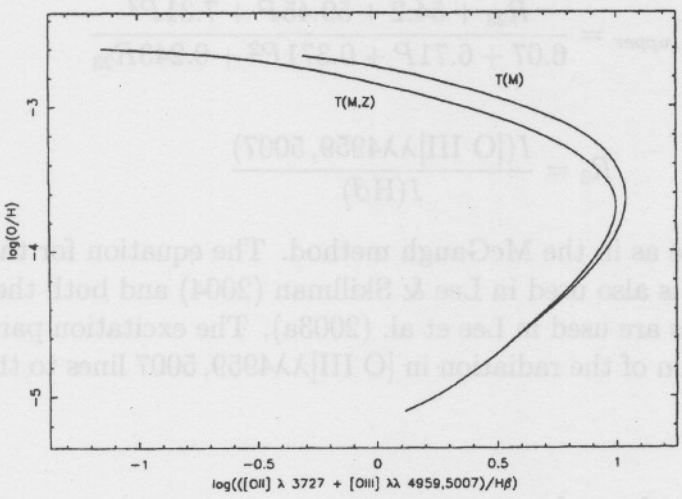

Figure 2.5: Comparison between the behaviour of R_{23} with $\log(\frac{\mathrm{O}}{\mathrm{H}})$ produced by models which assume that the temperatures are (1) a function $T(M, Z)$, of both mass and metallicity and (2) a function $T(M)$, of mass only. Figure taken from McGaugh (1991).

abundance. If this ratio is larger than 0.1 then the region has a high oxygen abundance and the upper value should be used. Similarly if the ratio is lower than 0.1 the lower value should be used (Lee et al. 2003a). For the McGaugh (1991) calibration, analytical equations for the oxygen abundance are given in terms of $x \equiv \log R_{23}$ and $y \equiv \log O_{32}$. The expressions for lower branch and upper branch oxygen abundances are

$$12+\log(\frac{\mathrm{O}}{\mathrm{H}})_{lower} = 12-4.93+4.25x-3.35\sin(x)-0.26y-0.12\sin(y) \quad (2.45)$$

$$12+\log(\frac{\mathrm{O}}{\mathrm{H}})_{upper} = 12-2.65-0.91x+0.12y\sin(x) \quad (2.46)$$

respectively, where the argument of the trigonometric function is in radians (Lee et al. 2003a).

Method 3: The Empirical Bright-Line Method

Pilyugin (2000) proposed a new calibration of the oxygen abundances using bright oxygen lines. His method accounts for systematic uncertainties in the R_{23} method. At low (Pilyugin 2000) and high (Pilyugin 2001) abundances respectively, his calibration is expressed as

$$12+\log(\frac{\mathrm{O}}{\mathrm{H}})_{lower} = 6.35+3.19\log R_{23}-1.74\log R_3 \quad (2.47)$$

$$12 + \log(\frac{\mathrm{O}}{\mathrm{H}})_{upper} = \frac{R_{23} + 54.2 + 59.45P + 7.31P^2}{6.07 + 6.71P + 0.371P^2 + 0.243R_{23}} \tag{2.48}$$

where

$$R_3 = \frac{I([\mathrm{O\ III}]\lambda\lambda 4959, 5007)}{I(\mathrm{H}\beta)} \tag{2.49}$$

and R_{23} is the same as in the McGaugh method. The equation for the lower oxygen abundance is also used in Lee & Skillman (2004) and both the upper and lower equations are used in Lee et al. (2003a). The excitation parameter P is the contribution of the radiation in [O III]$\lambda\lambda 4959, 5007$ lines to the total oxygen radiation.

2.1.7 Other Abundances

Ion	Spectrum	Lines Used (Å)
C^{+}	C II]	2326+2328
C^{+2}	C III]	1907+1909
N^{0}	[N I]	5198+5200
N^{+}	[N II]	5755,6548,6583
N^{+2}	N III]	1749+1752
O^{0}	[O I]	6300,6363
O^{+}	[O II]	3726+3729,7320+7330
O^{+2}	[O III]	4363,4959,5007
O^{+3}	O IV]	1400+1401+1405+1407
Ne^{+2}	[Ne III]	3342,3869,3968
Ne^{+3}	[Ne IV]	2423+2425,4724+4725
Ne^{+4}	[Ne V]	2975,3426,3346
Si^{+2}	Si III]	1206,1883+1892
S^{+}	[S II]	4068+4076,6716+6731
S^{+2}	[S III]	6312,9069,9532
Cl^{+1}	[Cl II]	3679,5807,9383
Cl^{+2}	[Cl III]	5517+5537
Cl^{+3}	[Cl IV]	5323,7531,8045
Ar^{+2}	[Ar III]	5192,7136,7751
Ar^{+3}	[Ar IV]	2854+2868,4711,4740,7170
Ar^{+4}	[Ar V]	4626,6435,7006

Table 2.6: Line fluxes often used for ionic abundances.

The lines that are typically used to derive ionic abundances, are listed in Table 2.6.

In the case of H II regions, the nitrogen and neon abundances are particularly interesting.

Nitrogen Abundance

Nitrogen is known to be both a primary and secondary product of nucleosynthesis. Measurement of the nitrogen-to-oxygen ratio, N/O, can be used as a time indicator to measure the time since the last burst of star formation. This scenario works if bursts of star formation are separated by long quiescent periods, which is exactly the case in BCGs (see next section). The result is that N/O values are low at a given O/H if a burst of star formation has occurred recently, whereas N/O values are high after a long quiescent period.

For low-metallicity H II regions, $\log(\mathrm{N/O}) \approx \log(\mathrm{N^+/O^+})$ is a good approximation, especially in nebulae containing ionising stars which are hotter than 40 000 K (Garnett 1990). Thus, the nitrogen-to-oxygen abundance ratio is

$$\frac{\mathrm{N}}{\mathrm{O}} = \frac{I([\mathrm{N\ II}]\lambda 6583)}{I([\mathrm{O\ II}]\lambda 3727)} \frac{j([\mathrm{O\ II}]\lambda 3727; \mathrm{N_e}, \mathrm{T_e})}{j([\mathrm{N\ II}]\lambda 6583; \mathrm{N_e}, \mathrm{T_e})} \tag{2.50}$$

where j is the volume emissivity at the given line at density N_e and temperature T_e (Lee et al. 2003a).

Neon Abundance

Neon is a product of α-processes in nucleosynthesis occurring in the same massive stars which produce oxygen. As a result, the neon-to-oxygen ratio, Ne/O, is expected to be constant with oxygen abundance. Assuming that doubly-ionised neon is found where doubly-ionised oxygen is found in the cloud, and that $\log(\mathrm{Ne/O}) \approx \log(\mathrm{Ne^{+2}/O^{+2}})$ then the neon-to-oxygen abundance ratio is

$$\frac{\mathrm{Ne}}{\mathrm{O}} = \frac{I([\mathrm{Ne\ III}]\lambda 3869)}{I([\mathrm{O\ III}]\lambda 5007)} \frac{j([\mathrm{O\ III}]\lambda 5007; \mathrm{N_e}, \mathrm{T_e})}{j([\mathrm{Ne\ III}]\lambda 3869; \mathrm{N_e}, \mathrm{T_e})} \tag{2.51}$$

(Lee et al. 2003a).

2.2 Metal Poor Blue Compact Galaxies

These galaxies are characterised by their very blue colour, compact appearance, high gas content and low chemical abundances of heavy elements (Kunth & Östlin 2000).

The concept of "compact galaxies" was introduced by Zwicky (Zwicky 1965), to denote galaxies barely distinguishable from stars on the Palomar Sky Survey plates. Originally, most studies of BCGs were concerned with objects from the lists of compact/emission-line/UV-excess galaxies produced by Zwicky (1966), Haro (1956) and Markarian (1967). However, only a fraction of the objects in these lists are BCGs, the others being Active Galactic Nuclei (AGN), normal spirals with nuclear star formation and H II regions in the outskirts of nearby spirals. BCGs are also referred to as H II galaxies, blue compact dwarf galaxies or blue amorphous galaxies. Different notations reflect a focus on different physical aspects, meaning that the classifications do not necessarily overlap completely and this loosely classified group may contain objects with different evolutionary histories. BCGs have luminosities in the range $m_B \approx -12$ to $m_B \approx -21$ (Kunth & Östlin 2000). The detailed morphology and surface photometry of BCGs have been studied by many investigators. The central morphology is often irregular due to the presence of active star formation but this contains very little information on the extended light distribution which likely traces the dominant stellar mass.

The metallicity, Z, is the mass fraction of elements other than hydrogen and helium. However, when calculating the metallicity of a galaxy, astronomers usually calculate the oxygen abundance (hereafter metallicity will mean oxygen abundance). The abundance of heavy elements in these galaxies range between $Z_\odot/50$ and $Z_\odot/2$, and put them among the least chemically evolved galaxies in the Universe[8]. BCGs undergo short bursts of star formation followed by longer, more quiescent periods (Kong & Cheng 2002a). A starburst produces a lot of metals and supernovae and stellar winds may eject gas into the intergalactic medium on short time scales. The low gravitational potential may also lead to the easy loss of metals and so explain their very low abundance.

The main reason BCGs were chosen to study spectroscopically was because of their bright emission lines and high surface brightness, as well as their cosmological importance. As it is fairly easy to discover them and thus derive their metal content, there exists a lot of high quality data on BCGs with which we can compare our results. These dwarf galaxies offer a very extreme environment for star formation and they can be so metal poor that their abundance analysis bears strong cosmological implications. One of the major reasons for this is that they host the H II regions from which the relation between helium and oxygen is derived and consequently, the primordial helium abundance; thus they provide a fundamental test for theories of Big

[8]The solar metallicity value of $12 + \log(\frac{O}{H}) = 8.87$ (Lee et al. 2003a) is used in this study and is equivalent to $Z_\odot = 7.413 \times 10^{-4}$.

Bang Nucleosynthesis. These galaxies are usually poorly evolved systems, thus the physical conditions within the starburst galaxies are thought to be similar to the conditions which existed in the early Universe, where the first generation of stars formed and galaxy formation occurred.

2.2.1 The Spectra of Blue Compact Galaxies

Extragalactic objects emit light from their constituent stars and from the hot gas clouds within them. They may also absorb the light from more distant objects against which they may be silhouetted. Their spectroscopic observation and much of the information that may be learned from it closely follows that of stars and nebulae. All the methods applicable to H II regions as discussed in the previous section, can be applied to BCGs.

The best known result of the spectroscopy of extragalactic objects is their redshift and the determination of their distances using the Hubble relation. The majority of extragalactic objects are moving away from our galaxy. It also means that the observed spectra in the visual region originated at shorter wavelengths. The redshift of a galaxy can be computed using the well known formula

$$z = \frac{V}{c} \qquad \text{for} \quad z \leqslant 0.3 \tag{2.52}$$

or

$$(1+z)^2 = \frac{(c+V)}{(c-V)} \qquad \text{for} \quad z > 0.3 \tag{2.53}$$

where V is the recession velocity of the galaxy and c is the velocity of light.

The shifts in the wavelength can then be determined from the equation

$$\frac{\Delta\lambda}{\lambda} = \frac{V}{c} \tag{2.54}$$

where $\Delta\lambda$ is the shift in the wavelength, and λ is the rest wavelength.

For example, at a redshift of $z = 3$, the observed wavelengths over the region 4000 — 7000 Å would have been emitted between 1000 and 1750 Å. For many extragalactic objects therefore, we may observe their UV and far-UV spectra via optical spectroscopy. For closer objects, we can observe most or all of the normally visible spectrum. The BCG Zw 0855 has a recession velocity of $V = 3110$ km s^{-1} (Kong & Cheng 2002a), which is equivalent to a redshift of 0.0104 and as a result the observed wavelengths at 4000 Å would be shifted about 41 Å, and those at 7000 Å about 72 Å. Similarly, Mrk 1267 has a recession velocity of $V = 6185$ km s^{-1} (Kong & Cheng 2002a), which equates to a redshift of 0.0206, thus the observed wavelengths at 4000 Å would be shifted by 81 Å and those at 7000 Å by 141 Å. This

means that even for small redshifts, this change in wavelength is significant and extreme care needs to be taken when calibrating the observed spectra. The procedure used to correct the relevant Doppler shift on the extragalactic objects in this study, is described in chapter 4. Table 2.7 lists the redshifts of the five BCGs selected for this study (Tol 2 and Tol 3 is from Simbad Astronomical Database, while II Zw 33 is also from Kong & Cheng (2002a)).

With the recession velocity (V) known, the distance to the extragalactic sources was calculated by using the equation

$$V = H_0 d, \tag{2.55}$$

where H_0 is the Hubble constant and d the distance to the object. Assuming $H_0 = 75$ km s^{-1}Mpc^{-1}, the equation leads to the values in Table 2.7.

Galaxy	Redshift (z)	Distance (Mpc)
Zw 0855	0.0104	41.6
Mrk 1267	0.0206	82.4
II Zw 33	0.0095	38.0
Tol 2	0.0032	12.8
Tol 3	0.0036	14.4

Table 2.7: Redshifts of BCGs.

The optical spectra of BCGs show strong, narrow emission lines superimposed on an almost featureless continuum, similar to the spectrum of an H II region. The least blue systems generally show both emission and absorption lines, while the bluest usually show only emission lines. Forbidden iron lines are an indicator of a starburst galaxy, and probably arise from the numerous supernovae occurring in them, unfortunately these lines are very weak and a good signal-to-noise ratio is required to observe them.

Some of the BCGs in this study formed part of a previous study by Gordon & Gottesman (1981), who has focused on the Haro (1956), Markarian (1967) and Zwicky (1966) lists of galaxies. The objects on these galaxy lists were selected on the basis of a blue colour, UV-excess or compactness, but not necessarily on the basis of emission-line strength (Kunth & Östlin 2000). The optical spectral observations of the galaxies from the Gordon & Gottesman (1981) sample have shown a range in spectral properties; from galaxies with absorption-line spectra to narrow emission-line objects classified as star-forming galaxies (SFGs). In order to correctly classify BCGs from these lists, firstly as emission-line galaxies and then as true SFGs, the following procedure can be used:

- Because the Hα recombination line is easily detected in an optical spectrum and is only weakly affected by dust and underlying stellar absorption, it can be used in order to classify spectra into those originating in emission-line galaxies and non-emission line galaxies. When Hα is detected in emission, the galaxy is an emission-line galaxy, otherwise it is a non-emission line galaxy.

- Further, if

$$\log\left(\frac{I([\text{N II}]\lambda 6583)}{I(\text{H}\alpha)}\right) < -0.25 \tag{2.56}$$

the galaxy can be classified as a SFG, H II-like (Kong et al. 2002b), otherwise it is an AGN. This condition is tested in chapter 4.

This classification scheme forms part of the spectral classification methods of emission-line galaxies, as developed by Veilleux & Osterbrock (1987), also described by Carter et al. (2001). This classification scheme is also briefly described in this chapter, under "Abundance Diagnostic Diagrams".

2.2.2 The Star Formation Rate

Understanding the star formation history of the Universe is the primary goal of much current research in astronomy. The SFR is a crucial ingredient to understand the star formation history of galaxies at all redshifts, as well as the global evolution of the Universe (Kong 2004). Thus, a reliable estimate of the SFR in individual galaxies is very important, and the blue colour, high gas content and strong nebular emission-line spectrum of BCGs indicate that they have a high star formation activity.

Line luminosities, derived from line fluxes, can be utilised as an indicator of the SFR of a galaxy. The following equation shows the relation between luminosity (L) and reddening corrected flux (I):

$$I(\text{erg s}^{-1}\text{cm}^{-2}) = \frac{L(\text{erg s}^{-1})}{4\pi d^2} \tag{2.57}$$

where d equals distance to the object (given in Table 2.7) which should be substituted in this equation in the unit cm.

For star-forming galaxies, the Balmer emission-line luminosities scale directly with the ionising fluxes of the embedded young stars and this makes it possible to use the Balmer lines to derive SFRs in galaxies. Hα is the best line for such applications (Kong et al. 2002b), but beyond $z \simeq 0.2 - 0.3$, this line is redshifted into the near infrared. To find other tracers of SFRs, the fluxes of other emission lines are analysed as a function of intrinsic Hα flux. From

purely astrophysical considerations, the most reliable star forming tracers in the blue should be the higher order Balmer lines, as the fluxes of these lines scale directly with massive star formation and are nearly independent of the temperature and ionisation level of the emitting gas. For the estimate of the SFR from Hα luminosities, the expression given by Kong (2004) can be used:

$$SFR_{\mathrm{H}\alpha}(M_\odot\ \mathrm{yr}^{-1}) = 7.9 \times 10^{-42} L_{\mathrm{H}\alpha}(\mathrm{erg\ s}^{-1}) \tag{2.58}$$

which is valid for a $T_e = 10^4$ K and the case of recombination where all the ionising photons are processed by the gas (thus, recombination to the ground state produce an ionising photon that ionises another hydrogen atom — this is usually called case B).[9]

If recombination lines are unavailable, the collisionally excited lines of heavy elements may be used instead. The [O II]λ3727 doublet is by far the strongest emission line in the blue and readily observable. It is also the most natural star formation tracer for objects with redshifts larger than 0.4 where Hα is shifted outside the optical range (Jansen, Fabricant & Franx 2001). The [O II]λ3727 luminosity is not directly coupled to the ionisation rate and its excitation is known to be sensitive to the abundance and the ionisation state of the gas. However, as the excitation of [O II]λ3727 is sufficiently stable in observed galaxies, it can be calibrated empirically with Hα as a quantitative indicator of the SFR. The relation between the SFR and $L_{[\mathrm{O\ II}]}$ can be expressed as:

$$SFR_{[\mathrm{O\ II}]}(M_\odot\ \mathrm{yr}^{-1}) = 9.3 \times 10^{-42} L_{[\mathrm{O\ II}]}(\mathrm{erg\ s}^{-1}) \tag{2.59}$$

(Kong 2004). This formula is similar to that given by Rosa-González, Terlevich & Terlevich (2002), where $SFR_{[\mathrm{O\ II}]}(M_\odot\ \mathrm{yr}^{-1}) = 1.4 \times 10^{-41} L_{[\mathrm{O\ II}]}$ (erg s^{-1}).

All of the SFR expressions above are for a Salpeter initial mass function (IMF), $N(m) \propto m^{-2.35}$, with masses varying from $0.1M_\odot$ to $100M_\odot$. The initial mass function of massive stars is one of the reasons why the formation of stars in extragalactic starbursts is still far from understood. Some of the questions that still need to be answered are the dependence of the IMF on environment, metallicity and other parameters and if it is the same everywhere. The history of formation of stars in starbursts is even less certain.

The reddening corrected emission-line fluxes used in the determination of the luminosity require an aperture correction to account for the fact that only a limited amount of emission from a galaxy is detected through the slit

[9]Case A is the case in which all optical depths are small and all photons escape. These cases are also called Menzel Case A and B after American physicist and astronomer Donald Howard Menzel (1901-1976).

during observations. Two different methods (both described in Kong (2004)) can be used. The first method is to determine the B-band magnitude from the spectra and to estimate the fraction of the B-band photometry for the whole galaxy. The second method is to use digitised images (for example Palomar images) to estimate the slit covering fraction for the galaxies, by measuring the ratio of the photographic flux within the slit aperture to the total photographic flux. However, the most important correction that has to be performed is the removal of the effect of underlying stellar Balmer absorptions in the measured emission-line fluxes. Some authors correct the underlying stellar absorption by adopting a constant equivalent width for all hydrogen absorption lines. This constant value can be predicted by models for synthetic absorption line spectra in starburst galaxies but unfortunately, spectra in the Hα region have second order contamination in many objects (Stasińska, Schaerer & Leitherer 2001). As the real value of the absorption equivalent width is uncertain and depends on the age of the star formation burst and the star formation history, the other usual correction for the contamination by stellar absorption lines assumes absorption equivalent widths, and iterates until the colour excesses derived by the Balmer decrement method (described fully in chapter 4) converge to the same value (Kong et al. 2002b). In the study conducted by Kong (2004) the SFRs were determined by using four methods comprising Hα, [O II]λ3727, infrared and radio luminosities, to assess the possible systematic differences among different star formation rate indicators. It was found that subtracting the underlying stellar absorption is very important in order to accurately calculate both dust extinction and the star formation rate of galaxies. Otherwise, the intrinsic extinction will be overestimated, and the SFRs derived from Hα and [O II]λ3727 will be underestimated (if the underlying stellar absorption and the internal extinction is not corrected) or overestimated (if an overestimated internal extinction is used for extinction correction). In the above mentioned study, the SFRs derived from Hα and [O II]λ3727 showed large discrepancies when compared to other indicators. The same conclusion was reached by Rosa-González et al. (2002) who compared SFRs determined by using Hα, [O II]λ3727, the far-UV continuum and the far-infrared luminosities. As no correction was performed on the underlying stellar Balmer absorptions in this dissertation (but the reddening correction was), there would have been a definite overestimation if the SFRs had been computed for the five BCGs. Caution should also be taken before blindly applying expressions for SFRs, such as those given above, to BCGs as it was found that the expressions are derived for cases of solar metallicity and continuous star formation.

Kong (2004) states that the SFRs of BCGs might vary over five orders of magnitude and it is not clear whether this wide range is as a result of the

use of different techniques, assumptions or sample selections employed in the available studies.

2.3 Concluding Remarks

The study of the ISM, once merely a major nuisance for optical astronomers, has become an important branch in modern astronomy. The subject offers fascinating variety, because the regions to be studied extend far through interstellar space. The consequent extreme rarefaction of matter and the dilution of the radiation field produce local conditions which are as far removed from thermodynamic equilibrium as anywhere in the Universe. This fact provides both the interest and the challenge of the investigation of the ISM. The birth, life and death of stars are essential to keep the material between the stars churning with activity. In turn, the ISM, bound gravitationally to the galaxies, traps the heavy elements expelled by dying stars. When pockets of gas and dust become dense and cold enough to become self-gravitating, the enriched material goes into forming a new generation of stars and planets.

Chapter 3

Observations and Data Reduction

This chapter contains a description of the instrumentation used with the procedures followed during the observation of the sources, as well as a detailed account of the data reduction and spectra extraction processes. The wavelength and flux calibration procedures are described, with the standard star and sky spectra also being shown.

3.1 Observations

3.1.1 The Optical Spectroscope

Detectors operating in the optical part of the spectrum are generally broadband devices. As they are sensitive to radiation over a wide range of wavelengths, the spectrum cannot be observed directly, as may be the case at shorter wavelengths, where the detector's response varies with the energy of the photon. In the optical region a spectroscope is required to separate the radiation into its component wavelengths before it is detected. There are several processes whereby the radiation can be separated into its component wavelengths; the method used in this study consisted of diffraction gratings.

Although a grating will usually contain many thousands of apertures, the principle of its operation is based upon the interference effects produced by just two apertures. This will be described below by following the discussion of Kitchin (1995). Consider the Fraunhofer (far-field) interference effects from a pair of closely spaced apertures (Figure 3.1a) illuminated by a distant monochromatic source of wavelength, λ. The path difference at an angle θ to the incoming ray is shown in Figure 3.1b and given by

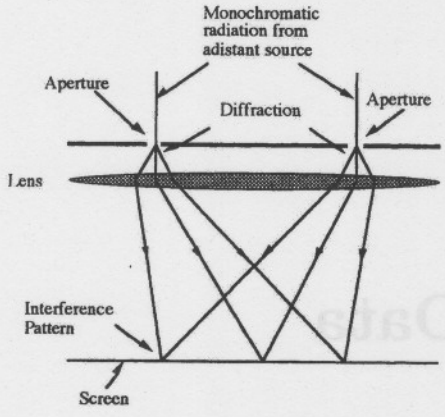

(a) Fraunhofer interference from a pair of apertures.

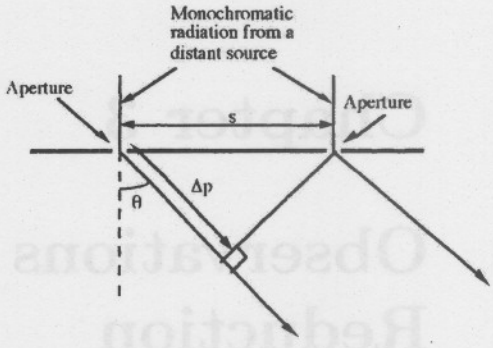

(b) Path difference in Fraunhofer interference at two apertures.

Figure 3.1: Fraunhofer interference.

$$\Delta p = s \times \sin\theta \tag{3.1}$$

where s is the separation of the apertures. The interference pattern on the screen will be a series of light and dark fringes as the path difference is an integer, or integer plus half, number of wavelengths and we have constructive and destructive interference respectively. The intensities of the maxima are modulated by the interference pattern from a single aperture. The centres of the bright fringes correspond to integer wavelength path differences and so at such points we have

$$\Delta p = s \times \sin\theta = n\lambda \tag{3.2}$$

where n is an integer, usually referred to as the order of interference. The angle between successive maxima is thus

$$\Delta\theta = \sin^{-1}\left(\frac{(n+1)\lambda}{s}\right) - \sin^{-1}\left(\frac{n\lambda}{s}\right) \tag{3.3}$$

which for small angles simplifies to

$$\Delta\theta \approx \frac{\lambda}{s} \tag{3.4}$$

If the normal to the plane of the apertures is at an angle ϕ to the incoming radiation, corresponding to the often utilised inclined grating, then (Figure 3.2a)

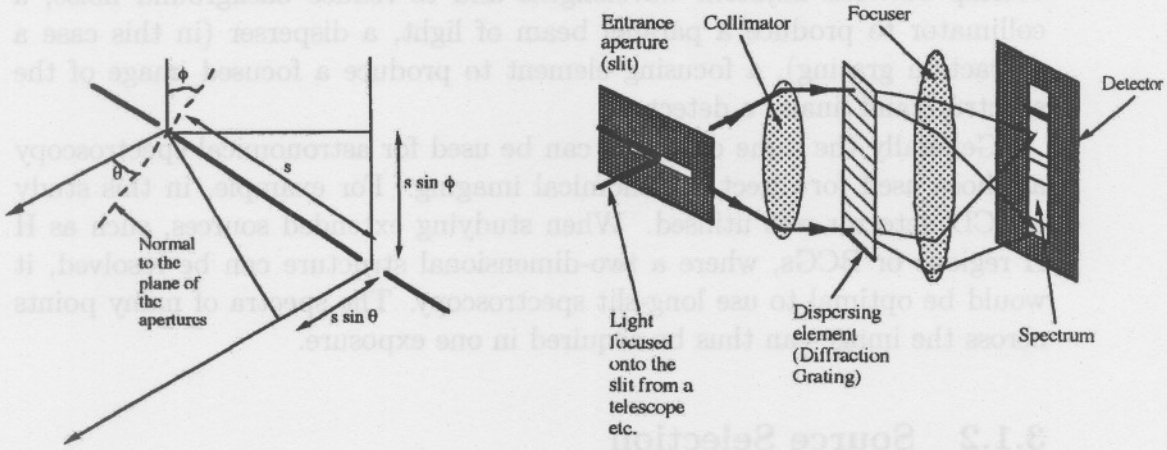

(a) Plane of the apertures inclined to the incoming radiation.

(b) Basic components of a spectroscope.

Figure 3.2: The optical spectroscope.

$$\delta p = s \times \sin\theta + s \times \sin\phi = n\lambda \tag{3.5}$$

This gives the grating equation in its normal form

$$\theta = \sin^{-1}\left(\frac{n\lambda}{s} - \sin\phi\right) \tag{3.6}$$

From this grating equation, we can see that the angular position of the maxima are wavelength dependent. Maxima for different wavelengths will therefore appear at different angles to the incoming radiation and thus we have the principle of operation of the diffraction grating. Adding further apertures causes the primary fringe widths to reduce further and although more secondary maxima are produced, they become progressively weaker. By the time the number of apertures has reached double figures, the secondary maxima have almost disappeared while the primary maxima have become narrow enough for different wavelengths to be separated out. In practice, gratings contain thousands of apertures and the angular fringe widths become equivalent to fractions of a nanometre.

In order to produce a usable spectrum, the diffraction grating must usually be combined with several other components and it is this combination that is usually referred to as a spectroscope. Most spectroscopes incorporate the following basic components (Figure 3.2b): an entrance slit to reduce

overlap between adjacent wavelengths and to reduce background noise, a collimator to produce a parallel beam of light, a disperser (in this case a diffraction grating), a focusing element to produce a focused image of the spectrum and finally a detector.

Generally the same detectors can be used for astronomical spectroscopy as those used for direct astronomical imaging. For example, in this study a CCD detector was utilised. When studying extended sources, such as H II regions or BCGs, where a two-dimensional structure can be resolved, it would be optimal to use long-slit spectroscopy. The spectra of many points across the image can thus be acquired in one exposure.

3.1.2 Source Selection

Galactic H II Regions

The bright galactic H II region designated RCW 57 comprises the optically bright and extended nebula NGC 3576 (G291.28-0.71) as well as the giant H II region and OB star cluster NGC 3603 (G291.58-0.43). These nebulae were selected to be of relatively high excitation for H II regions. The former region, NGC 3576, also formed part of a previous study in which UBVRI imaging was carried out on southern high mass star formation regions in order to search for optically visible pre-main sequence stars associated with the region. Located at distances of 3.0±0.3 kpc (NGC 3576) and 6.1±0.6 kpc (NGC 3603) respectively (De Pree, Nysewander & Goss 1999), their proximity in the sky (∼30' apart) is accidental, with no physical association. NGC 3603, with a bolometric luminosity of $10^7 L_\odot$, contains some $10^4 M_\odot$ of ionised gas and aside from W49A may be the most massive H II region in the Galaxy (De Pree et al. 1999).

Blue Compact Galaxies

The three BCGs Zw 0855, Mrk 1267 and II Zw 33 were selected from a sample of BCGs previously studied by Kong & Cheng (2002a) and before that, by Gordon & Gottesman (1981). Kong & Cheng (2002a) performed an optical spectroscopic study, whereas Gordon & Gottesman (1981) studied BCGs in the radio region. The latter authors assembled their list of BCGs from the Markarian (1967), Haro (1956) and Zwicky (1966) lists. The BCGs Tol 2 and Tol 3 form part of the Palomar/Las Campanas Imaging Atlas of Blue Compact Galaxies (Gil de Paz, Madore & Pevunova 2003). Tol galaxies were originally discovered through the presence of emission lines, for example the [O III]λ5007 line, and were first observed at the Cerro Tololo

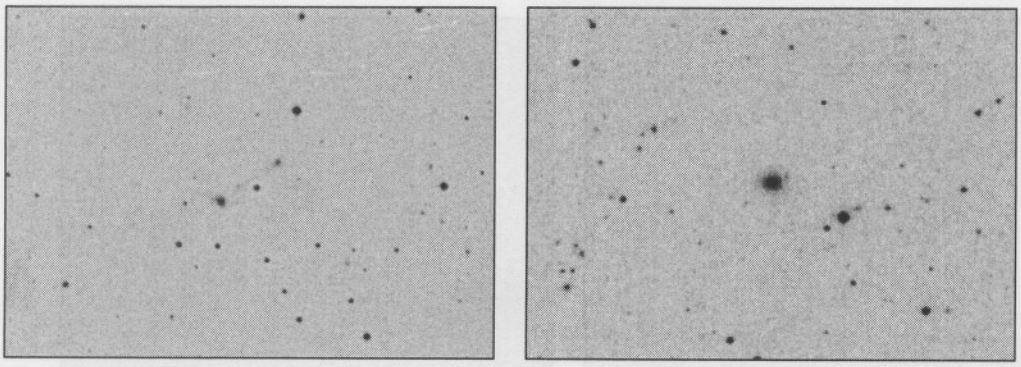

(a) Zw 0855 (b) Mrk 1267

Figure 3.3: Sources. Images obtained from Aladin Sky Atlas.

Observatory, Chile. These five galaxies were initially selected on the basis of their integrated B-magnitudes, as the limitations of using a 1.9m telescope for this kind of study called for extragalactic objects which are relatively bright in order to detect them on the CCD-based acquisition camera. A further prerequisite for the sources was that the objects had to be readily visible from the southern hemisphere at the time of the planned observations. Table 3.1 shows the list of principal targets, the two galactic H II regions and the five BCGs.

Blue Compact Galaxies

Name	α(J2000)	δ(J2000)	mag
Zw 0855	08 58 27.4	+06 19 41.3	$m_B \sim 14.5$
Mrk 1267 (UGC 6003)	10 53 03.9	+04 37 54	$m_B \sim 14.5$
II Zw 33 (UGCA 102, Mrk 1094)	05 10 48	−02 40 54	$m_B \sim 14.0$
Tol 2 (AM 0957-275)	09 59 21.21	−28 08 00.28	$m_B \sim 14.5$
Tol 3 (NGC 3125, AM 1004-294)	10 06 33.33	−29 56 06.60	$m_B \sim 13.3$

Galactic H II Regions

Name	α(J2000)	δ(J2000)
NGC 3576 (G291.28-0.71)	11 11 51.2	−61 18 23.3
NGC 3603 (G291.58-0.43)	11 15 09.1	−61 16 17

Table 3.1: List of principal targets, alternative names for these objects are given in brackets.

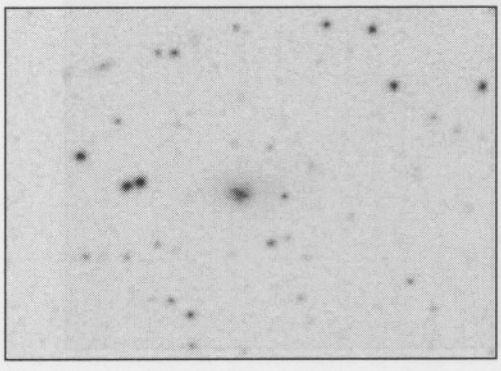

(c) Tol 2

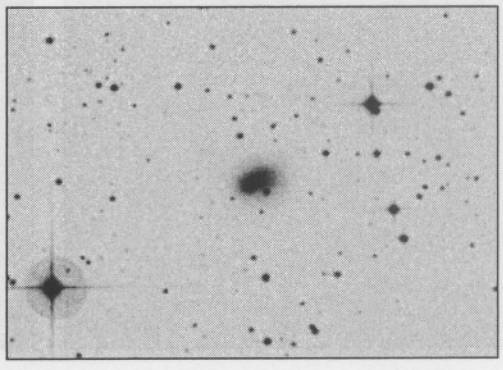

(d) Tol 3

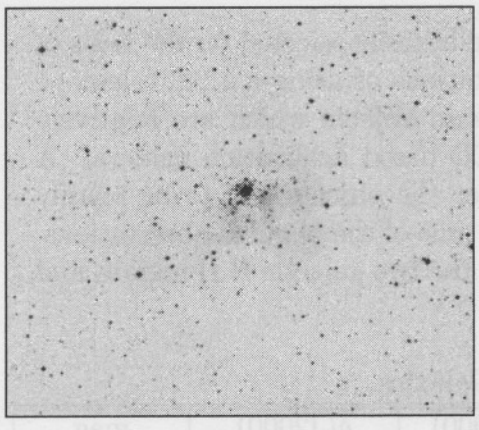

(e) NGC 3603

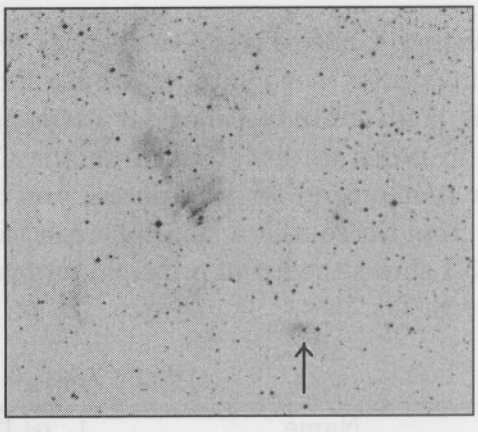

(f) NGC 3576

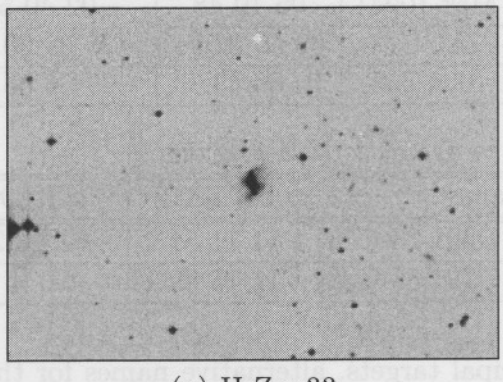

(g) II Zw 33

Figure 3.3: Sources (continue). Images obtained from Aladin Sky Atlas.

3.1.3 Source Observations

Observations of the sources listed in Table 3.1 were carried out during the period 1 to 7 March 2005 by the author, together with D.J. van der Walt and C.G. Deale using the 1.9m (Radcliffe) telescope of the SAAO at Sutherland, in the Northern Cape province, South Africa. This telescope was equipped with a grating spectroscope and a SITe CCD. The scale of the spectroscope slit was 6 arcsec mm^{-1} and the normal slit width was 1.2 — 1.5 arcsec. Comparison spectra were provided by a Cu/Ar arc and flat-field illumination by a quartz-iodine lamp. The SITe CCD is effectively 266 × 1798 pixels in size, and can be used at wavelengths ranging from 3500 Å to 10 000 Å. Pixel size is 15 microns, which corresponds to 0.74 arcsecs perpendicular to the dispersion axis.

One of the seven observing nights was totally lost due to cloud cover, with occasional early morning ridge clouds interrupting observations on some of the others.

During the observation period various calibration spectra were obtained, for example dome flat fields, twilight flat fields, bias images and sky spectra. Spectra of all of the objects as well as calibration spectra were taken using two different gratings. The gratings used are listed in Table 3.2.

Grating no.	Useful Range (Å)	Blaze (Å)	Resolution (Å)	Dispersion (Å mm^{-1})
6	1600	4600	2	100
7	3200	4600	5	210

Table 3.2: Gratings used in the spectrograph.

The number of object spectra together with exposure times are shown in Table 3.3. With the H II region NGC 3603, the slit was placed on three different regions (middle, upper, lower) on the object to obtain spectra from the different regions. All of the extended source objects observed, appeared very faint on the CCD-based acquisition and auto-guide cameras, which made it very difficult to place the slit on the same region of the objects on different nights. Multiple spectra, instead of long exposures, of the objects were taken and combined after reduction in order to avoid saturation effects on the CCD. It should be noted that it was not possible to change the orientation of the slit or the telescope in order to control the slit placement on the source (for example to place the slit along the major or the minor axes of the source).

Name	Number and Time (s)	Grating Used (6 or 7)
Zw 0855	8×900	7
	2×900	6
Mrk 1267	4×900	7
	1×900	6
II Zw 33	3×900	7
	2×900	6
Tol 2	2×900	7
	2×900	6
Tol 3	1×900, 2×450	7
	2×900	6
NGC 3576	3×120	7
NGC 3603	1×60, 16×120 (middle)	7
	1×120, 2×900 (upper)	7
	2×900 (lower)	7
	1×120, 1×600 (middle)	6
	1×600 (upper)	6

Table 3.3: Number of exposures and exposure times.

Standard stars were also observed for the purpose of flux calibration. These stars were observed two or three times throughout the night, at different airmasses, with an exposure time of 300 seconds. The standard stars that were observed are shown in Table 3.4.

	LTT 3218	HR 4468 (Theta Crater)
α(J2000)	08 41 34.10	11 36 40.91
δ(J2000)	−32 57 00.1	−09 48 08.2
V_{mag}	11.86	4.70
$B-V$	+0.22	−0.07
Spectral type	DA	B9.5V

Table 3.4: Standard stars.

Before and after every standard star or object spectrum, a calibration (comparison) spectrum of the Cu/Ar arc was obtained for the purpose of wavelength calibration.

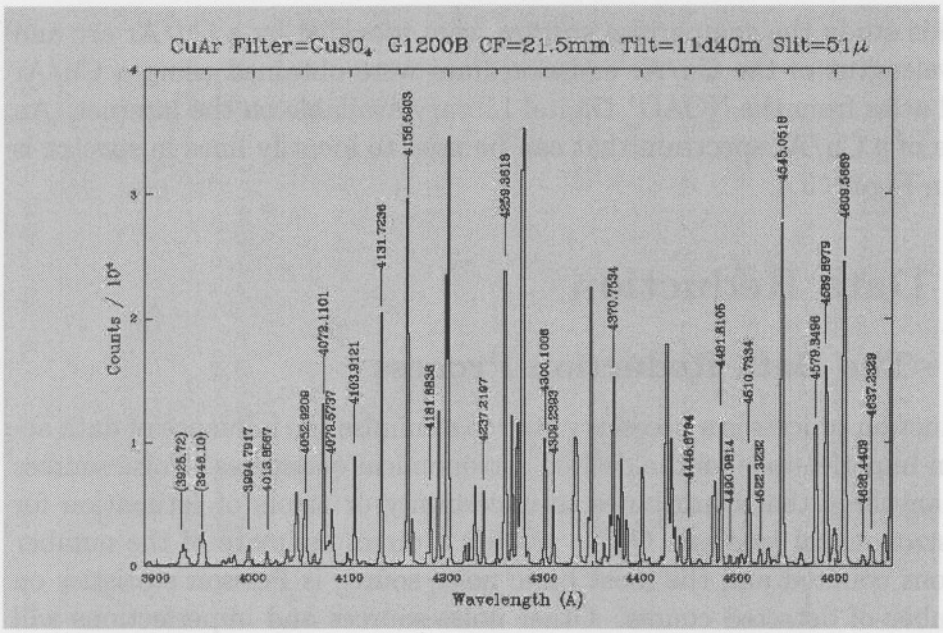

Figure 3.4: Comparison Spectrum (Cu/Ar).

3.1.4 Comparison Spectra

From the earliest days of stellar spectroscopy it has been realised that a comparison spectrum would be needed to enable precise wavelength data to be obtained (see "Historical Background" section). The comparison spectrum is an emission-line spectrum, produced on or near the spectroscope from an emission lamp or an electric arc, the light from which is fed into the spectroscope. For a CCD or equivalent image, measurement of the position of a spectral line (and hence its wavelength) is made by using the appropriate data reduction software. Since the wavelengths of the emission lines in the comparison spectrum are known, the observed wavelengths of lines in the spectrum of interest can be found by interpolation. A great deal of care needs to be taken if accurate wavelengths are to be obtained, in particular when lines are asymmetrical and the dispersion is nonlinear. With such care, however, observed wavelengths in the visible region may be determined typically to about one part in $30\,000/n$, where n is the dispersion of the spectrum in nm mm^{-1}. This corresponds to being able to determine radial velocities through the Doppler shift to an accuracy of about $\pm 10n$ km s^{-1}. For example, the grating 7 used in this study has a dispersion of $n = 21$ nm mm^{-1}. Therefore, the Doppler shift can be determined to an accuracy of about ± 210 km s^{-1} (z=0.0007) under ideal conditions.

In this study the comparison spectra were provided by a Cu/Ar arc and the wavelengths of the Cu/Ar emission lines were obtained using a Cu/Ar spectral atlas from the NOAO[1] Digital Library available on the internet. An example of a Cu/Ar spectrum that can be used to identify lines in spectra is shown in Figure 3.4.

3.2 Data Reduction

3.2.1 The Data Reduction Process

The reduction process is a necessary step to minimise the influence of data acquisition imperfections on the desired astronomical quantities. Noise sources can be anything that contributes to uncertainty or errors of estimation for some astronomical interest. CCDs provide a direct estimate of the number of photons counted and the most basic noise source is Poisson statistics on the number of detected counts. Other noise sources and imperfections will be described below by following the discussion of McLean (1997).

Bias

In most CCD systems it is necessary to purposely offset the video signal slightly positive so that the readout noise never drives the input negative. This electronic instrument signature is therefore known as bias level and can be determined easily by taking an unexposed frame (zero exposure time, shutter closed). Several bias frames can be averaged to reduce the random readout noise while preserving any spatially coherent noise and the pixel-to-pixel bias levels. The normal procedure in astronomy is to take many bias frames and subtract the median of that set from each exposed frame as the first step in data reduction. Bias information can also be conveniently obtained in many CCD systems by using an overscan i.e. the sequencer is told to send more clock pulses than are actually required to vertically and horizontally read out the real CCD (eg. 1034×1034 instead of 1024×1024). If the system is working perfectly then a bias frame should contain very little fixed pattern structure; it should be dominated by random readout noise variations.

Flat-fielding

CCDs do not have a uniform response to light across their surfaces. Pixel-to-pixel variation in sensitivity arise due to physical differences between pixels

[1]National Optical Astronomy Observatories.

as the result of manufacture processes and due to optical attenuation effects such as microscopic dust particles on the surface of the CCD. The images that are taken to correct for these effects are called flat-field images. A common practice is to observe the inside of the telescope dome (if it is matt white) or a huge white card on the dome. Flat-field images can also be obtained by observing the uniformly illuminated twilight.

General Procedure

These and other effects must be removed in an optimum sequence. In general the reduction and calibration of raw CCD images can be done according to the following pattern:

1. **Subtract bias and bias structure:** A bias image, obtained by averaging many bias frames is subtracted and overscan data are also removed.

2. **Subtract dark:** Most CCDs exhibit some dark current or a low-level light-emitting diode activity, leading to electronic pollution during long exposures. To correct for this effect, the median image of many long dark exposures must be subtracted from the object frames.

3. **Divide by flat-field:** Many flat-field exposures are averaged for each filter (for spectroscopic data this procedure is only done once). The bias-corrected, dark subtracted, flat-field averages are then divided into the object frames.

4. **Subtract fringe frame:** Night-sky emission lines limited to a very narrow band of wavelengths can cause interference fringes on some back-illuminated CCDs bonded to glass. A fringe frame must be scaled and subtracted from the flat-fielded object frame.

5. **Interpolate over bad pixels:** A bad pixel map for the particular CCD in use can be supplied as input to a median interpolating routine whereby the bad pixels will automatically be filtered out.

6. **Remove cosmic ray events:** A computer algorithm can be used to identify non-starlike point sources, and cosmic radiation events can be eliminated.

7. **Registration of frames and median filtering:** If the random offsetting technique is used, re-registration of data frames to a fraction of a pixel using interpolative software routines, followed by median filtering and edge trimming, is done to produce the final cleaned image.

3.2.2 Data Reduction Using IRAF

The CCD reductions in this study were done with the software package IRAF. IRAF is a general Image Reduction and Analysis Facility providing a wide range of image processing tools and is a product of the NOAO.

Before a task can be executed in IRAF the user must set the task parameters to the appropriate values by executing `epar` *taskname*. Details can be found by doing a `help` *taskname* from within IRAF. For an introduction to IRAF see Barnes (1993), and for CCD reductions using IRAF see Massey (1997).

The following steps outline the reduction process:

- The exposures were examined using `implot` and the areas of the chip that contain good data as well as the overscan information were determined.
- The `setinstrument` parameters were changed to that of the instruments used in the observations, and the header translations were made valid by using `ccdhedit` and `ccdlist`.
- The individual bias frames were combined using `zerocombine` to produce an averaged combined image.
- At this stage all the frames (including flat-field images) were processed with `ccdproc` to remove the overscan and average bias and to trim the images.
- Since we were not concerned with the dark current the next step was to combine the flat-field exposures using `flatcombine` with the `scale=mode` and `reject=crreject` parameters active. This scaled the images by using the mode and rejected cosmic rays.
- The combined flat-field exposures were normalised along the dispersion axis, by dividing it by a low-order fit using `response` in the `twodspec` package.
- All the object frames were processed by dividing them by the relevant combined flat-field exposures (the normalised images) using `ccdproc`.
- The task `imexamine` was used to determine if any further corrections had to be made but that was not the case.

3.2.3 The Spectra Extraction Process

The proliferation of linear digital detectors on spectrographs, has greatly increased the astronomer's ability to perform quantitative analysis. This however, has increased demands upon the tools used for reducing these data. Astronomers want to do a mathematical optimal extraction of their spectra to achieve maximum signal-to-noise data. Extraction of a typical spectrum can be broken down into steps by following the discussion in Howell (1992) and Massey, Valdes & Barnes (1992):

1. **Find the spectrum:** This may be done manually by examining a cut along the spatial axis and indicating the appropriate peak or automatically if the relevant spectrum is the strongest peak present.

2. **Define the extraction and background windows:** This is done by specifying the size of the extraction window and the background region. These regions can also be examined upon the cut along the spatial axis.

3. **Trace the centre of the spatial profile along the dispersion axis:** Usually the spectrum will not be perpendicular to the spatial axis (or parallel to what is known as the dispersion axis). The angle made by the spectrum to the dispersion axis will differ, often significantly, from one exposure to another and should be taken into account.

4. **Sum the spectrum within the extraction window and subtract the sky:** At each point along the dispersion axis, the data within the extraction aperture are summed and the sky background is subtracted.

   At this stage a one-dimensional spectrum has been extracted from a two-dimensional image and the calibration steps should follow.

5. **Wavelength calibration:** Extract a one-dimensional spectrum from the appropriate comparison exposure using the identical aperture and trace used for the object spectrum and determine the dispersion solution for this comparison spectrum. If a second comparison exposure is to be used for providing the wavelength calibration for the object spectrum (such as interpolating in time between two comparison exposures), these steps should be repeated. Using the dispersion solution(s), the object spectrum should be put on a linear wavelength scale since many measurement tasks assume that the data are linear in wavelength.

6. **Flux calibration or normalisation:** If suitable spectrophotometric standard stars were observed, it would be possible to transform the

data to either absolute or relative flux units. It would also be possible to normalise the object spectrum so that the continuum level is unity. This is easily performed by fitting a smooth function through the continuum and dividing the spectrum by this fit. Which procedure is most applicable depends on the scientific needs. In a study of this kind, it is desirable to do flux calibration, since the line fluxes will be used to determine physical properties of the region.

3.2.4 Spectra Extraction Using IRAF

Most of the tasks necessary for extraction and wavelength calibration of spectra can be found within the `onedspec` and `twodspec` packages within `IRAF`. As each step of the extraction process is completed, an entry is made in a local subdirectory `database` in a file called `ap`*imagename*. It is through these database entries that one part of the extraction process communicates with the next.

The following steps outline the extraction and wavelength calibration process:

- The first step was to characterise the data by using `implot` to plot typical object and comparison spectra. A cut perpendicular to the dispersion axis was made to determine the base width and the full width at half maximum of the spatial profile. The task `implot` was also used to determine the overall alignment of the spectra from one end to the other.

- All the routines for extracting a spectrum have been consolidated in a single task within `IRAF` called `apall`. All of the parameters controlling the extraction aperture, the background window, the trace, the summation and background subtraction as well as parameters controlling the output can be changed with *epar* `apall`. By running `apall`, an aperture editor allows the user to change the size or the location of the extraction aperture, by changing the parameters interactively. After this was done, the interactive curve fitting routine, called `icfit` was used to inspect and alter the background window and fit. The next subroutine consisted of generating and fitting the trace, which was also done in `icfit`. This interactive routine allowed the order and function of the fit of the trace to be changed. The last subroutine in `apall` writes the apertures to the database and reviews the spectrum.

- The next step was to to convert the data on the object spectrum to a linear wavelength scale. This step also consisted of various subrou-

tines that started with the extraction of the comparison exposures with `apall`. Identical centring and trace parameters were used for the extraction of the comparison spectra which were taken before and after the object spectrum and for the object spectrum itself. The background subtraction subroutine in `apall` was unnecessary for comparison spectra. Next, `identify` was run on the comparison spectrum. This allowed the user to identify which comparison lines have what laboratory wavelength and to fit a function to these data. A text file containing the prominent Cu/Ar lines was specified in the `coordlist` parameter. The interactive dispersion function fitting was once again done in `icfit`. The second comparison spectrum can be handled very easily based upon the solution of the first comparison spectrum by using `reidentify`. Each solution was linked to the appropriate object spectrum by adding keywords `REFSPEC1`=*comparison imagename 1* and `REFSPEC2`=*comparison imagename 2* in the header of the object spectrum. The task `refspec` was then used to assign comparison spectra to an object spectrum. The final step was to apply the dispersion solution of the wavelength calibration to set the wavelength scale of the object spectrum; this was done with `dispcor`.

3.2.5 Flux Calibration Using IRAF

Spectroscopic standard stars were used to calibrate object spectra to real flux units. The standard stars that were used were selected from the ESO[2] Optical and UV Spectrophotometric Standard Stars list, and ASCII data files containing the wavelength, magnitude and bandpass used in measurement were obtained and specified in a subdirectory for each of the two standard stars.

The flux calibration was carried out by executing the following steps:

- The airmass values in the object headers were corrected to account for the effective airmass (at mid-exposure) and not for the airmass at the beginning of the exposures. This was done by running the `setairmass` routine.
- An atmospheric extinction correction was applied to the data. The atmospheric extinction table (Table 3.5) for Sutherland Observatory was obtained from the SAAO.
- For each standard star observation, the task `standard` was executed. This routine integrates the data over the appropriate bandpasses, di-

[2]European Southern Observatory.

vides by the exposure time and outputs a single file containing an observation-by-observation listing of the observed counts within each bandpass along with the standard star fluxes.

- The `sensfunc` task was executed and allows the user to interactively fit the sensitivity function as a function of wavelength using the output file from `standard`.

- The sensitivity function determined by `sensfunc` was applied to the data by running the `calibrate` task. The program spectra were corrected for atmospheric extinction (using the table entered at step 2), divided by the exposure time and finally transformed using the sensitivity curve.

Wavelength (Å)	Extinction	Wavelength (Å)	Extinction
3200	1.03	5263	0.18
3250	0.97	5556	0.15
3300	0.92	5840	0.13
3350	0.87	6056	0.12
3400	0.82	6436	0.10
3450	0.78	6790	0.08
3500	0.74	7100	0.07
3571	0.68	7550	0.06
3636	0.64	7780	0.06
3704	0.60	8090	0.05
3862	0.51	8370	0.05
4036	0.44	8708	0.05
4167	0.39	9832	0.04
4255	0.36	10256	0.03
4464	0.31	10400	0.03
4566	0.28	10610	0.03
4785	0.24	10796	0.03
5000	0.21	10870	0.03

Table 3.5: Extinction coefficients for Sutherland Observatory.

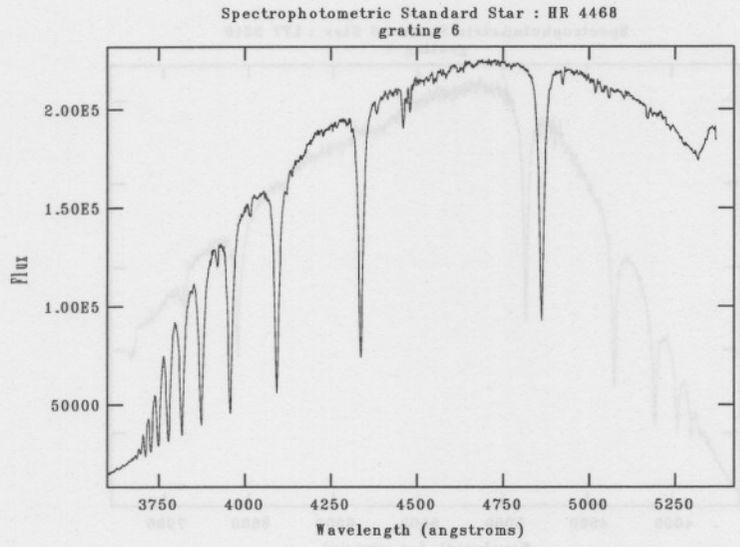

Figure 3.5: Standard star: HR 4468.

3.3 Supplementary Spectra

3.3.1 Standard Star Spectra

Figures 3.5 and 3.6 show examples of the spectra from the two standard stars that were used to calibrate the object spectra to real flux units. The flux density units (y-axis) are erg $s^{-1}cm^{-2}Å^{-1}$. The information on these spectrophotometric standard stars can be found in Table 3.4.

Both of these standard star spectra illustrate the Balmer series beautifully. Figure 3.5 shows the Balmer lines from the $n = 4 \rightarrow 2$ transition (Hβ at λ4861 Å) to the higher order Balmer lines. In Figure 3.6, the transitions from $n = 3 \rightarrow 2$ (Hα at λ6563 Å) to the higher order transitions can be seen. LTT 3218 in Figure 3.6 is a DA-type star, which means that it is a white dwarf with very strong hydrogen lines. HR 4468 in Figure 3.5 is a B9.5V-type star, which means that it is a star in a cooler subclass (9.5) of the hot B-type stars and it is of luminosity class V (main sequence). Between the strong Balmer lines, some neutral He I lines can also be seen in this spectrum, for example the two small absorption lines at approximately 4450 Å, between Hβ and Hγ.

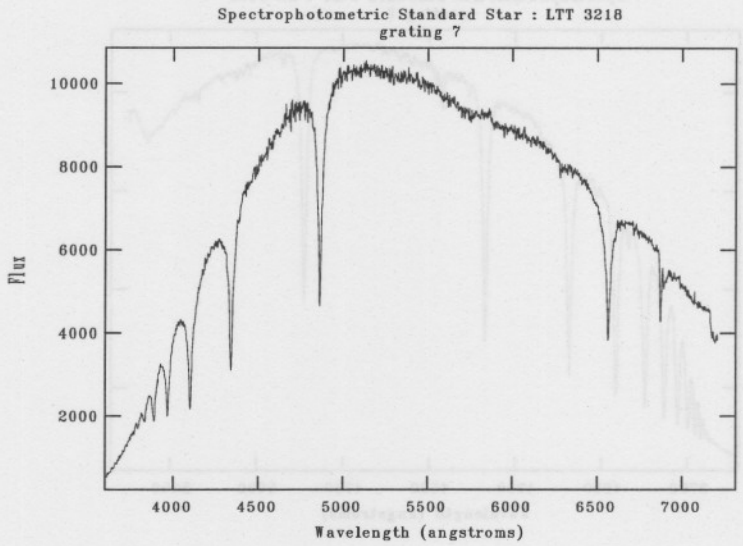

Figure 3.6: Standard star: LTT 3218.

3.3.2 Sky Spectra

For the BCGs, it was found that a background spectrum could easily be defined and subtracted from a spectrum. As an illustration, consider Figure 3.7. This figure consists of three spectra, of which the upper spectrum is a sky spectrum, the middle one is a grating 7 spectrum of Tol 2 before the background was subtracted, and the lower one is the same spectrum of Tol 2 after the background has been subtracted. The y-axis is not on the same scale. From spectra like these, object emission lines and sky emission lines can be identified.

For the H II regions, background subtraction was a lot more difficult since the object extended throughout the whole slit. For the middle region of the nebula NGC 3603, background subtraction was possible and done in the conventional manner, as described earlier. For the upper and lower regions of NGC 3603, as well as for the nebula NGC 3576, conventional background subtraction was not possible. However, from investigation of the sky spectra and the spectra where background subtraction was possible, the wavelength of the sky lines and their effect on the object spectra can be inferred.

It was also found that it is difficult to obtain sky spectra where just sky lines are present, since pointing the telescope to a region that looks like clear sky on the acquisition camera, may in fact contain objects that influence the spectrum. This is especially true for objects in the galactic plane like NGC 3603 and NGC 3576.

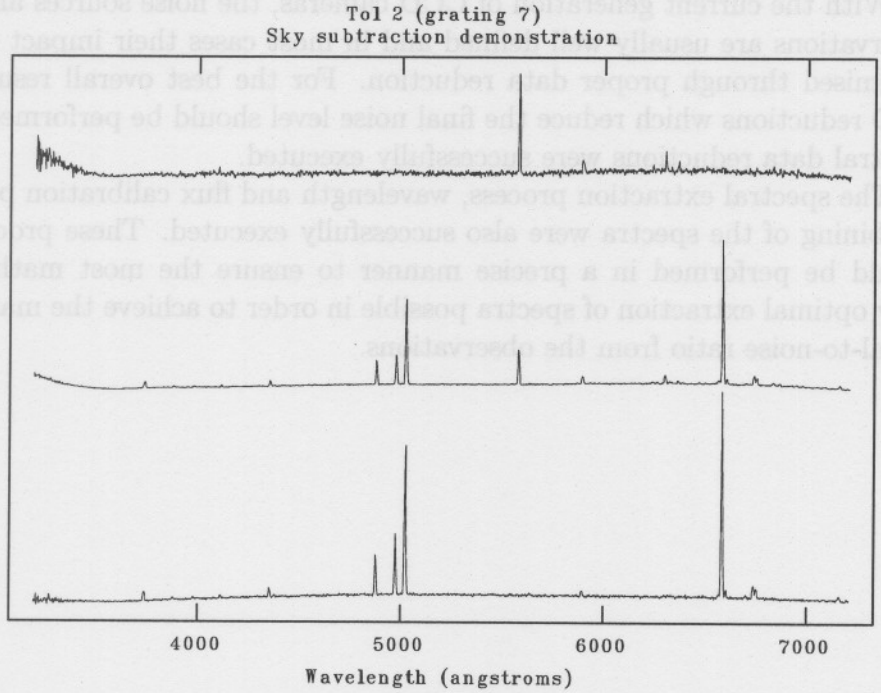

Figure 3.7: Background subtraction demonstration. The upper spectrum is a sky spectrum, the middle spectrum is a grating 7 spectrum of Tol 2 before background was subtracted, and the lower spectrum is the same spectrum of Tol 2 after the background has been subtracted.

3.4 Summary

Sound knowledge of the spectroscope (and its components) is a basic requirement in order to optimise the use thereof for a particular project. The choice of grating, slit width and slit placement on the objects will depend on the scientific need and can determine the success of the observation run. The observation of the objects and the collection of all the calibration spectra necessary for this study were successfully conducted.

With the current generation of CCD cameras, the noise sources affecting observations are usually well defined and in most cases their impact can be minimised through proper data reduction. For the best overall results, all CCD reductions which reduce the final noise level should be performed. The spectral data reductions were successfully executed.

The spectral extraction process, wavelength and flux calibration plus the combining of the spectra were also successfully executed. These procedures should be performed in a precise manner to ensure the most mathematically optimal extraction of spectra possible in order to achieve the maximum signal-to-noise ratio from the observations.

Chapter 4

Nebular Analysis

This chapter consists of a detailed account of how the emission lines of the five BCGs were identified and how their properties were measured. Identification and measurement of the emission lines made the interstellar reddening and Doppler correction possible, whereafter all the emission lines were measured again and their properties tabulated. The measurements of the five BCGs, together with the spectra of all seven objects are presented and discussed in this chapter. Prior to the temperature and density determinations of the five BCGs, a condition was tested which proved that the five galaxies were indeed correctly classified as star formation galaxies. The oxygen abundance of galaxies serve as metallicity indicators and these have been determined using three different methods. After other chemical abundances are presented, an account into the investigation of suitable nebular analysis software follows.

4.1 Identifying and Measuring Emission Lines

Most of the nebular analysis described in this chapter was performed within the `IRAF` software package. The `splot` task, located in the `onedspec` package, was used extensively to combine the spectra as well as to analyse and measure features of the spectra.

4.1.1 Centroid, Flux and Equivalent Width Determinations

There exist various techniques to measure equivalent widths and other line profile parameters in `splot`. The technique used most, consisted simply of the integration of the pixel values between two marked pixels. The user interactively marks the two edges of the emission line at the continuum. The

measured line centre, continuum value, line flux and equivalent width are then given by:

$$centre = \frac{\sum(w(i) \times (I(i) - C(i))^{\frac{3}{2}})}{\sum((I(i) - C(i))^{\frac{3}{2}})} \tag{4.1}$$

$$continuum = C(midpoint) \tag{4.2}$$

$$flux = \sum((I(i) - C(i)) \times (w(i2) - w(i1))/(i2 - i1)) \tag{4.3}$$

$$eq.width = \sum(1 - I(i)/C(i)) \tag{4.4}$$

where $w(i)$ is the wavelength of pixel i, $i1$ and $i2$ are the nearest integer pixel limits of the integrated wavelength range, $I(i)$ is the data value of pixel i, $C(i)$ is the continuum at pixel i and the sum is over the marked range of pixels. The continuum is a linear interpolation between the two points marked.

For the above method the flux is directly integrated but for some of the lines such as Hα which lies between the two [N II] lines, as well as the two [S II] lines which are very close together, a more complex method was applied. These lines were blended and Gaussian profiles were fitted with a linear background. Two cursor positions, given as input by the user, define the region to be fit and a fixed linear continuum. The profile centre, peak strength and equivalent width were then determined.

The integrated, reddening corrected fluxes measured with both the methods are in the units of erg $s^{-1}cm^{-2}$, and the integration is done in the same units as the plotted scale (x-axis: wavelength (Å) and y-axis: flux density (erg $s^{-1}cm^{-2}Å^{-1}$)).

Error estimates were found by using a Poisson statistics model of the data. The model parameters are a constant Gaussian sigma (a standard deviation estimate derived from the noise on the continuum of the spectrum) and an inverse gain (allows the error estimate to change as a linear function with wavelength) as specified by the parameters σ_0 and `invgain`. The parameters are used to compute the pixel value σ from the following formula:

$$\sigma^2 = \sigma_0^2 + invgain \times I \tag{4.5}$$

where I is the pixel value. The number of error estimates was set to 100. The noise model for the processed spectra was not the same as the detector readout noise and gain. These parameters were estimated from the statistics of the spectra. An inverse gain, instead of a direct gain, was used to allow a value of zero; this provides the model with constant uncertainties over the wavelength range. The standard deviation does vary over wavelength but was computed from each spectrum in the general region of the emission line to

be measured manually and set accordingly in the `splot` parameters. These error estimates are one sigma estimates.

4.1.2 Identifying Emission Lines

The "Atomic Line List v2.04", which is obtainable on the internet, was used to identify the emission lines on the spectra. The atomic line list is hosted by the Department of Physics and Astronomy at the University of Kentucky and is maintained by Peter van Hoof from the Royal Observatory of Belgium. It is a compilation of approximately 923 000 allowed, intercombination and forbidden atomic transitions with the wavelengths in the range from 0.5 Å to 1000 μm. Its primary intention is to allow the identification of observed atomic absorption or emission features. Most of the atomic energy level data have been taken from the Atomic Spectra Database provided by the National Institute of Standards and Technology (NIST).

The wavelengths of the lesser known emission lines were measured and given as input (together with a reasonable error interval). The additional selection criteria were set to transitions in nebulae with the medium set to air. When more than one possible line was given as output, additional information on the relevant transitions, such as the transition probability, was considered in order to identify the line.

The identified emission lines are indicated on the spectra which are presented later in this chapter. All measurements taken of the identified emission lines are tabulated with the spectra; some of the lines are used in the nebular analysis which follows later in this chapter.

4.2 Corrections

4.2.1 Interstellar Reddening

Gaseous nebulae contain dust particles in addition to gas and the effects of this dust are by no means negligible.

The most obvious effect of interstellar dust is its extinction of the light from distant stars and nebulae. This extinction in the ordinary optical region is due largely to scattering but is also partly due to absorption. It reduces the amount of light from a source shining through interstellar dust according to the equation

$$I_\lambda = I_{\lambda 0} \exp^{-\tau_\lambda} \tag{4.6}$$

where $I_{\lambda 0}$ is the intensity that would be received at Earth in the absence of interstellar extinction along the line of sight, λ is the wavelength, I_λ is the inten-

sity actually observed and τ_λ is the optical depth at the observed wavelength. Interstellar extinction increases towards shorter wavelengths. How much a source is extinguished at any wavelength λ is quantified by the monochromatic extinction $A(\lambda)$, which is the difference between the monochromatic magnitude of the source at wavelength λ and the magnitude of the source which would be observed at the same wavelength in the absence of dust. The difference in extinction between two wavelengths is referred to as reddening.

The form of wavelength dependence of the interstellar extinction in the ordinary optical region is approximately the same for all stars and only the amount of extinction varies, so that

$$\tau_\lambda = Cf(\lambda) \tag{4.7}$$

where the constant factor C depends on the star but the function $f(\lambda)$ is the same for all stars (Osterbrock 1989). This implies physically that the optical properties of dust are similar everywhere in the observed region of interstellar space. Although this standard form of interstellar extinction is a good first approximation, careful observations of different stars reveal variations in the wavelength dependence of the interstellar extinction along different lines of sight in the Galaxy. These differences are small but not insignificant. Some authors, for example Carnochan (1986), even warn that variations from the mean extinction law are so common that the adoption of a mean extinction curve for the correction of interstellar reddening can be dangerous. This is particularly true in the UV spectral region.

Interstellar extinction naturally makes the observed ratio of intensities of two emission lines $I_{\lambda_1}/I_{\lambda_2}$ differ from their ratio as emitted in the nebula $I_{\lambda_1 0}/I_{\lambda_2 0}$ according to:

$$\frac{I_{\lambda_1}}{I_{\lambda_2}} = \frac{I_{\lambda_1 0}}{I_{\lambda_2 0}} \exp^{-(\tau_{\lambda_1} - \tau_{\lambda_2})} \tag{4.8}$$

The data from the observations must therefore be corrected for interstellar extinction before they can be discussed physically.

As a first approximation, the interstellar extinction can ordinarily be assumed to have the average form, unless the amount is very large, so that this ratio can also be written as

$$\frac{I_{\lambda_1}}{I_{\lambda_2}} = \frac{I_{\lambda_1 0}}{I_{\lambda_2 0}} \exp^{-C(f_{\lambda_1} - f_{\lambda_2})} \tag{4.9}$$

Then, it is often convenient to write

$$\frac{I_{\lambda_1}}{I_{\lambda_2}} = \frac{I_{\lambda_1 0}}{I_{\lambda_2 0}} 10^{-c(f_{\lambda_1} - f_{\lambda_2})} \tag{4.10}$$

where $c = \log e \times C = 0.434 \times C$ and is called the logarithmic extinction coefficient.

To find the amount of extinction, the principle is to use the measured ratio of strengths of two lines for which the relative intensities, as emitted in the nebula, are known independently — thus, only C is unknown and can be determined. Once C is known, the average reddening curve, $f(\lambda)$, gives the optical depths at all wavelengths. The ideal line ratio to determine the amount of extinction would be the one that is completely independent of physical conditions and is easy to measure in all nebulae. Such an ideal pair of lines does not exist in nature but various approximations exist and can be used to obtain a good estimate of the interstellar extinction of a nebula.

The method most frequently used in practice to determine the interstellar extinction is to measure the ratio of two or more H I Balmer lines, for instance, Hα/Hβ and Hβ/Hγ. The Balmer lines are strong and occur in the part of the spectrum that is ordinarily observed. For the approximation $T_e = 10^4$ K and $N_e = 10^2$ cm^{-3} (the case B approximation):

$$\frac{I(\mathrm{H}\alpha)}{I(\mathrm{H}\beta)} = 2.87 \tag{4.11}$$

$$\frac{I(\mathrm{H}\gamma)}{I(\mathrm{H}\beta)} = 0.47 \tag{4.12}$$

A change in temperature to 20 000 K only alters $I(\mathrm{H}\alpha)/I(\mathrm{H}\beta) = 2.87$ to 2.69, and the effect of a doubling in electron density is smaller still (Emerson 1997). Thus the ratio of line intensities in a recombination cascade is essentially fixed irrespective of temperature and density. The ratio of the Balmer line intensities

$$I(\mathrm{H}\alpha) : I(\mathrm{H}\beta) : I(\mathrm{H}\gamma) \tag{4.13}$$

is called the Balmer decrement. A problem with the Balmer-line method is the large uncertainty in the measured strengths of Hγ and Hδ, due to their intrinsic weakness and because they can be strongly affected by the underlying stellar Balmer absorption lines. Nebulae are observed to differ greatly in the amount of extinction, for instance, $c(\mathrm{H}\beta) \approx 0.02$ for NGC 6853, while one of the most heavily reddened planetary nebula for which optical observations have been made is NGC 6369, with $c(\mathrm{H}\beta) \approx 2.3$ (Osterbrock 1989). $c(\mathrm{H}\beta)$ is called the logarithmic extinction at Hβ.

The `deredden` task in `IRAF` was used to correct the input spectra for interstellar extinction by using the empirical selective extinction function of Cardelli et al. (1989). This extinction function is valid over the wavelength range 3.5 μm $\geq \lambda \geq$ 0.125 μm, and is applicable to both the diffuse and dense regions of the ISM. The analytical formula has been divided into three wavelength regions (infrared, optical/near-infrared and UV) by Cardelli et al. (1989), mainly for computational reasons. The formula for the monochromatic extinction, $A(\lambda)$, in the optical/NIR region (3000 Å to 9000 Å) is given by:

$$\frac{A(\lambda)}{A_V} = a(x) + \frac{b(x)}{R_V} \tag{4.14}$$

with

$$a(x) = 1 + 0.17699y - 0.50477y^2 - 0.02427y^3 + 0.72085y^4 \tag{4.15}$$
$$+0.01979y^5 - 0.77530y^6 + 0.32999y^7$$

and

$$b(x) = 1.41338y + 2.28305y^2 + 1.07233y^3 - 5.38434y^4 \tag{4.16}$$
$$-0.62251y^5 + 5.30260y^6 - 2.09002y^7$$

and where

$$x \equiv \frac{1}{\lambda(\mu\mathrm{m}^{-1})} \tag{4.17}$$

and

$$y = (x - 1.82) \tag{4.18}$$

for

$$1.1\ \mu\mathrm{m}^{-1} \leq x \leq 3.3\ \mu\mathrm{m}^{-1} \tag{4.19}$$

The quantities R_V and A_V are described below.

The `deredden` task requires two parameters: the absolute extinction at 5550 Å, A_V, and the ratio R_V, of this extinction to the colour excess between 4350 Å and 5550 Å, $E(B-V)$. One of the input task parameters is R_V, which has a value of 3.1 for the ISM (Cardelli et al. 1989). The second input parameter can be A_V, $E(B-V)$ or $c(\mathrm{H}\beta)$. If either one of the latter two are provided then A_V can be calculated.

To evaluate the value of $c(\mathrm{H}\beta)$ for every galaxy, the following procedure was used:

- The fluxes and wavelengths of the Hα and Hβ lines were measured with `splot`. The wavelengths were measured since they did not occur exactly at their rest wavelength but at a Doppler shifted wavelength, and this had to be taken into account[1]. The grating 7 spectra were used, since Hα falls outside the wavelength range of grating 6, and the Hγ fluxes in the spectra are strongly affected by underlying absorption.

- The extinction function was evaluated and the values used to construct the interstellar extinction curve, both with the aid of a graphics package. This curve can be seen in Figure 4.1; thus, the value of the extinction curve at any wavelength can easily be found.

- The ratio of the measured fluxes (the same as the ratio of the intensities), $\frac{I(\mathrm{H}\alpha)}{I(\mathrm{H}\beta)}$, and the value of the extinction curve at the measured wavelength of Hα and Hβ, $f(\mathrm{H}\alpha)$ and $f(\mathrm{H}\beta)$ were substituted in the equation:

$$\log \frac{I(\mathrm{H}\alpha)}{I(\mathrm{H}\beta)} - \log \frac{I_0(\mathrm{H}\alpha)}{I_0(\mathrm{H}\beta)} = -c(\mathrm{H}\beta) \times (f(\mathrm{H}\alpha) - f(\mathrm{H}\beta)) \qquad (4.20)$$

  where $\frac{I_0(\mathrm{H}\alpha)}{I_0(\mathrm{H}\beta)} = 2.87$. This leads to the values of $c(\mathrm{H}\beta)$ shown in Table 4.1.

BCG	$c(\mathrm{H}\beta)$
Zw 0855	0.064±0.006
Mrk 1267	0.435±0.004
II Zw 33	0.244±0.007
Tol 2	0.154±0.002
Tol 3	0.069±0.001

Table 4.1: The values of the logarithmic extinction coefficient at Hβ.

[1]This implies that all the extinction occurs outside of the BCGs. Normally, astronomers assume that all of the extinguishing dust is in the foreground, partly because of suspicions that any dust that once existed within the harsh environment of the nebula itself would have been destroyed. However the possibility that there may be dust mixed with the emitting gas cannot be excluded.

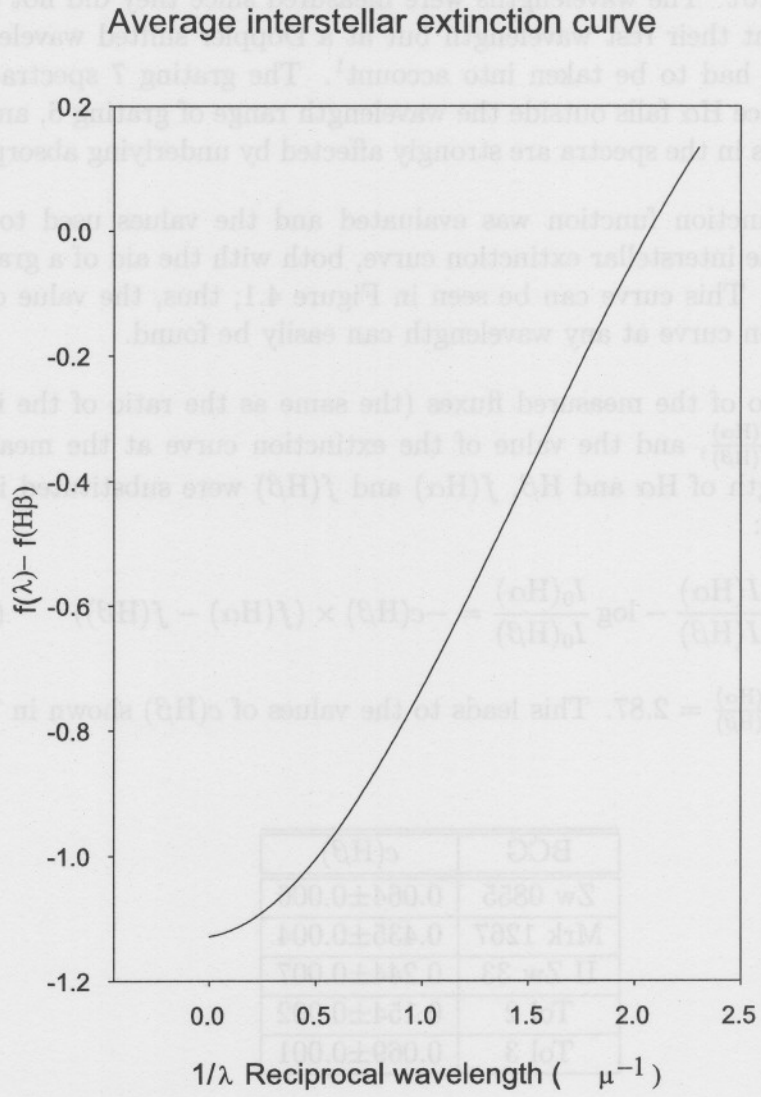

Figure 4.1: The extinction curve. The y-axis scale gives extinction relative to extinction at Hβ, and the extinction is plotted in terms of reciprocal wavelength because it is nearly linear in this variable.

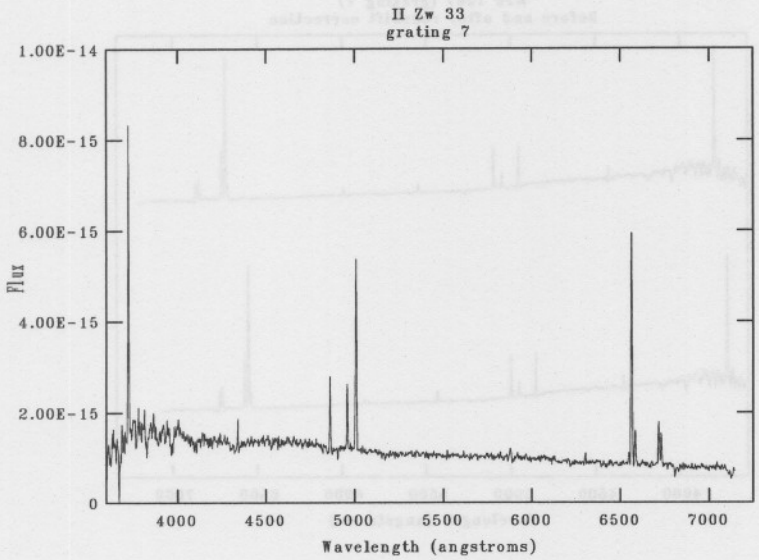

Figure 4.2: II Zw 33 before interstellar reddening correction. The flux density (y-axis) unit is erg $s^{-1}cm^{-2}Å^{-1}$.

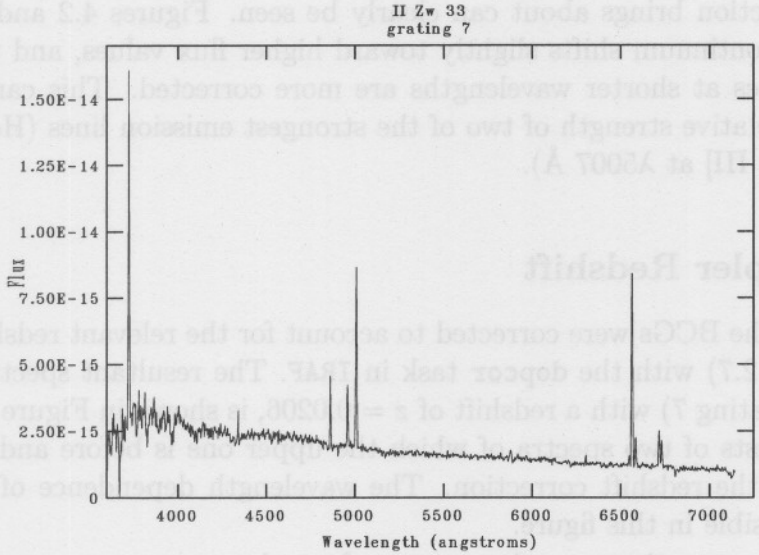

Figure 4.3: II Zw 33 after interstellar reddening correction. Note the change in the continuum level as well as the change in the relative intensities between two of the strongest emission lines: Hα at λ6563 Å and [O III] at λ5007 Å.

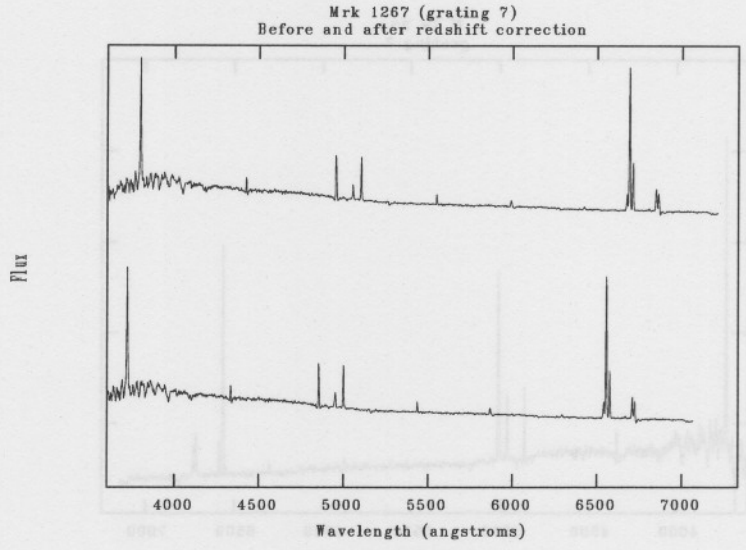

Figure 4.4: Mrk 1267. Before and after the redshift correction.

Figures 4.2 and 4.3 show spectra of II Zw 33 before and after the interstellar reddening correction. From these spectra, the change that the interstellar reddening correction brings about can clearly be seen. Figures 4.2 and 4.3 show that the continuum shifts slightly toward higher flux values, and that the emission lines at shorter wavelengths are more corrected. This can be seen from the relative strength of two of the strongest emission lines (Hα at λ6563 Å and [O III] at λ5007 Å).

4.2.2 Doppler Redshift

The spectra of the BCGs were corrected to account for the relevant redshifts (given in Table 2.7) with the `dopcor` task in `IRAF`. The resultant spectrum of Mrk 1267 (grating 7) with a redshift of $z = 0.0206$, is shown in Figure 4.4. The figure consists of two spectra of which the upper one is before and the lower one after the redshift correction. The wavelength dependence of the shift is easily visible in this figure.

The Doppler correction procedure was performed:

- on a set of spectra from the five BCGs that had not been reddening corrected
- on a set of spectra that had been reddening corrected.

This was necessary in order to measure the emission-line flux before and after the reddening correction.

The Doppler shifts were measured from the combined observed spectra, by measuring the wavelengths of two strong lines ([O II] at λ3727 Å and Hα at λ6563 Å) at different ends of the observed spectrum. The average redshifts of these two measured lines compared very well with those obtained in the literature (Kong & Cheng 2002a; Simbad Astronomical Database). The minor discrepancies are fully ascribable to measurement errors due to using the `IRAF` task, `splot`, interactively, as well as the spectral resolution of the spectroscope used in observations. As stated in section 3.1.4, the use of a comparison spectrum enables the Doppler shift to be calculated to an accuracy of z=0.0007 for grating 7, under ideal conditions. The redshifts are presented in Table 4.2 (errors indicated on measurements are the standard deviations on the averages and do not include the instrumental uncertainty of z=0.0007).

Galaxy	Average measured z	Value of z from literature
Zw 0855	0.0115±0.0016	0.0104[a]
Mrk 1267	0.0190±0.0005	0.0206[a]
II Zw 33	0.0090±0.0004	0.0095[a]
Tol 2	0.0036±0.0013	0.0032[b]
Tol 3	0.0029±0.0006	0.0036[b]

Table 4.2: Redshifts of the BCGs. References: *a* is from Kong & Cheng (2002a) and *b* is from Simbad Astronomical Database.

4.3 Galactic H II Regions

The spectra obtained for the two galactic H II regions are shown and discussed in this section. The various nebular analysis techniques, such as the derivation of the temperature and density of the region, that follows later in this chapter, were not applied to the galactic H II regions. This is not only because it proved very difficult to properly subtract the background sky from all of the spectra, as these extended regions filled the whole slit, but also because of the underlying stellar absorption (particularly in the case of NGC 3603). However, as stated previously, there is no difference in the procedure of these methods if it is being applied to galactic H II regions or extragalactic H II regions, but biased results would have been achieved. The spectra shown in this section were obtained after the flux calibration procedure.

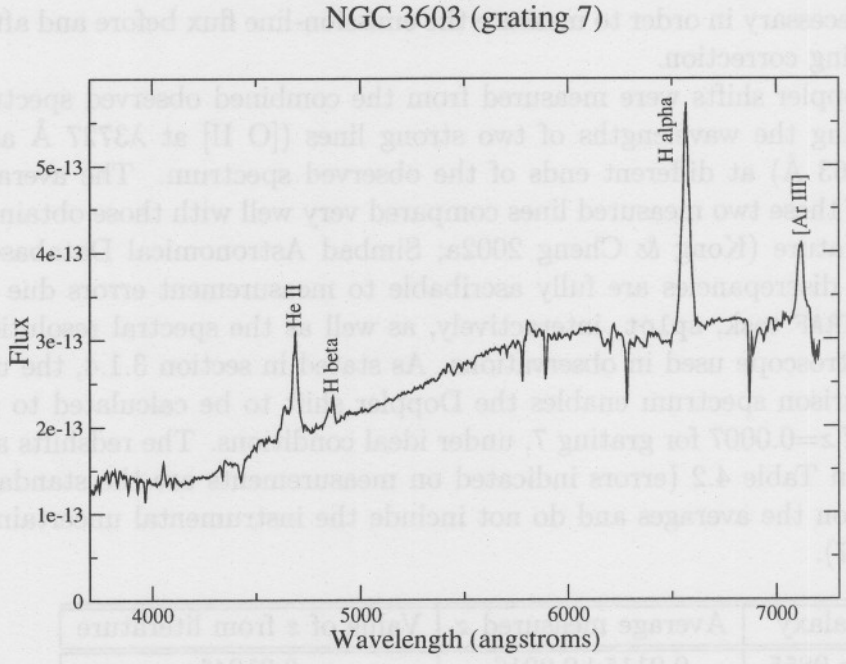

Figure 4.5: Spectrum of the middle part of NGC 3603.

4.3.1 NGC 3603

Even when a nearby nebula, such as NGC 3603, is observed, where the slit can be placed away from stars, light from stars may still enter the spectrograph as a consequence of scattering off dust mixed with the gas. Although there may be astrophysical information about the environment contained in a stellar continuum, its presence leads to problems in analysing nebular emission lines. This is because the stellar spectrum is crossed with absorption lines, some of which underlie key nebular lines. Forbidden lines are extremely weak in absorption, so nebular recombination lines are the primary lines affected. Paramount among them are the Balmer lines of hydrogen, which as can be seen in some of the spectra, appears suppressed as they fill in the underlying Balmer absorption lines in the stellar continuum. The underlying stellar absorption is the main reason why this object proved to be not suitable for an emission-line analysis study. This region, NGC 3603, is a giant OB star cluster and the spectra are therefore mainly stellar absorption spectra with a few strong emission lines superimposed.

As mentioned before, spectra were taken of three different regions, the middle, the upper and the lower part of this object (the middle, upper and lower part is in reference to Figure 3.3 e). The spectra of these regions of NGC 3603 are shown in Figures 4.5, 4.6 and 4.7, respectively (where the flux

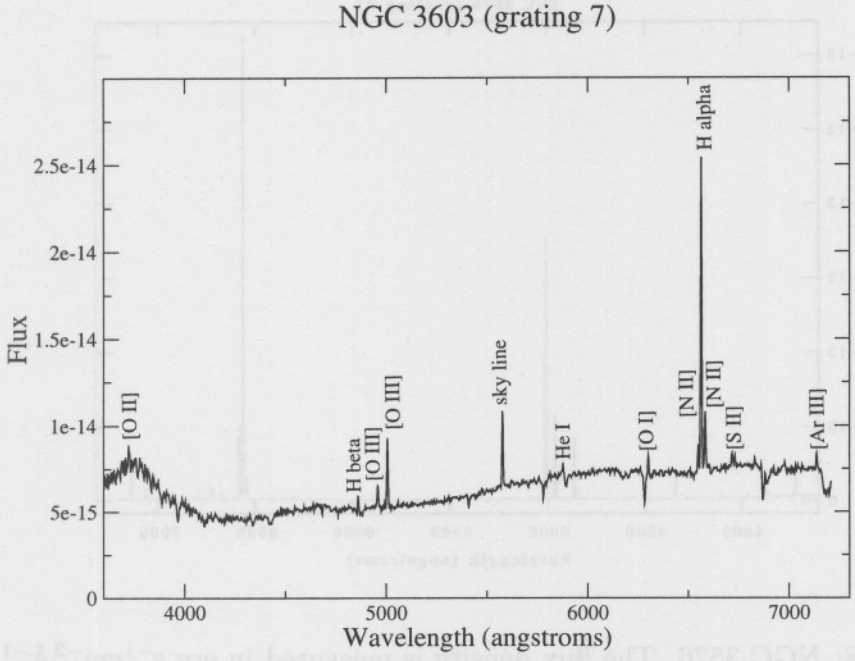

Figure 4.6: Spectrum of the upper part of NGC 3603.

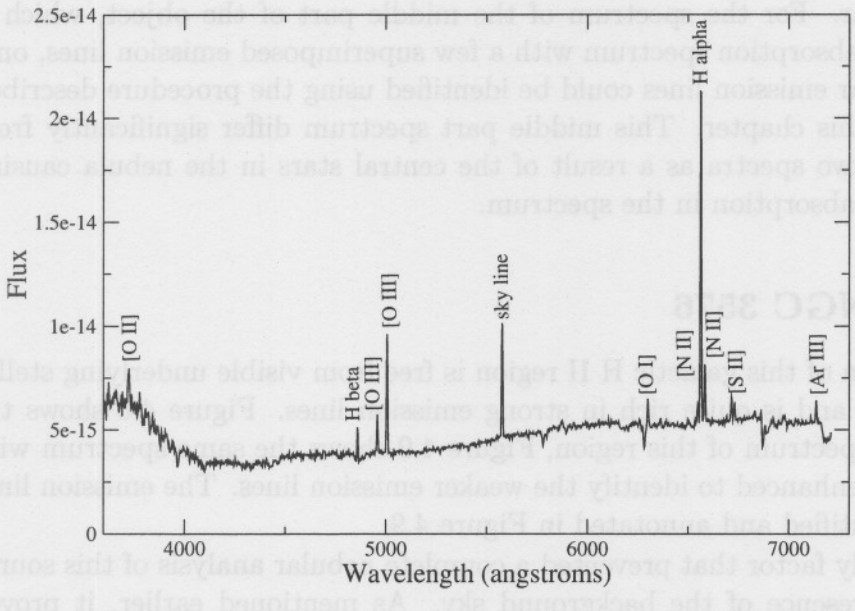

Figure 4.7: Spectrum of the lower part of NGC 3603.

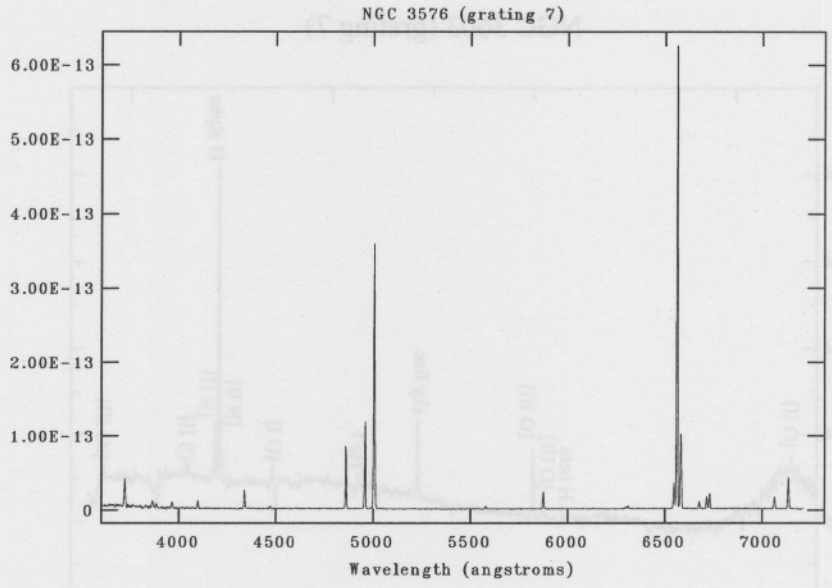

Figure 4.8: NGC 3576. The flux density is measured in erg $s^{-1}cm^{-2}Å^{-1}$.

density on the y-axis is measured in erg $s^{-1}cm^{-2}Å^{-1}$). For the spectra of the upper and the lower part of the object, the emission lines as well as a sky line, were identified and indicated on the spectra. These two spectra are very similar. For the spectrum of the middle part of the object, which is mostly an absorption spectrum with a few superimposed emission lines, only four nebular emission lines could be identified using the procedure described earlier in this chapter. This middle part spectrum differ significantly from the other two spectra as a result of the central stars in the nebula causing the stellar absorption in the spectrum.

4.3.2 NGC 3576

The spectra of this galactic H II region is free from visible underlying stellar absorption and is quite rich in strong emission lines. Figure 4.8 shows the grating 7 spectrum of this region, Figure 4.9 shows the same spectrum with the y-axis enhanced to identify the weaker emission lines. The emission lines are all identified and annotated in Figure 4.9.

The only factor that prevented a complete nebular analysis of this source was the presence of the background sky. As mentioned earlier, it proved impossible to subtract the background from this extended source as it filled the whole slit. It was also very difficult to obtain a sky spectrum near this

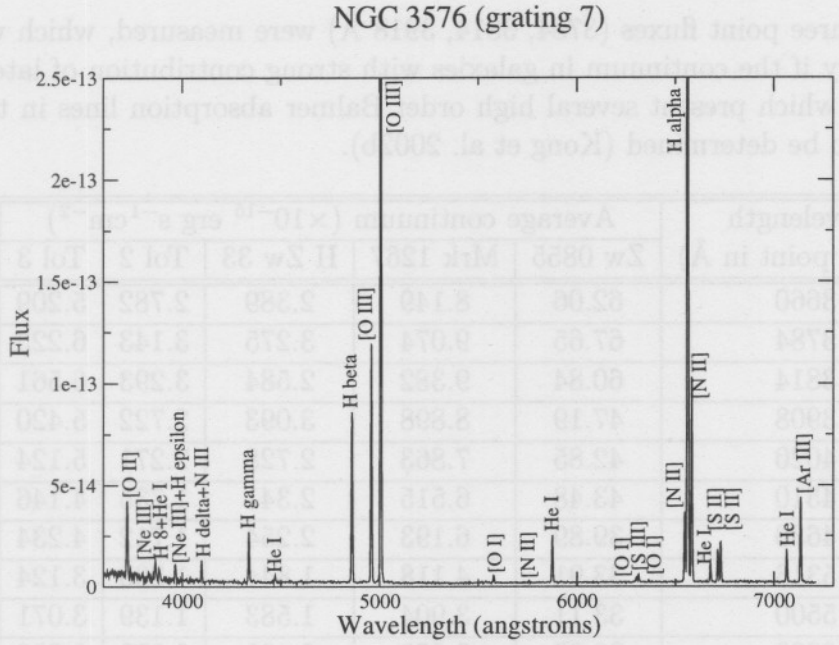

Figure 4.9: NGC 3576 with y-axis scaled to enhance emission lines.

source (in the galactic plane), as pointing the telescope to a region that looks like clear sky on the acquisition camera, may contain objects. However, it can be seen that the [O III]λ4363 line is absent, which indicates that this source does not have a very low metallicity (compared to solar metallicity). Kobulnicky, Kennicutt & Pizagno (1999) states that [O III]λ4363 is generally detected only in galaxies with $12 + \log(\frac{O}{H}) \leq 8.4$, which is roughly equivalent to $Z \leq 0.3 Z_{\odot}$. The absence of the [O III]λ4363 line can also be due to a low temperature, large extinction at the blue end of the spectrum due to dust, or a poor signal-to-noise ratio. However the latter two are improbable since relatively weak lines in the blue end of the spectrum can still be seen.

4.4 Blue Compact Galaxies

The Continuum

Table 4.3 lists the continuum values which were measured for each galaxy. In order to derive the continuum, the reddening corrected fluxes at nine pivot points were measured, i.e. at 3660, 4020, 4510, 4630, 5313, 5500, 6080, 6630, 7043 Å. These points were chosen to avoid regions of strong emission or absorption features (Kong et al. 2002b). The corresponding fluxes were determined as averages in 20 Å bins centred on the listed wavelengths. In

addition, three point fluxes (3784, 3814, 3918 Å) were measured, which will be necessary if the continuum in galaxies with strong contribution of late B to F stars, which present several high order Balmer absorption lines in this region, is to be determined (Kong et al. 2002b).

Wavelength	Average continuum ($\times 10^{-15}$ erg s^{-1}cm^{-2})				
(centre point in Å)	Zw 0855	Mrk 1267	II Zw 33	Tol 2	Tol 3
3660	62.06	8.149	2.389	2.782	5.209
3784	67.65	9.074	3.275	3.143	6.223
3814	60.84	9.382	2.584	3.293	6.561
3908	47.19	8.898	3.093	2.722	5.420
4020	42.85	7.863	2.728	2.271	5.124
4510	43.48	6.515	2.341	1.735	4.146
4630	39.89	6.193	2.254	1.712	4.234
5313	33.91	4.118	1.844	1.300	3.124
5500	33.11	3.904	1.583	1.139	3.071
6080	29.23	3.359	1.439	0.973	2.836
6630	26.33	2.739	1.190	0.782	2.438
7043	23.43	2.493	1.029	0.676	2.264

Table 4.3: The average continuum values.

Gaseous nebulae are usually transparent in the continuum, at least in the visible region of the spectrum. Except at very long and very short wavelengths, continuum emission does not reach the black-body level appropriate to the local continuum temperature, so that the lines appear as emission lines. Some of the continuum in nebulae may be due to faint background stars but a component is produced by the atomic processes of the nebula itself. Part of the nebular continuum is caused by the free-bound (recombination) and free-free (bremsstrahlung) processes in the nebula. Most of it however, is produced by the so-called two-photon process[2]. Usually, an electron in hydrogen's level $n = 2$ will simply jump to level $n = 1$ with the production of the Lyman-α line at λ1216 Å. However it is also possible that two photons can be emitted simultaneously. Thus, the two-photon process involves transitions from the $n = 2, l = 1$ level of hydrogen to the $n = 1, l = 0$ ground state. The sum of their energies must equal that of a Lyman-α photon, but otherwise there are no restrictions; the energy can be divided in any way between the two photons. The result is a continuum that pervades the

[2]See Dopita & Sutherland (2003) or Osterbrock (1989) for a detailed analysis of this process, including the transition probability.

spectrum with a limit at 1216 Å and peaks at about 2431 Å (Osterbrock 1989). Thus the peak emission occurs at a wavelength corresponding to half the energy of the Lyman-α transition. The probability distribution of the emitted photons is therefore symmetric around λ=2431 Å. Since a Lyman-α photon, once created, will suffer numerous successive re-absorptions and re-emissions as it tries to work its way out of the nebula, the odds of it breaking down into two photons become reasonably good and a strong continuum is produced. A similar process in ionised helium will produce additional continuous radiation in the spectra of planetary nebulae down to He II at λ304 Å, although the ionising stars in H II regions are too cool to produce He^+ (Kaler 1989).

The Emission Lines

In this section, the basic spectral line results of the five BCGs are listed individually. The observed emission-line fluxes are listed (measured from spectra that have been Doppler corrected but not reddening corrected) in units of erg $s^{-1}cm^{-2}$. In the same table, the reddening corrected line fluxes are also listed (measured from reddening corrected, Doppler corrected spectra) in the same units of erg $s^{-1}cm^{-2}$. The reddening corrected line flux I is related to the observed line flux F by

$$I(\lambda) = F(\lambda) \times 10^{-cf_\lambda} \tag{4.21}$$

where $c(H\beta)$ is the logarithmic extinction constant for each galaxy (Table 4.1) and f_λ is the extinction function by Cardelli et al. (1989). The equivalent widths (in Å) were also measured from the reddening corrected spectra.

In the spectra of Mrk 1267 and II Zw 33, some absorption features were detected. The equivalent widths of these features are tabulated in the respective subsections. The equivalent widths of these absorption features are positive, while those of emission features are negative (see definition of equivalent width in chapter 2). The absolute values of the equivalent widths are listed in the tables, whether it is absorption or emission lines will be clear from the context.

For each galaxy, a table containing the results of the calculation of some of the important ratios and metallicity indices was also created, as these specific ratios are used in the nebular analysis that follows. The combined grating 7 spectrum of each galaxy is also shown, as well as a version of the same spectrum where the y-axis is scaled differently in order to identify weaker emission lines. The noise increases towards the shorter wavelengths, thus the errors in the measurements increases correspondingly.

4.4.1 Zw 0855

No.	Line	λ (Å)	Observed Flux $\times 10^{-15}$	Corrected Flux $\times 10^{-15}$	Equivalent width (Å)
1	[S II]	6731	4.18±0.17	4.55±0.18	16.35±0.65
2	[S II]	6717	6.01±0.17	6.56±0.17	23.15±0.61
3	[N II]	6584	6.35±0.17	6.66±0.16	21.89±0.54
4	Hα	6563	43.88±0.18	48.07±0.19	152.30±0.60
5	[N II]	6548	2.12±0.18	2.79±0.17	9.23±0.58
6	[S III]	6312	0.61±0.16	0.77±0.17	2.81±0.63
7	He I	5876	1.38±0.17	1.51±0.18	4.73±0.55
8	[O III]	5007	29.39±0.23	32.90±0.22	84.07±0.55
9	[O III]	4959	10.35±0.18	11.61±0.19	29.89±0.49
10	Hβ	4861	14.47±0.18	16.37±0.18	39.90±0.44
11	He I	4472	0.81±0.75	0.98±0.80	2.36±1.90
12	[O III]	4363	0.75±0.75	1.05±0.75	2.42±1.75
13	Hγ	4340	5.41±0.75	6.27±0.80	14.29±1.75
14	Hδ + N III	4102	2.77±1.50	3.11±1.50	8.02±3.70
15	[Ne III] + Hϵ	3969	2.85±1.80	2.56±1.60	5.37±3.50
16	H8 + He I	3889	1.82±1.50	2.37±1.80	5.24±3.90
17	[Ne III]	3869	2.71±1.50	3.05±1.60	6.40±3.40
18	[O II]	3727	63.26±1.90	77.90±2.10	139.40±4.10

Table 4.4: Emission-line measurements of Zw 0855 (flux in erg $s^{-1}cm^{-2}$).

Zw 0855 formed part of the BCG survey, containing 97 BCGs, which is described in a series of five papers (Kong & Cheng (2002a); Kong et al. (2002b, 2003); Kong (2004); Shi et al. (2005)). These authors obtained their spectra using the 2.16m telescope of the Beijing Astronomical Observatory (BAO) in China, that included a spectroscope which achieved 10 Å resolution in the wavelength region 3580 Å to 7400 Å. The measured values of the equivalent width, reddening corrected flux and average continuum could be compared with the values from this above mentioned study (although the flux and wavelength units are different and the intrinsic flux values are given as relative to the flux of Hβ). For all three types of measurements, most of the values from Kong et al. (2002b), after unit conversion, are systematically higher than in this study but are still in the same order of magnitude, while some of the values agree.

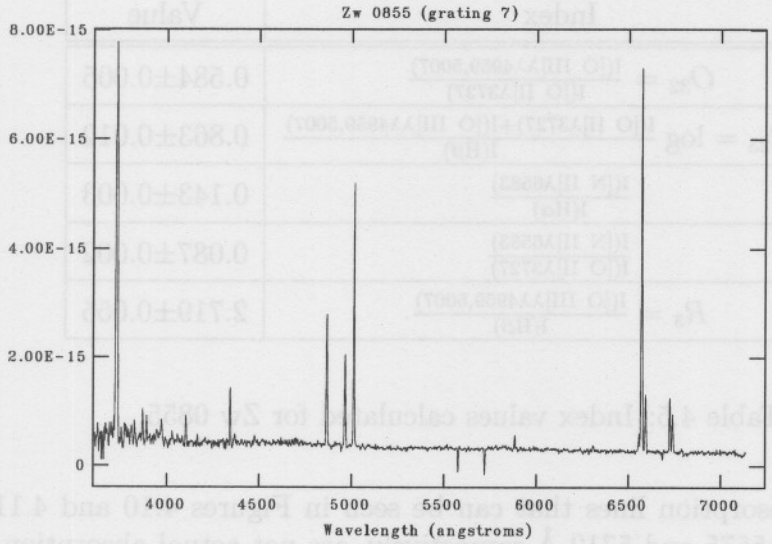

Figure 4.10: Zw 0855. The flux density is measured in erg $s^{-1}cm^{-2}Å^{-1}$.

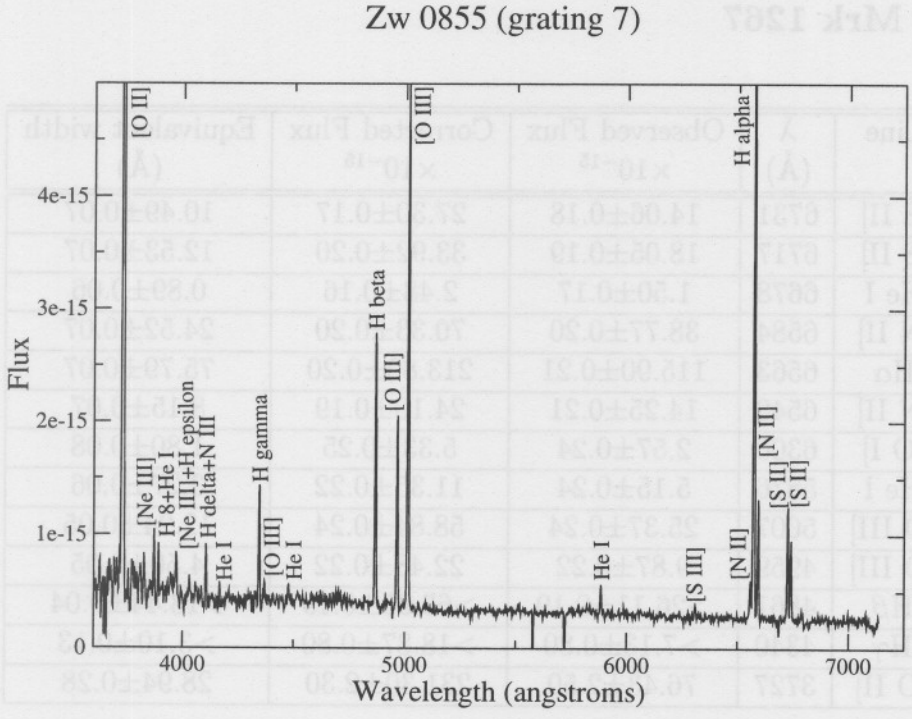

Figure 4.11: Zw 0855 with y-axis scaled to enhance emission lines.

Index	Value
$O_{32} = \frac{\text{I([O III]}\lambda\lambda\text{4959,5007)}}{\text{I([O II]}\lambda\text{3727)}}$	0.584±0.005
$\log R_{23} = \log \frac{\text{I([O II]}\lambda\text{3727)+I([O III]}\lambda\lambda\text{4959,5007)}}{\text{I(H}\beta\text{)}}$	0.863±0.012
$\frac{\text{I([N II]}\lambda\text{6583)}}{\text{I(H}\alpha\text{)}}$	0.143±0.003
$\frac{\text{I([N II]}\lambda\text{6583)}}{\text{I([O II]}\lambda\text{3727)}}$	0.087±0.002
$R_3 = \frac{\text{I([O III]}\lambda\lambda\text{4959,5007)}}{\text{I(H}\beta\text{)}}$	2.719±0.055

Table 4.5: Index values calculated for Zw 0855.

The two absorption lines that can be seen in Figures 4.10 and 4.11, at wavelengths of 5575 and 5712 Å respectively, are not actual absorption features. They only occur in one of the eight spectra that were combined and as a result also in the combined spectrum. Thus, they can be ignored.

4.4.2 Mrk 1267

No.	Line	λ (Å)	Observed Flux $\times 10^{-15}$	Corrected Flux $\times 10^{-15}$	Equivalent width (Å)
1	[S II]	6731	14.06±0.18	27.30±0.17	10.49±0.07
2	[S II]	6717	18.05±0.19	33.92±0.20	12.53±0.07
3	He I	6678	1.50±0.17	2.48±0.16	0.89±0.06
4	[N II]	6584	38.77±0.20	70.33±0.20	24.52±0.07
5	Hα	6563	115.90±0.21	213.80±0.20	75.79±0.07
6	[N II]	6548	14.25±0.21	24.10±0.19	8.15±0.07
7	[O I]	6300	2.57±0.24	5.33±0.25	1.80±0.08
8	He I	5876	5.15±0.24	11.35±0.22	3.27±0.06
9	[O III]	5007	25.37±0.24	58.84±0.24	12.24±0.05
10	[O III]	4959	9.87±0.22	22.48±0.22	4.50±0.05
11	Hβ	4861	>26.11±0.19	>63.95±0.19	>13.44±0.04
12	Hγ	4340	>7.13±0.80	>18.87±0.80	>3.10±0.13
13	[O II]	3727	76.43±2.50	231.30±2.30	28.94±0.28

Table 4.6: Emission-line measurements of Mrk 1267, (flux in erg $s^{-1}cm^{-2}$).

Mrk 1267 was also part of the BCG survey described in a series of five papers (Kong & Cheng (2002a); Kong et al. (2002b, 2003); Kong (2004); Shi et al. (2005)). The equivalent widths of the emission lines are in accordance with the values found by Kong et al. (2002b), with most of the values agreeing within the error bars and only small differences between those that do not. The equivalent widths of the absorption features also agree very well, with the value of MgI + MgH being the same. Overall, it was found that the measured values of the corrected fluxes were slightly less than the values from Kong et al. (2002b) but still of the same order. The measured continuum values were also slightly less but followed the same profile.

In this final spectrum of Mrk 1267, it can be seen that the Hβ and Hγ emission lines suffers from underlying absorption. Hδ and Hϵ are only absorption features. As a result of this underlying absorption in Hβ and Hγ, the measurements of these lines are extremely uncertain. These two lines were measured in such a way that their values in Table 4.6 can, in effect, be treated as lower limits. This also resulted in an overestimate of the interstellar extinction coefficient.

The difference between the observed flux measurement and the reddening corrected flux measurement, which result from the interstellar extinction, and the wavelength dependence of this difference can clearly be seen in Table 4.6. The reddening correction increased the corrected flux of Hα (λ6563 Å) by 84%, but increased the corrected flux of [O II] (λ3727 Å) by 202%. Mrk 1267 has the highest interstellar reddening coefficient in this small sample of five galaxies, as can be seen in Table 4.1. This might be a direct effect of the underlying stellar Balmer absorption, which caused an overestimated interstellar extinction coefficient. When the interstellar extinction coefficient is overestimated, the reddening corrected flux values becomes underestimated and this is the most likely explanation of the discrepancies between the measured continuum and reddening corrected flux values between this study and that of Kong et al. (2002b).

Absorption feature	Centred around wavelength (Å)	Equivalent width (Å)
Hδ	4094	3.53±0.05
Ca II, H + Hϵ	3959	3.57±0.03
MgI + MgH	5166	2.07±0.06

Table 4.7: Equivalent width of absorption features of Mrk 1267.

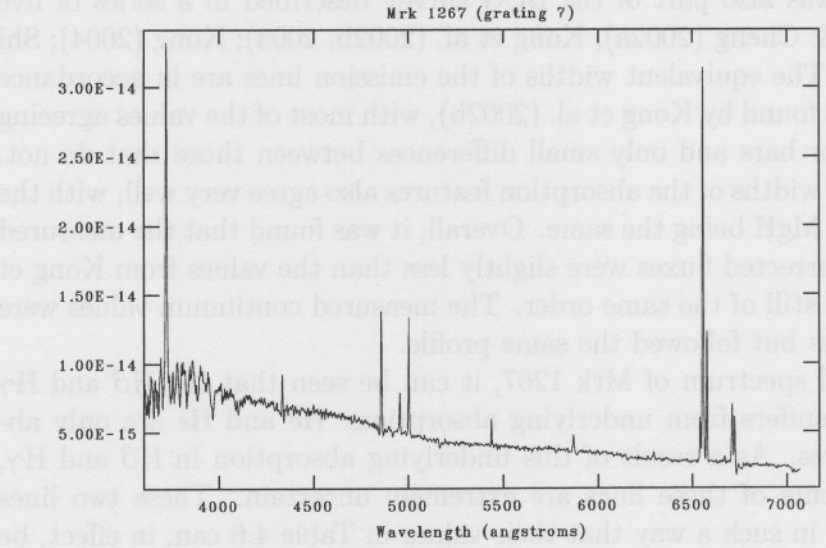

Figure 4.12: Mrk 1267. The flux density is measured in erg $s^{-1}cm^{-2}Å^{-1}$.

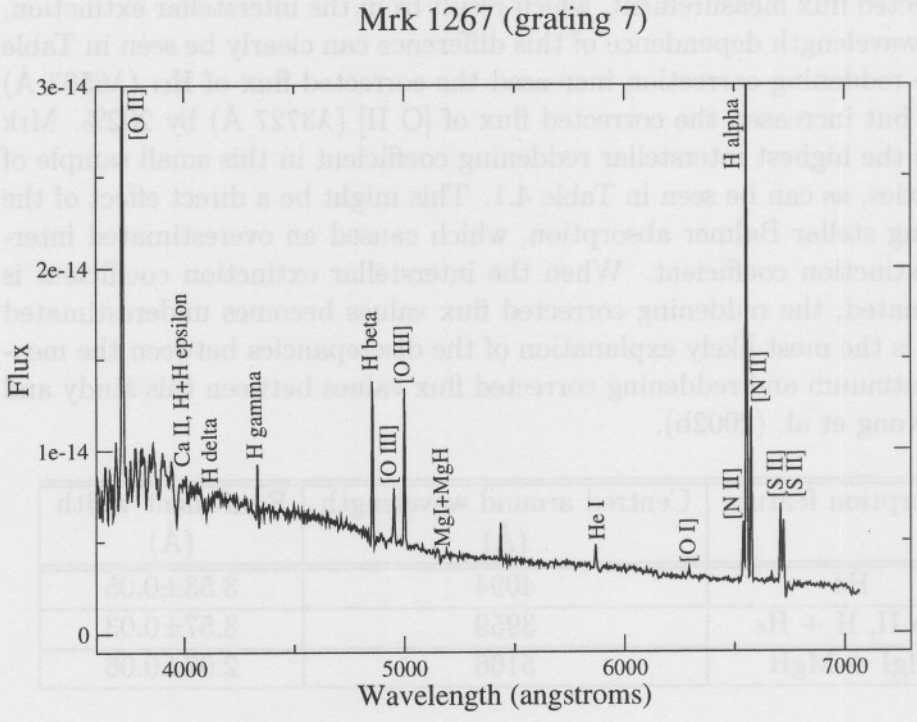

Figure 4.13: Mrk 1267 with y-axis scaled to enhance emission lines. Hδ, Ca II, H + Hϵ and MgI + MgH are absorption features. Note the underlying absorption at Hβ and Hγ.

The emission line at approximately 5432 Å in Figures 4.12 and 4.13, only occurs in one of the four spectra that were averaged together and as a result appears in the final spectrum. The line could be attributed to the sky spectrum that was not properly subtracted but this is unlikely as the sky line in that region of the spectra occurs at just over 5500 Å. Thus, it is most probably a cosmic ray event and was ignored in the measurements and analysis.

Index	Value
$O_{32} = \frac{\text{I([O III]}\lambda\lambda\text{4959,5007)}}{\text{I([O II]}\lambda\text{3727)}}$	0.352±0.002
$\log R_{23} = \log \frac{\text{I([O II]}\lambda\text{3727)+I([O III]}\lambda\lambda\text{4959,5007)}}{\text{I(H}\beta\text{)}}$	0.706±0.004
$\frac{\text{I([N II]}\lambda\text{6583)}}{\text{I(H}\alpha\text{)}}$	0.332±0.001
$\frac{\text{I([N II]}\lambda\text{6583)}}{\text{I([O II]}\lambda\text{3727)}}$	0.321±0.001
$R_3 = \frac{\text{I([O III]}\lambda\lambda\text{4959,5007)}}{\text{I(H}\beta\text{)}}$	1.272±0.011

Table 4.8: Index values calculated for Mrk 1267.

4.4.3 II Zw 33

No.	Line	λ (Å)	Observed Flux $\times 10^{-15}$	Corrected Flux $\times 10^{-15}$	Equivalent width (Å)
1	[S II]	6731	5.60±0.19	8.82±0.20	7.89±0.18
2	[S II]	6717	7.15±0.18	11.03±0.18	9.66±0.16
3	[N II]	6584	5.58±0.21	8.21±0.21	6.89±0.18
4	Hα	6563	40.94±0.19	57.52±0.20	48.75±0.17
5	[N II]	6548	1.57±0.16	2.41±0.17	2.02±0.15
6	[O I]	6300	1.10±0.19	2.04±0.18	1.62±0.14
7	He I	5876	2.32±0.20	3.58±0.19	2.49±0.13
8	[O III]	5007	30.18±0.20	47.52±0.19	24.46±0.10
9	[O III]	4959	10.48±0.19	16.60±0.19	8.47±0.10
10	Hβ	4861	>11.32±0.20	>18.37±0.18	>9.92±0.10
11	Hγ	4340	>4.40±1.05	>7.98±1.05	>3.98±0.50
12	[O II]	3727	49.75±2.10	98.13±1.90	35.02±0.66

Table 4.9: Emission-line measurements of II Zw 33 (flux in erg $s^{-1}cm^{-2}$).

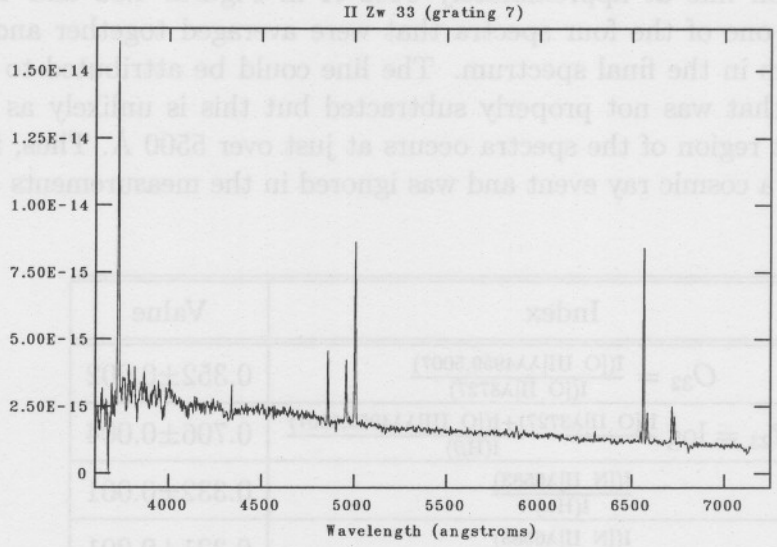

Figure 4.14: II Zw 33. The flux density is measured in erg $s^{-1}cm^{-2}Å^{-1}$.

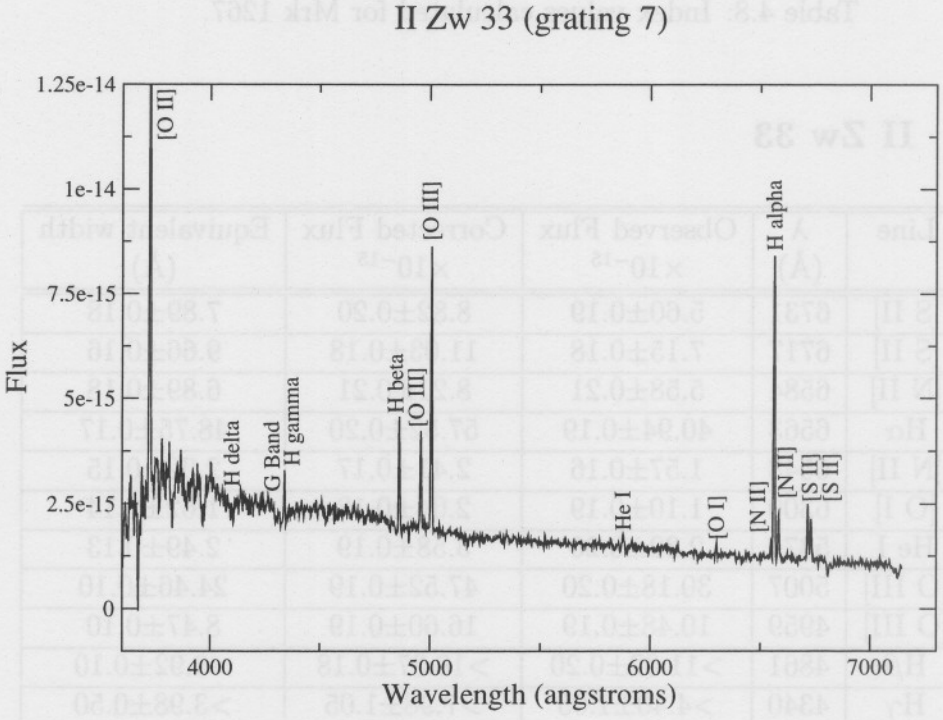

Figure 4.15: II Zw 33 with y-axis scaled to enhance emission lines. Hδ and G Band are absorption features.

As was the case with Zw 0855 and Mrk 1267, the measured values from II Zw 33 could also be compared with the values from the Kong et al. (2002b) study. The measured equivalent widths of the emission lines are in unison with the values from Kong et al. (2002b), with the exception of a few lines. The two measured values of the equivalent widths of the absorption features, are each about 2 Å smaller than the values from Kong et al. (2002b). The measured values of the corrected flux and the continuum are slightly smaller than their comparative values but still of the same order. The continuum profiles are also in agreement.

The Hβ and Hγ emission lines, again suffer from underlying absorption and Hδ is only an absorption feature (Figures 4.14 and 4.15). As a result of this underlying absorption in Hβ and Hγ, the measurements of these lines are once again uncertain. These two lines were also measured in such a way that their values in Table 4.9 can, in effect, be treated as lower limits. As was the case with Mrk 1267, this caused an overestimate in the interstellar extinction coefficient. In Table 4.1 it can be seen that II Zw 33 has the second highest (after Mrk 1267) interstellar extinction coefficient. This resulted once again in the continuum and reddening corrected flux values being slightly less than that of Kong et al. (2002b).

Absorption feature	Centred around wavelength (Å)	Equivalent width (Å)
Hδ	4096	5.32±0.08
G Band	4308	1.15±0.08

Table 4.10: Equivalent width of absorption features of II Zw 33.

Index	Value
$O_{32} = \frac{\text{I([O III]}\lambda\lambda\text{4959,5007)}}{\text{I([O II]}\lambda\text{3727)}}$	0.666±0.004
$\log R_{23} = \log \frac{\text{I([O II]}\lambda\text{3727)+I([O III]}\lambda\lambda\text{4959,5007)}}{\text{I(H}\beta\text{)}}$	0.928±0.010
$\frac{\text{I([N II]}\lambda\text{6583)}}{\text{I(H}\alpha\text{)}}$	0.138±0.004
$\frac{\text{I([N II]}\lambda\text{6583)}}{\text{I([O II]}\lambda\text{3727)}}$	0.082±0.002
$R_3 = \frac{\text{I([O III]}\lambda\lambda\text{4959,5007)}}{\text{I(H}\beta\text{)}}$	3.490±0.055

Table 4.11: Index values calculated for II Zw 33.

4.4.4 Tol 2

No.	Line	λ (Å)	Observed Flux $\times 10^{-15}$	Corrected Flux $\times 10^{-15}$	Equivalent width (Å)
1	[Ar III]	7136	5.39±0.21	6.63±0.21	10.12±0.33
2	[S II]	6731	11.09±0.19	16.10±0.21	13.21±0.27
3	[S II]	6717	7.78±0.21	14.77±0.20	18.26±0.24
4	He I	6678	2.26±0.33	3.14±0.33	3.76±0.39
5	[N II]	6584	5.81±0.19	8.21±0.19	10.12±0.23
6	Hα	6563	162.80±0.21	204.20±0.22	251.20±0.27
7	[N II]	6548	4.54±0.36	6.09±0.20	8.22±0.26
8	[S III]	6312	1.08±0.17	1.25±0.17	1.34±0.18
9	[O I]	6300	1.47±0.17	1.76±0.16	1.92±0.17
10	He I	5876	5.52±0.20	6.82±0.19	6.57±0.19
11	[O III]	5007	179.80±0.22	240.20±0.22	159.70±0.15
12	[O III]	4959	66.84±0.22	90.39±0.21	60.03±0.14
13	Hβ	4861	50.07±0.21	69.31±0.25	48.18±0.17
14	[O III]	4363	2.82±0.85	4.18±0.85	2.20±0.46
15	Hγ	4340	17.90±0.90	26.82±0.95	15.12±0.55
16	Hδ + N III	4102	7.82±1.80	13.18±2.10	6.15±0.96
17	[Ne III] + Hϵ	3969	8.95±2.00	15.51±2.10	6.28±0.86
18	[Ne III]	3869	14.43±1.60	25.40±2.20	9.26±0.79
19	He I	3820	3.66±1.40	10.81±1.70	4.17±0.66
20	[O II]	3727	99.74±2.20	160.30±2.50	55.23±0.86

Table 4.12: Emission-line measurements of Tol 2, (flux in erg $s^{-1}cm^{-2}$).

The BCG Tol 2 formed part of a spectrophotometric catalogue of 425 emission-line galaxies studied by Terlevich et al. (1991). They made use of larger telescopes located at the ESO (3.6m), Las Campanas (2.5m) and Cerro Tololo (4.0m) observatories. The measured values of the corrected flux and the equivalent widths of some of the emission lines of Tol 2 compared favourably with the values from the above mentioned study.

Terlevich et al. (1991) published the reddening corrected line fluxes as relative to the corrected flux of Hβ. The measured values (converted to corrected flux relative to Hβ) are in accordance with these published values, with most of the strong emission lines equating. For example, the measured value of [O II]/Hβ and Hγ/Hβ is 2.313 and 0.387, respectively, which compare very well to 2.333 and 0.343 from Terlevich et al. (1991).

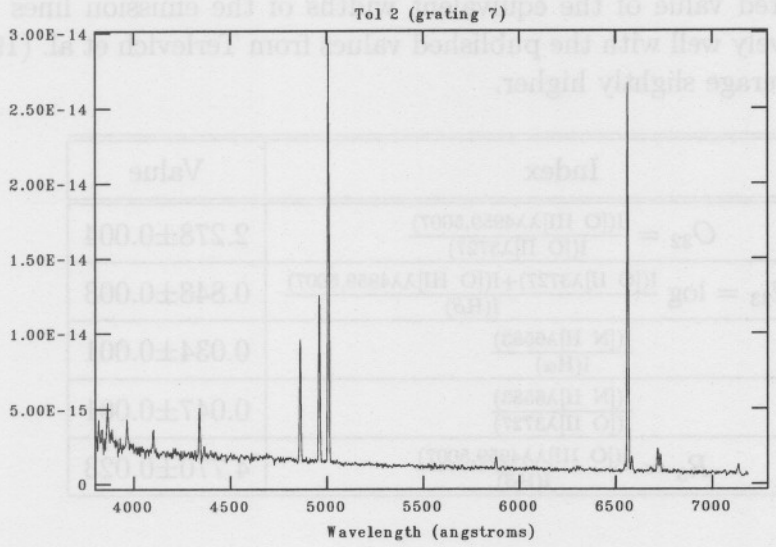

Figure 4.16: Tol 2. The flux density is measured in erg $s^{-1}cm^{-2}Å^{-1}$.

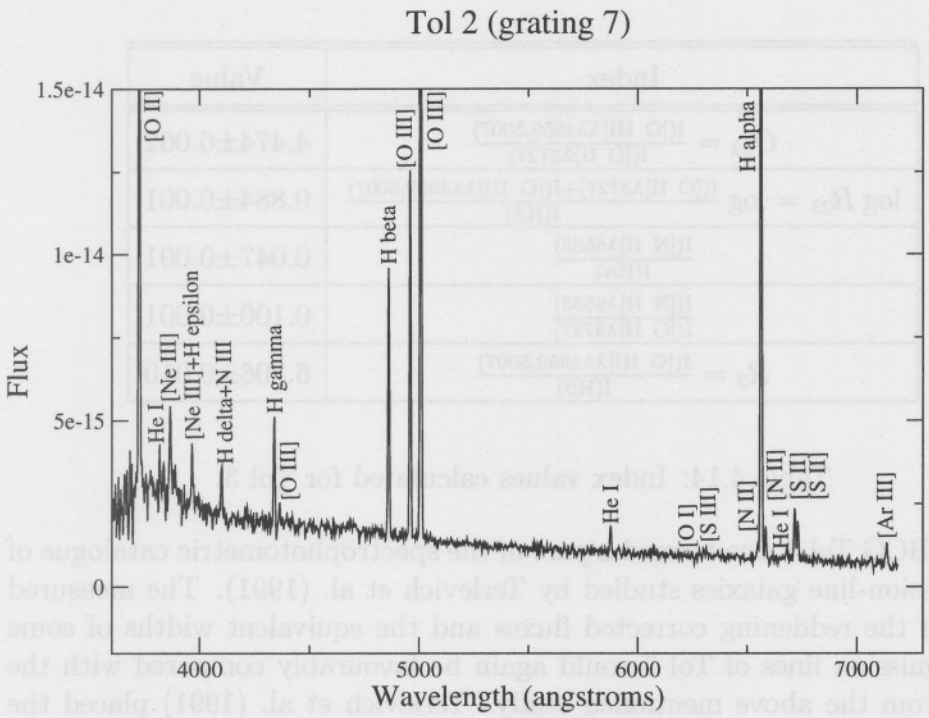

Figure 4.17: Tol 2 with y-axis scaled to enhance emission lines.

The measured value of the equivalent widths of the emission lines also compare relatively well with the published values from Terlevich et al. (1991) but were on average slightly higher.

Index	Value
$O_{32} = \frac{\text{I([O III]}\lambda\lambda\text{4959,5007)}}{\text{I([O II]}\lambda\text{3727)}}$	2.278±0.004
$\log R_{23} = \log \frac{\text{I([O II]}\lambda\text{3727)+I([O III]}\lambda\lambda\text{4959,5007)}}{\text{I(H}\beta\text{)}}$	0.848±0.003
$\frac{\text{I([N II]}\lambda\text{6583)}}{\text{I(H}\alpha\text{)}}$	0.034±0.001
$\frac{\text{I([N II]}\lambda\text{6583)}}{\text{I([O II]}\lambda\text{3727)}}$	0.047±0.001
$R_3 = \frac{\text{I([O III]}\lambda\lambda\text{4959,5007)}}{\text{I(H}\beta\text{)}}$	4.770±0.023

Table 4.13: Index values calculated for Tol 2.

4.4.5 Tol 3

Index	Value
$O_{32} = \frac{\text{I([O III]}\lambda\lambda\text{4959,5007)}}{\text{I([O II]}\lambda\text{3727)}}$	4.474±0.002
$\log R_{23} = \log \frac{\text{I([O II]}\lambda\text{3727)+I([O III]}\lambda\lambda\text{4959,5007)}}{\text{I(H}\beta\text{)}}$	0.884±0.001
$\frac{\text{I([N II]}\lambda\text{6583)}}{\text{I(H}\alpha\text{)}}$	0.047±0.001
$\frac{\text{I([N II]}\lambda\text{6583)}}{\text{I([O II]}\lambda\text{3727)}}$	0.100±0.001
$R_3 = \frac{\text{I([O III]}\lambda\lambda\text{4959,5007)}}{\text{I(H}\beta\text{)}}$	6.206±0.010

Table 4.14: Index values calculated for Tol 3.

The BCG Tol 3 also formed a part of the spectrophotometric catalogue of 425 emission-line galaxies studied by Terlevich et al. (1991). The measured values of the reddening corrected fluxes and the equivalent widths of some of the emission lines of Tol 3 could again be favourably compared with the values from the above mentioned study. Terlevich et al. (1991) placed the slit on two different regions of Tol 3, a NW region and a SE region, during their observations. However, some of the published values differ considerably between these two regions.

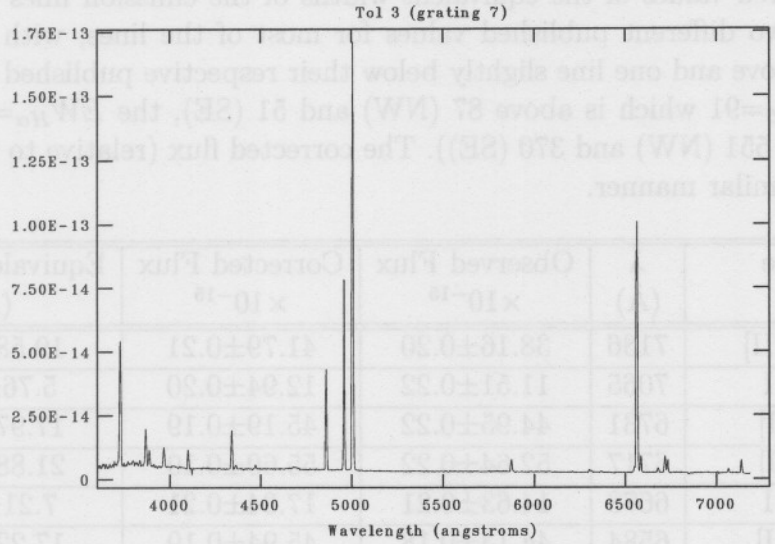

Figure 4.18: Tol 3. The flux density is measured in erg $s^{-1}cm^{-2}Å^{-1}$.

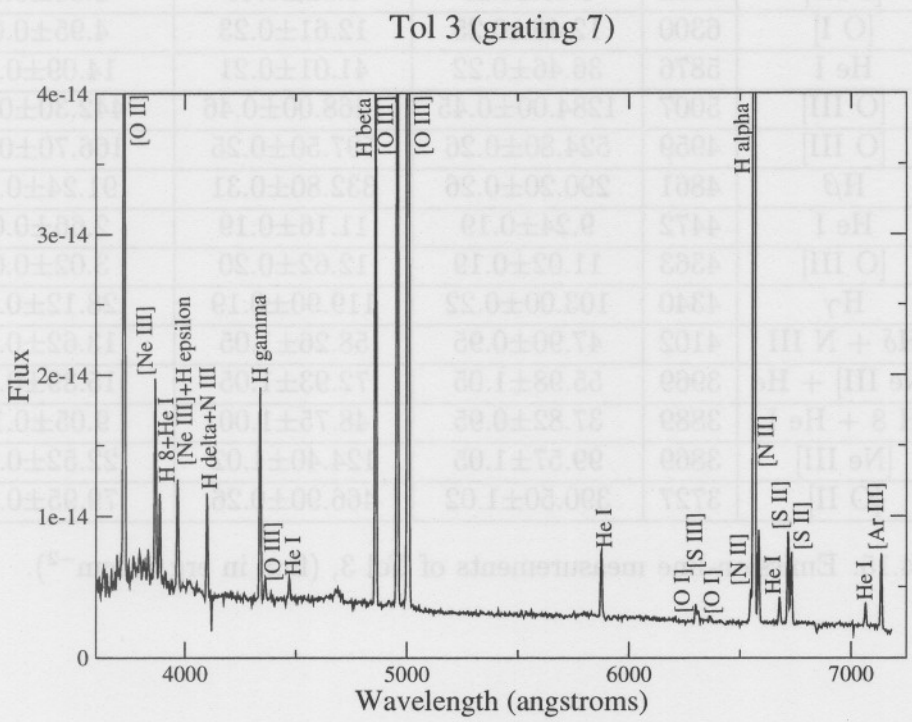

Figure 4.19: Tol 3 with y-axis scaled to enhance emission lines.

The measured values of the equivalent widths of the emission lines falls between the two different published values for most of the lines, with one line slightly above and one line slightly below their respective published values (the $EW_{H\beta}$=91 which is above 87 (NW) and 51 (SE), the $EW_{H\alpha}$=345 which is below 551 (NW) and 370 (SE)). The corrected flux (relative to Hβ) compared in similar manner.

No.	Line	λ (Å)	Observed Flux $\times 10^{-15}$	Corrected Flux $\times 10^{-15}$	Equivalent width (Å)
1	[Ar III]	7136	38.16±0.20	41.79±0.21	19.58±0.10
2	He I	7065	11.51±0.22	12.94±0.20	5.76±0.09
3	[S II]	6731	44.95±0.22	45.19±0.19	17.97±0.08
4	[S II]	6717	52.64±0.22	55.60±0.19	21.88±0.07
5	He I	6678	14.63±0.21	17.34±0.21	7.21±0.09
6	[N II]	6584	44.13±0.18	45.94±0.19	17.22±0.07
7	Hα	6563	866.70±0.21	961.80±0.22	344.80±0.08
8	[N II]	6548	15.45±0.17	22.03±0.21	19.06±0.08
9	[O I]	6364	3.06±0.18	3.24±0.17	1.26±0.07
10	[S III]	6312	8.19±0.29	8.82±0.46	3.30±0.17
11	[O I]	6300	12.46±0.25	12.61±0.23	4.95±0.09
12	He I	5876	36.46±0.22	41.01±0.21	14.09±0.07
13	[O III]	5007	1284.00±0.45	1468.00±0.46	442.30±0.08
14	[O III]	4959	524.80±0.26	597.50±0.25	166.70±0.07
15	Hβ	4861	290.20±0.26	332.80±0.31	91.24±0.09
16	He I	4472	9.24±0.19	11.16±0.19	2.66±0.05
17	[O III]	4363	11.02±0.19	12.62±0.20	3.02±0.05
18	Hγ	4340	103.00±0.22	119.90±0.19	28.12±0.05
19	Hδ + N III	4102	47.90±0.95	58.26±1.05	13.62±0.25
20	[Ne III] + Hϵ	3969	55.98±1.05	72.93±1.05	15.39±0.25
21	H 8 + He I	3889	37.82±0.95	48.75±1.00	9.05±0.19
22	[Ne III]	3869	99.57±1.05	124.40±1.02	22.52±0.04
23	[O II]	3727	390.50±1.02	466.90±0.26	79.95±0.04

Table 4.15: Emission-line measurements of Tol 3, (flux in erg $s^{-1}cm^{-2}$).

4.4.6 BCG Spectra: General Remarks

Firstly, note that without a full nebular analysis it can already be seen directly from the spectra that Zw 0855, Tol 2 and Tol 3 must be the most metal poor of the five galaxies. As mentioned before, the presence of the [O III]λ4363 line gives a preliminary indication of the metallicity of the source. Kobulnicky et al. (1999) states that [O III]λ4363 is generally detected only in galaxies with $12+\log(\frac{\mathrm{O}}{\mathrm{H}}) \leq 8.4$, which is roughly equivalent to $Z \leq 0.3Z_{\odot}$. It is therefore no coincidence that the spectra of the two galaxies in which absorption features were found, Mrk 1267 and II Zw 33, did not contain the [O III]λ4363 emission line. The stellar component of these galaxies not only cause the Balmer absorption but also contribute to the metallicity. A higher metallicity signals a lower temperature (as explained later under "Oxygen Abundances: General Remarks"). The condition where the [O III]λ4363 line becomes undetectable ($12+\log(\frac{\mathrm{O}}{\mathrm{H}}) > 8.4$) roughly corresponds to $T_e < 7\,500$ K, depending on surface brightness (Pagel 1997).

It is also interesting to note that the spectra of the galaxies in which the [O III]λ4363 line could be detected are the only spectra in which the [Ne III]λ3869 line was detected. As mentioned in chapter 2, neon is a product of the α-processes in nucleosynthesis occurring in the same massive stars ($M \geq 10M_{\odot}$) which produce oxygen (Izotov & Thuan 1999). As a result, the neon-to-oxygen ratio, Ne/O, is expected to be constant with oxygen abundance. In particular, the assumption that doubly-ionised neon is found where doubly-ionised oxygen is found in the cloud, is made in order to compute the neon abundance. The [Ne III]λ3869 line can, in conjunction with two other [Ne III] lines, also be used to determine the electron temperature from spectra.

The [Ne III] λ3869 and λ3969 lines were detected in Zw 0855, Tol 2 and Tol 3. In order to ionise Ne^{+} to Ne^{+2}, photon energies of at least 41.1 eV are required, thus a sufficient amount of photons with energy $h\nu > 41$ eV is needed (Ali et al. 1991). The lack of [Ne III] lines in Mrk 1267 and II Zw 33 indicates lower photon energies in general since the ionisation potential of Ne^{+2} is one of the highest of all the ions observed. This might indicate that the ionising stars in Mrk 1267 and II Zw 33 are cooler than those of Zw 0855, Tol 2 and Tol 3. The high metallicity in Mrk 1267 and II Zw 33 means that there must be a sufficient abundance of neon, but the lack of [Ne III] lines might be a result of the properties of the ionising stellar population.

Lastly note that in the spectra of Zw 0855, Mrk 1267 and II Zw 33, the [S II]λ6731 line is the last line that can be seen at the long wavelength end of the spectrum. This is because these galaxies have redshifts of $z = 0.0104$, 0.0206 and 0.0095, respectively and therefore, lines at the long wavelength end of the spectrum are lost. In the spectra of Tol 2 and Tol 3, [Ar III]λ7136

is the line with the longest wavelength that was detected, as these galaxies only have redshifts of $z = 0.0032$ and 0.0036, respectively.

4.5 Starbursts Or Not?

In chapter 2, the following relation was introduced from which an emission-line galaxy can be classified as an H II-like star formation galaxy (SFG):

$$\log\left(\frac{I([\text{N II}]\lambda 6583)}{I(\text{H}\alpha)}\right) < -0.25 \qquad (4.22)$$

otherwise, it is classified as an AGN (Kong et al. 2002b). This condition was tested for the five BCGs and they are indeed correctly classified as SFGs. The results are shown in Table 4.16.

BCG	$\log(\frac{\text{I([N II]}\lambda 6583)}{\text{I(H}\alpha)})$	Type of emission-line galaxy
Zw 0855	-0.845 ± 0.024	SFG
Mrk 1267	-0.478 ± 0.003	SFG
II Zw 33	-0.860 ± 0.025	SFG
Tol 2	-1.469 ± 0.001	SFG
Tol 3	-1.325 ± 0.002	SFG

Table 4.16: The values of the logarithm of the ratio $\frac{\text{I([N II]}\lambda 6583)}{\text{I(H}\alpha)}$.

4.6 Temperature and Density Determinations Using IRAF

The `nebular` package that was used in this section, is available in an external `IRAF` package called `STSDAS` (Space Telescope Science Data Analysis System, version 3.3.1, 2004). Several of the tasks are based upon the FIVEL program by De Robertis, Dufour and Hunt (1987).

The `temden` task was used to compute electron temperature or density from a diagnostic line ratio. The user specifies the quantity to be calculated (temperature or density), the reddening corrected diagnostic line ratio, the name and spectrum of the atom, and an assumed value for the quantity not being calculated (temperature or density). For the five BCGs, values for the I([S II]λ6716)/I([S II]λ6731) diagnostic line ratio were measured and used

to determine the density with a value of 10 000 K being assumed for the temperature. Values for the [O III] $I(\lambda\lambda 4959{,}5007)/I(\lambda 4363)$ diagnostic line ratio could be measured for three BCGs (the [O III]λ4363 line could not be detected in the case of two of the galaxies) and was used to determine the temperature with a value of 100 cm^{-3} being assumed for the density. The approximations, $T = 10\,000$ K and $N_e = 100$ cm^{-3} (the case B approximations), were also used previously in the Balmer decrement method when the reddening correction was made. The results are shown in Table 4.17.

These results are in general agreement with the physical conditions that are usually derived with this method. For example, Peña, Ruiz & Maza (1991) found an average N_e of 250 cm^{-3} for 42 Southern H II galaxies, with several values of $N_e < 100$ cm^{-3}; the highest value of N_e was 800 cm^{-3}. The temperatures are also in accordance with the values found in the above mentioned survey.

An assumption of a density of 1 000 cm^{-3} results in the following temperatures for the line ratios obtained in this study: Zw 0855 (19 290 K), Tol 2 (14 137 K) and Tol 3 (10 780 K). From this and Table 4.17, it can be seen that the calculations are not very sensitive to the density approximation, as stated in chapter 2. Likewise, the density calculations are not very sensitive to the temperature approximation.

Galaxy	Density (cm^{-3})	$\frac{I(\lambda 6716)}{I(\lambda 6731)}$
Zw 0855	27	1.4
Mrk 1267	240	1.2
II Zw 33	121	1.3
Tol 2	910	0.9
Tol 3	240	1.2

Galaxy	Temperature (K)	$\frac{I(\lambda\lambda 4959{,}5007)}{I(\lambda 4363)}$
Zw 0855	19 327	42.4
Tol 2	14 160	79.1
Tol 3	10 796	163.7

Table 4.17: Densities (assuming $T = 10\,000$ K) and temperatures (assuming $N_e = 100$ cm^{-3}) determined using the `temden` task in `IRAF`.

Another task, `zones`, computes the electron temperatures and densities of an ionised nebular gas in separate zones of low-, medium- and high-ionisation from a variety of diagnostic emission-line fluxes. This task makes use of an iterative technique to derive both the temperature and density (thus, no approximations are needed) within each of the three zones by making simultaneous use of temperature- and density-sensitive line ratios from different ions with similar ionisation potentials.

The only two diagnostic line ratios that could be measured in this study, i.e. that of [S II] and [O III], have different ionisation potentials. The [S II] ratio has an ionisation potential of 10.4 eV and can be used in the low-zone, while the [O III] ratio has an ionisation potential of 35.1 eV and can be used in the medium-zone. Thus, the `zones` task could not be applied to the data in this project, as a density and a temperature diagnostic line ratio are required for each of the three ionisation zones. This method of simultaneous solution for the temperature and density in the three different zones can only be used when a very exceptional signal-to-noise ratio is obtained during observations and in a relatively broad wavelength region.

Tables 4.18 and 4.19 give some of the temperature and density diagnostic line ratios tabulated in chapter 2, but with the ionisation zones for which it can be used indicated. These are the most common diagnostic line ratios used for nebular analysis and illustrate the number of lines and wavelength range necessary to use a sound method to determine the density and temperature simultaneously without assumptions, such as the method used in the `zones` task.

Spectrum	Line Ratio	Ionisation Potential (eV)	Zone
[S II]	I(6716+6731)/I(4068+4076)	10.4	Low
[O II]	I(3726+3729)/I(7320+7330)	13.6	Low
[N II]	I(6548+6583)/I(5755)	14.5	Low
[S III]	I(9069+9532)/I(6312)	23.4	Medium
[Ar III]	I(7136+7751)/I(5192)	27.6	Medium
[O III]	I(4959+5007)/I(4363)	35.1	Medium
[Ne III]	I(3869+3969)/I(3342)	41.1	Medium
[Ar V]	I(6435+7006)/I(4626)	59.8	High
[Ne V]	I(3426+3346)/I(2975)	97.0	High

Table 4.18: Electron temperature diagnostic line ratios with ionisation zones indicated.

Spectrum	Line Ratio	Ionisation Potential (eV)	Zone
[S II]	I(6716)/I(6731)	10.4	Low
[O II]	I(3726)/I(3729)	13.6	Low
[Cl III]	I(5517)/I(5537)	23.8	Medium
[Ar IV]	I(4711)/I(4740)	40.9	Medium
C III]	I(1907)/I(1909)	47.9	Medium
[Ne IV]	I(2423)/I(2425)	63.5	High

Table 4.19: Electron density diagnostic line ratios with ionisation zones indicated.

4.7 Oxygen Abundance Determinations

The three methods discussed in chapter 2: (1) the direct method; (2) the bright-line method by McGaugh (1991); and (3) the bright-line method by Pilyugin (2000), are applied to the data in this section. The accepted value used for the solar abundance is $12 + \log(\frac{\mathrm{O}}{\mathrm{H}}) = 8.87$ (Lee et al. 2003a).

Method 1: [O III]λ4363

This method was applied with the `ionic` task which also forms part of the external `nebular` package in `IRAF`. This task computes atomic energy-level populations, critical densities and line emissivities for a nebular gas, within the N-level atom approximation[3], given the electron temperature, T_e, and density, N_e. The user specifies the name and the spectrum of the atom, the assumed values for T_e and N_e, and (optionally) the wavelength and relative flux of a particular emission line or range of lines of interest. The task output lists the level populations, critical densities, line emissivities and optionally the ionic abundance relative to ionised hydrogen.

The emissivities are listed by atomic transition, as are the calculated wavelengths. If the wavelength of a particular line of interest and the observed line flux are provided, the task will compute the ionic abundance, relative to the ionised hydrogen as:

$$\frac{N(\mathrm{X}^l)}{N(\mathrm{H}^+)} = \frac{I(\lambda)}{I(\mathrm{H}\beta)} \times \frac{j(\mathrm{H}\beta)}{j(\lambda)} \tag{4.23}$$

[3]This task is based on the original FIVEL program by De Robertis et al. (1987) but has been extended beyond the five level approximation to provide diagnostics from a greater set of ions and emission lines. Thus, more than five levels are now accommodated for most of the ions (Shaw & Dufour 1995).

where $I(\lambda)/I(\mathrm{H}\beta)$ is the reddening corrected flux ratio and j the emissivity. In this case the calculated wavelength is really the sum of all lines lying within a specified range of the wavelength of interest. This range is specified with the `wv_toler` parameter. The Hβ emissivity is derived from a formula by Aller (1984):

$$4\pi j(\mathrm{H}\beta) = 1.387 \times 10^{-25} N_e N(\mathrm{H}^+) t_e^{-0.983} 10^{-0.0424/t_e} \tag{4.24}$$

in units of erg cm^{-3}s^{-1}, where $t_e = T_e/10^4$ K. The results of the abundance calculations are stored in the task parameter `result`.

As none of the five BCGs exhibited emission of He II λ4686 Å, which is indicative of the presence of O^{+3} (Lee & Skillman 2004), the oxygen abundances were computed using the formula

$$\frac{N(\mathrm{O})}{N(\mathrm{H})} = f\left[\frac{N(\mathrm{O}^+)}{N(\mathrm{H}^+)} + \frac{N(\mathrm{O}^{+2})}{N(\mathrm{H}^+)}\right] \tag{4.25}$$

where f is equal to 1 in this case and

$$\frac{N(\mathrm{O}^+)}{N(\mathrm{H}^+)} = \frac{I([\mathrm{O\ II}]\lambda 3727)}{I(\mathrm{H}\beta)} \frac{j(\mathrm{H}\beta; \mathrm{N_e}, \mathrm{T_e})}{j([\mathrm{O\ II}]\lambda 3727; \mathrm{N_e}, \mathrm{T_e})} \tag{4.26}$$

$$\frac{N(\mathrm{O}^{+2})}{N(\mathrm{H}^+)} = \frac{I([\mathrm{O\ III}]\lambda 5007)}{I(\mathrm{H}\beta)} \frac{j(\mathrm{H}\beta; \mathrm{N_e}, \mathrm{T_e})}{j([\mathrm{O\ III}]\lambda 5007; \mathrm{N_e}, \mathrm{T_e})} \tag{4.27}$$

The emissivity of [O II]λ3727 was computed by adding the emissivity of [O II]λ3726 and [O II]λ3729, since [O II]λ3727 is actually two lines, but very high spectral resolution is needed to resolve the two lines. The wavelength tolerance parameter `wv_toler` was set to include both lines in the theoretical calculations.

This direct method of metallicity determination is called the [O III]λ4363 method, because it depends on the temperature of the nebula, usually determined by the [O III] diagnostic line ratio, which in turn depends on the relatively weak [O III]λ4363 line. Thus, if the [O III]λ4363 line is available, this direct method can be used. As the temperature could only be determined for three of the five BCGs (for which the [O III]λ4363 line was available), it was assumed to be 10 000 K throughout the first set of calculations to determine the metallicity for all five galaxies, and the density was set to 100 cm^{-3} (the case B approximation).

Thereafter, the calculations were repeated for the three galaxies (Zw 0855, Tol 2 and Tol 3) using the previously determined temperature and density values. Although a density was assumed (100 cm^{-3}) to calculate the temperature and a temperature was assumed (10 000 K) to calculate the density,

the determined values for the temperature and density can be used together, since the equations to determine temperature (or density) are not very sensitive to the change in density (or temperature). To see this, consider once again the equation used to determine temperature from the [O III] diagnostic line ratio:

$$\frac{I(5007)+I(4959)}{I(4363)} = 7.6e^{32990/T}\left[1+4.49\times10^{-10}\frac{N_e}{T^{1/2}}\right]^{-1} \tag{4.28}$$

With densities in the order of 100 cm^{-3} and temperatures in the order of 10 000 K, the factor $\frac{N_e}{T^{1/2}}$ is in the order of 1. From the above equation, it can then be seen that the factor that includes the contribution of the density, N_e, is actually negligibly small. To see how the density equations are not very sensitive to temperature variations, consider Figure 2.3 (page 22). In the case of [O II], the small gap between the second ($^2D_{5/2}$) and third ($^2D_{3/2}$) levels of the ions used to determine density is equivalent to $\Delta E/kT = 3.11\times10^{-3}$ (assuming $T = 10\,000$ K), and thus has the effect of suppressing the temperature dependence, because $\exp(-\Delta E/kT) = 0.997$. In general, $\Delta E/kT \ll 1$ and thus, $\exp(-\Delta E/kT) \rightarrow 1$ will be true for density sensitive line ratios.

The results for $T_e = 10\,000$ K, $N_e = 100$ cm^{-3} are shown in Table 4.20, with the results for the determined temperatures and densities shown in Table 4.21. From the changes in the value of the oxygen abundances in these two tables it can be seen that the resulting oxygen abundance is very strongly dependent on temperature (while the calculations showed that it is not as sensitive to changes in density as it is in temperature). Hence, it can be concluded that the emissivity of Hβ as well as the emissivity of the oxygen ions vary significantly with temperature.

Galaxy	$12+\log(\frac{O}{H})$	[O/H]	Z
Zw 0855	8.40	−0.47	$Z_\odot/3.0$
Mrk 1267	8.23	−0.64	$Z_\odot/4.4$
II Zw 33	8.47	−0.40	$Z_\odot/2.5$
Tol 2	8.32	−0.55	$Z_\odot/3.5$
Tol 3	8.32	−0.55	$Z_\odot/3.5$

Table 4.20: The metallicity (oxygen abundance) determinations from method 1. The standard notation of solar metallicity indicated by $Z_\odot$ as well as [O/H]=$\log(\frac{O}{H})-\log(\frac{O}{H})_\odot$ were used. The values of $12+\log(\frac{O}{H})$ and [O/H] are both in the unit dex.

Note that the underlying stellar Balmer absorption caused the Hβ measurements of Mrk 1267 and II Zw 33 to be just the lower limits. Therefore, the oxygen abundances of these galaxies will almost certainly be a little bit lower than the values obtained and given in Table 4.20.

Galaxy	Temperature (K)	Density (cm^{-3})	$12+\log(\frac{O}{H})$	[O/H]	Z
Zw 0855	19 327	27	7.50	−1.37	$Z_{\odot}/23.4$
Tol 2	14 160	910	7.85	−1.02	$Z_{\odot}/10.5$
Tol 3	10 796	240	8.20	−0.67	$Z_{\odot}/4.7$

Table 4.21: Metallicity determinations with the determined temperatures and densities.

Method 2: The Bright-Line Method

This empirical method could be applied to the reddening corrected line fluxes from the spectra of all five BCGs without the aid of any software packages. Because of the degeneracy of the oxygen abundance calibration in this empirical method as well as in method 3, the value of the ratio

$$\frac{I([\text{N II}]\lambda 6583)}{I([\text{O II}]\lambda 3727)} \tag{4.29}$$

should be utilised to discriminate between the upper and lower oxygen abundance values. If this ratio is larger than 0.1 then the galaxy has a high oxygen abundance and the upper value should be used. Similarly if the ratio is lower than 0.1 then the lower value should be used (Lee et al. 2003a).

For the galaxies Zw 0855, II Zw 33 and Tol 2, the following equation for the lower oxygen abundance was used in accordance with the values of the [N II]/[O II] ratio:

$$12+\log(\frac{\text{O}}{\text{H}})_{lower} = 12-4.93+4.25x-3.35\sin(x)-0.26y-0.12\sin(y) \tag{4.30}$$

For Mrk 1267 the equation used for the upper oxygen abundance was:

$$12+\log(\frac{\text{O}}{\text{H}})_{upper} = 12-2.65-0.91x+0.12y\sin(x) \tag{4.31}$$

In both the upper and lower equations, the trigonometric function is in radians and $x \equiv \log R_{23}$ and $y \equiv \log O_{32}$. However, for Tol 3 the value of the [N II]/[O II] ratio is 0.100±0.001, and as a result no choice could be made between the degenerate upper and lower values and both were calculated. The results are given in Table 4.22.

Galaxy	[N II]/[O II]	upper/lower	$12+\log(\frac{O}{H})$	[O/H]	Z
Zw 0855	0.087±0.002	lower	8.28±0.04	−0.59	$Z_\odot/3.9$
Mrk 1267	0.321±0.001	upper	8.67±0.02	−0.20	$Z_\odot/1.6$
II Zw 33	0.082±0.002	lower	8.40±0.03	−0.47	$Z_\odot/3.0$
Tol 2	0.047±0.001	lower	8.03±0.01	−0.84	$Z_\odot/7.0$
Tol 3 u	0.100±0.001	upper	8.61±0.01	−0.26	$Z_\odot/1.8$
Tol 3 l	0.100±0.001	lower	8.00±0.01	−0.88	$Z_\odot/7.5$

Table 4.22: The metallicity (oxygen abundance) determinations from method 2. The standard notation of solar metallicity indicated by $Z_\odot$ as well as $[O/H]=\log(\frac{O}{H})-\log(\frac{O}{H})_\odot$ were used. The values of $12+\log(\frac{O}{H})$ and [O/H] are both in the unit dex.

Method 3: The Empirical Bright-Line Method

The procedure for the determination of the oxygen abundances using this method followed that of the previous method, with the only difference being the empirical equations used:

$$12+\log(\frac{O}{H})_{lower} = 6.35+3.19\log R_{23}-1.74\log R_3 \tag{4.32}$$

$$12+\log(\frac{O}{H})_{upper} = \frac{R_{23}+54.2+59.45P+7.31P^2}{6.07+6.71P+0.371P^2+0.243R_{23}} \tag{4.33}$$

The excitation parameter P is the contribution of the radiation in [O III]$\lambda\lambda$4959, 5007 lines to the total oxygen radiation. The results achieved are shown in Table 4.23.

Galaxy	upper/lower	$12+\log(\frac{O}{H})$	[O/H]	Z
Zw 0855	lower	8.35±0.08	−0.52	$Z_\odot/3.3$
Mrk 1267	upper	8.29±0.04	−0.58	$Z_\odot/3.8$
II Zw 33	lower	8.37±0.03	−0.50	$Z_\odot/3.2$
Tol 2	lower	7.87±0.01	−1.00	$Z_\odot/9.9$
Tol 3 u	upper	8.44±0.03	−0.43	$Z_\odot/2.7$
Tol 3 l	lower	7.79±0.02	−1.08	$Z_\odot/12.0$

Table 4.23: The metallicity (oxygen abundance) determinations from method 3. The standard notation of solar metallicity indicated by $Z_\odot$ as well as $[O/H]=\log(\frac{O}{H})-\log(\frac{O}{H})_\odot$ were used. The values of $12+\log(\frac{O}{H})$ and [O/H] are both in the unit dex.

Oxygen Abundances: General Remarks

Shi et al. (2005) published the fifth paper in a series studying BCGs (first to fourth papers published by Kong & Cheng (2002a); Kong et al. (2002b, 2003); Kong (2004)), in which they derive the metallicities of a sample of BCGs. This sample of BCGs includes the galaxies Zw 0855, Mrk 1267 and II Zw 33. Shi et al. (2005) used five different methods to obtain the oxygen abundances of the galaxies, of which one of the methods makes use of the electron temperature, T_e, and four methods make use of strong line empirical abundance indicators. Although their methods are different from that used in this study, the results of this study fall in the range of their published results ($7.15 > 12 + \log(\frac{O}{H}) < 9.0$) for all the BCGs in their sample. Two of the methods used in the above mentioned paper agree to a certain extent with methods 2 and 3 in this study, with only minor differences. Table 4.24 shows the results of Shi et al. (2005). Method 1 is the direct method which makes use of T_e, 2 and 3 are similar to 2 and 3 in this study, while methods 4 and 5 make use of the [N II]λ6583 line. Shi et al. (2005) also states that their values for the oxygen abundances derived from the method that makes use of the temperature, T_e, are on average systematically lower than those derived from the strong line empirical abundance indicators. This can be seen in the results of this study by comparing Table 4.21 to Tables 4.22 and 4.23.

Galaxy	Method 1	Method 2	Method 3	Method 4	Method 5
Zw 0855	8.43	8.65	8.41	8.49	8.35
Mrk 1267	8.60	8.87	8.60	8.85	8.64
II Zw 33	7.99	8.34	8.01	8.40	8.29

Table 4.24: Oxygen abundances by Shi et al. (2005).

True to the nature of BCGs, all three methods used in this study deliver metallicities below the solar value. However, it was found that there are rather large discrepancies between the results of the three methods used in this study. For example, the value of $Z = Z_{\odot}/23.4$ for Zw 0855 (calculated with the direct method) is not at all in accordance with the values of $Z = Z_{\odot}/3.9$ and $Z = Z_{\odot}/3.3$ (calculated with the empirical methods). This is also very clear from the results of Shi et al. (2005). Not only are the results of the empirical methods systematically higher than those obtained by the direct method, but the precision of the empirical methods is no better than $0.2 - 0.3$ dex (Izotov & Thuan 1999). It is clear that extra attempts should be made in order to derive precise results for the metallicity of metal poor

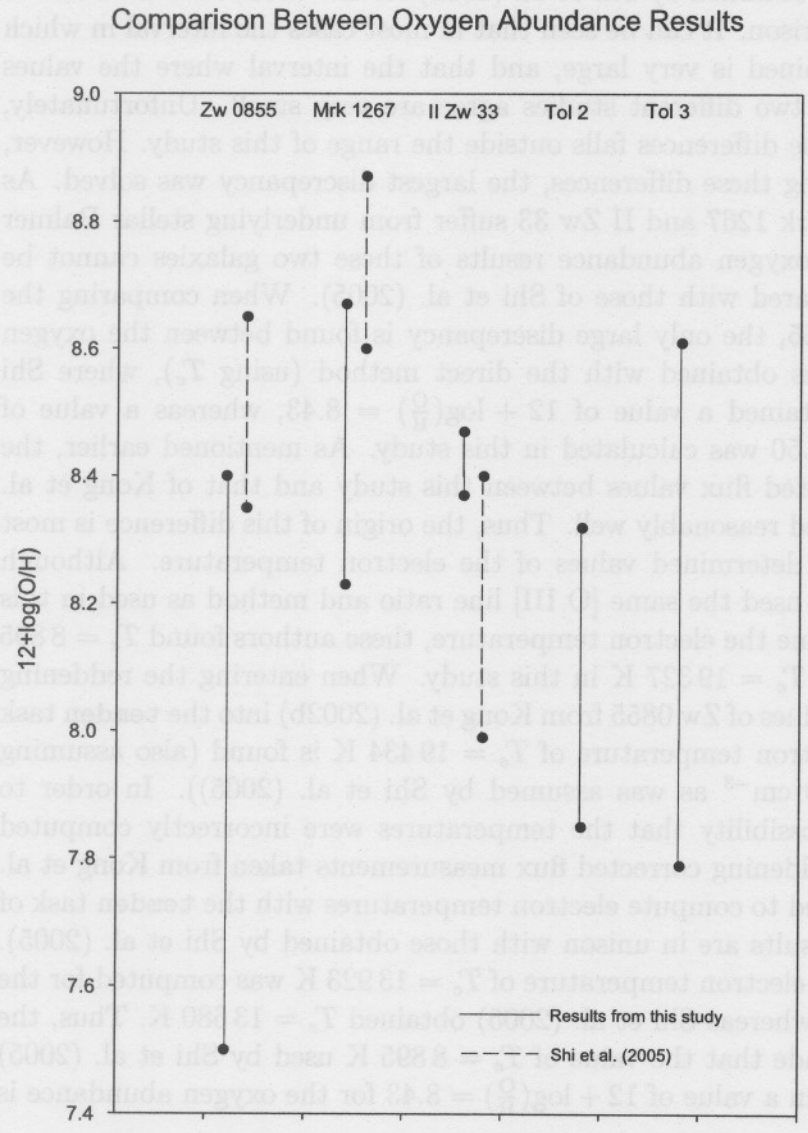

Figure 4.20: Comparison between oxygen abundance results.

galaxies, and that empirical methods should be carefully investigated before applying them.

Figure 4.20 shows the highest and the lowest oxygen abundance value obtained for each of the five BCGs in this study. It also shows the highest and the lowest value obtained by Shi et al. (2005) for Zw 0855, Mrk 1267 and II Zw 33, in comparison. It can be seen that in most cases the interval in which values were obtained is very large, and that the interval where the values obtained by the two different studies agree are very small. Unfortunately, the origin of these differences falls outside the range of this study. However, upon investigating these differences, the largest discrepancy was solved. As the spectra of Mrk 1267 and II Zw 33 suffer from underlying stellar Balmer absorption, the oxygen abundance results of these two galaxies cannot be accurately compared with those of Shi et al. (2005). When comparing the values of Zw 0855, the only large discrepancy is found between the oxygen abundance values obtained with the direct method (using T_e), where Shi et al. (2005) obtained a value of $12 + \log(\frac{\mathrm{O}}{\mathrm{H}}) = 8.43$, whereas a value of $12 + \log(\frac{\mathrm{O}}{\mathrm{H}}) = 7.50$ was calculated in this study. As mentioned earlier, the reddening corrected flux values between this study and that of Kong et al. (2002b) compared reasonably well. Thus, the origin of this difference is most probably in the determined values of the electron temperature. Although Shi et al. (2005) used the same [O III] line ratio and method as used in this study to determine the electron temperature, these authors found $T_e = 8\,895$ K, compared to $T_e = 19\,327$ K in this study. When entering the reddening corrected flux values of Zw 0855 from Kong et al. (2002b) into the `temden` task of `IRAF`, an electron temperature of $T_e = 19\,434$ K is found (also assuming a density of 100 cm^{-3} as was assumed by Shi et al. (2005)). In order to eliminate the possibility that the temperatures were incorrectly computed in this study, reddening corrected flux measurements taken from Kong et al. (2002b) were used to compute electron temperatures with the `temden` task of `IRAF` and the results are in unison with those obtained by Shi et al. (2005). For example, an electron temperature of $T_e = 13\,923$ K was computed for the BCG II Zw 40, whereas Shi et al. (2005) obtained $T_e = 13\,680$ K. Thus, the conclusion is made that the value of $T_e = 8\,895$ K used by Shi et al. (2005) in order to obtain a value of $12 + \log(\frac{\mathrm{O}}{\mathrm{H}}) = 8.43$ for the oxygen abundance is in doubt.

The underlying Balmer stellar absorption in Mrk 1267 and II Zw 33 resulted in overestimates of the oxygen abundances in Tables 4.20, 4.22 and 4.23. Since the severity of these overestimates are unknown, it is not possible to confirm the prediction (by the absence of the [O III]λ4363 line) that these two galaxies are the least metal poor of the five BCGs.

Oxygen regulates physical conditions as the primary coolant within H II

regions. Cooling is accomplished primarily through the optical emission lines of oxygen. Thus, the electron temperature is also very useful as an oxygen abundance indicator as higher chemical abundances increase nebular cooling, leading to lower temperatures (Kewley & Dopita 2002). This relationship between electron temperature and oxygen abundance is clearly illustrated in Table 4.21, where the oxygen abundances were determined with the direct method using the determined temperatures and densities. This relationship between oxygen abundance and temperature is also the reason why the [O III]λ4363 line becomes undetectable at metallicities higher than $0.3Z_{\odot}$. In high abundance H II regions, the temperature (T_e) becomes so low that the [O III]λ4363 line becomes undetectable (equation 4.28). This situation is better for planetary nebulae because they can have high surface brightness. The condition where the [O III]λ4363 line becomes undetectable ($12+\log(\frac{\mathrm{O}}{\mathrm{H}}) > 8.4$) roughly corresponds to $T_e < 7\,500$ K, depending on surface brightness (Pagel 1997).

4.8 Other Abundances

Nitrogen

The nitrogen and neon abundances were computed in the same manner as the oxygen abundance (method 1) by using the `ionic` task in `IRAF`. The nitrogen abundance was calculated according to the formula:

$$\frac{\mathrm{N}}{\mathrm{O}} = \frac{I([\mathrm{N\ II}]\lambda 6583)}{I([\mathrm{O\ II}]\lambda 3727)} \frac{j([\mathrm{O\ II}]\lambda 3727; \mathrm{N_e}, \mathrm{T_e})}{j([\mathrm{N\ II}]\lambda 6583; \mathrm{N_e}, \mathrm{T_e})} \tag{4.34}$$

The nitrogen abundance results for the case B approximation (T_e =10 000 K and $N_e = 100\,\mathrm{cm}^{-3}$) are given in Table 4.25 and the results for the determined temperatures and densities are given in Table 4.26.

Galaxy	$\log(\frac{\mathrm{N}}{\mathrm{O}})$
Zw 0855	−1.35
Mrk 1267	−0.80
II Zw 33	−1.36
Tol 2	−1.57
Tol 3	−1.29

Table 4.25: The nitrogen abundances for the case B approximation.

Galaxy	Temperature (K)	Density (cm^{-3})	$\log(\frac{N}{O})$
Zw 0855	19 327	27	−0.99
Tol 2	14 160	910	−1.42
Tol 3	10 796	240	−1.25

Table 4.26: The nitrogen abundances for the determined temperatures and densities.

Once again, it can be seen that the abundances depend very strongly on temperature and density (via the emissivities).

Shi et al. (2005) used a different method of calculating the nitrogen abundance but obtained similar results for Zw 0855 ($\log(\frac{N}{O}) = -1.22$), Mrk 1267 ($\log(\frac{N}{O}) = -0.69$) and II Zw 33 ($\log(\frac{N}{O}) = -1.40$). Lee & Skillman (2004) studied 16 H II regions in the starburst galaxy NGC 1705 and found an average of $\log(\frac{N}{O}) = -1.63 \pm 0.07$. Garnett (1990) also studied extragalactic H II regions and found an average value of $\log(\frac{N}{O}) = -1.46^{+0.10}_{-0.13}$.

Neon

The [Ne III]λ3869 line could be measured in three of the five BCG spectra (the same three galaxies for which the [O III]λ4363 line could be measured). Thus, the neon abundance was determined for these three galaxies, using their determined temperatures and densities, according to the formula:

$$\frac{Ne}{O} = \frac{I([\text{Ne III}]\lambda 3869)}{I([\text{O III}]\lambda 5007)} \frac{j([\text{O III}]\lambda 5007; N_e, T_e)}{j([\text{Ne III}]\lambda 3869; N_e, T_e)} \tag{4.35}$$

with the results shown in Table 4.27.

Galaxy	$\log(\frac{Ne}{O})$
Zw 0855	−0.66
Tol 2	−0.56
Tol 3	−0.60

Table 4.27: The neon abundances.

Lee & Skillman (2004) studied 16 H II regions in the starburst galaxy NGC 1705 and found an average of $\log(\frac{Ne}{O}) = -0.426 \pm 0.033$.

The `nebular` package also hosts a task called `abund`, that computes abundances for several ions simultaneously. Given the electron temperature and

density, Hβ and ionic emission-line fluxes, the task computes the abundances in the low-, medium- and high-ionisation zones. This task is particularly useful if there are enough diagnostic emission lines present in a spectrum so that the temperatures and densities can be computed with the `zones` task, as the output from the `zones` task can be directly used as partial input for the `abund` task.

4.9 Other Nebular Analysis Software

SNAP

The Spreadsheet Nebular Analysis Package (`SNAP`) was developed by astronomers at York University in Toronto, Canada, who used Microsoft Excel and the built-in programming language (Visual Basic for Applications) to create a user-friendly nebular analysis tool.

`SNAP` can be used to interpret measurements of spectral line fluxes in one or two dimensions. It can be used to estimate the amount of extinction by dust along any line of sight, and then to correct the flux for the extinction. It can be used to calculate temperatures or densities from observed ratios of the reddening corrected line fluxes. Then, given temperatures and densities, it can calculate abundances of individual ions, as well as total elemental abundances. `SNAP` also provides a number of accessories to aid the user in the development of nebular diagnostics. Atomic data used in the calculations can be inspected and additional data can be added. Grotrian diagrams can also be displayed for collisionally excited ions.

This program was acquired through private communication with one of the developers, Marshall McCall, and applied to the data of the five BCGs in order to compare the results with those of `IRAF's nebular` package. `SNAP` can compute the electron temperature by using either the I([O III]λ4363)/I([O III]λ5007) or the I([O III]λ4363)/I([O III]λ4959) ratio, provided an assumption for the density is made, whereas `IRAF` uses the whole [O III] $I(\lambda\lambda(4959{,}5007))/I(\lambda 4363)$ ratio. As in `IRAF`, the density can be computed using the I([S II]λ6716)/I([S II]λ6731) ratio, once again providing an electron temperature. These results are given in Table 4.28 and compare very well with those obtained with `IRAF` (Table 4.17).

Once again, the availability of the [O III]λ4363 line constrained the temperature calculations to three of the five galaxies and the density of Zw 0855 was too low to be computed. The minor discrepancies between Tables 4.17 and 4.28 may be due to the iterative methods used to solve the equations or to differences in the atomic data used.

Galaxy	Density (cm^{-3})
Zw 0855	<100
Mrk 1267	186
II Zw 33	176
Tol 2	848
Tol 3	201

Galaxy	Temperature (K) $\frac{I(\lambda4363)}{I(\lambda5007)}$	Temperature (K) $\frac{I(\lambda4363)}{I(\lambda4959)}$
Zw 0855	19 343	19 141
Tol 2	14 266	13 776
Tol 3	10 935	10 412

Table 4.28: Densities (assuming $T = 10\,000$ K) and temperatures (assuming $N_e = 100$ cm^{-3}) determined using SNAP.

The oxygen abundance was computed by using the same procedure and emission lines as in IRAF, with the results for the three galaxies for which temperatures could be determined shown in Table 4.29. The temperature results from IRAF were used in this calculation, to preserve consistency in order to compare the oxygen abundance results with those previously obtained.

Galaxy	Temperature (K)	Density (cm^{-3})	$12 + \log(\frac{O}{H})$	Z
Zw 0855	19 327	27	7.77	$Z_\odot/12.6$
Tol 2	14 160	910	7.96	$Z_\odot/8.1$
Tol 3	10 796	240	8.32	$Z_\odot/3.5$

Table 4.29: SNAP metallicity determinations using the determined temperatures and densities.

These results are systematically slightly higher than those obtained with IRAF (Table 4.21). This can only be due to differences in the equations and atomic data used to compute the emissivities in the two software packages.

Overall, a satisfactory agreement in the temperature, density and oxygen abundance calculations between IRAF's nebular package and SNAP was found.

Cloudy

`Cloudy` is a spectral simulation code developed by Gary Ferland and is available on the internet.

The code computes the non-equilibrium ionisation, thermal and chemical state of a cloud that may (or may not) be exposed to an external radiation field. Given the basic assumption that atomic processes have had time to reach a steady state, the code will then determine the ionisation, temperature and chemical state of a cloud and predict its spectrum. This is done by simultaneously solving the equations of statistical equilibrium and equations that balance ionisation-neutralisation and heating-cooling processes, respectively.

`Cloudy` is designed to simulate emission-line regions ranging from the intergalactic medium to the broad line regions of quasars. It can be used to predict either the structure or the observed spectrum from such regions.

Other

Kewley & Dopita (2002) used a combination of stellar population synthesis and photoionisation models to develope a set of ionisation parameter and abundance diagnostics based only on the use of the strong optical emission lines. They made use of various models to develop an optimal scheme for abundance determination based on the range of possible combinations of bright optical or infrared emission lines which are likely to be available to the observer.

4.10 Summary

The corrections that have been applied to the spectra of the five BCGs, why it was necessary and how it corrects the information that can be learned from the spectra, are discussed in this chapter. The procedure for centroid, flux and equivalent width measurements, together with the errors involved are also discussed. The error bars on all of the above mentioned measurements were only determined by the signal-to-noise ratio of the spectra, which were on average very good. The errors therefore, give no indication of the measurement error that could have resulted from the interactive manner in which the measurements were made. Two different users of the same measurement task in `IRAF`, will almost certainly define the start and end of the emission line with respect to the continuum at different points and thus get different answers. These measurements should be applied to the nebular analysis methods and interpreted with this factor kept in mind. The emission lines were also successfully identified with the aid of a spectral line atlas.

There is no doubt about the presence of dust in H II galaxies, nor that it modifies the spectra of these galaxies. However, to correct accurately for its extinction is difficult. Since very little is known about the properties of dust in these galaxies, the standard assumption is that the properties of the dust in emission-line galaxies are identical with the optical properties of dust in our Galaxy near the Sun. The distribution of dust in these galaxies may well be irregular, thus the assignment of a single value for the extinction, as was done in this project, is only a first approximation. Using this single value, the extinction due to the gas in our Galaxy was corrected, after which the correction for the Doppler shift was successfully executed. The Doppler shift for each galaxy was also determined from the spectra and these values are in general agreement with those from the literature, with the minor discrepancies fully ascribable to measurement errors and instrumental limitations.

The spectra of all seven objects have been presented in this chapter. The presence of the background sky in the spectra of the galactic H II regions, impeded the application of the nebular analysis methods to these spectra but a nebular analysis was done on each of the five BCGs. All measurements of the BCGs are tabulated and despite the fact that there are unknown errors, resulting from the interactive manner in which the measurements were made, the reddening corrected flux as well as the continuum measurements are in satisfactory agreement with the respective published values. As a preliminary test of the resulting emission line fluxes from the corrected spectra, an empirical relation was evaluated to confirm that the five galaxies are indeed star formation galaxies.

Notwithstanding the unknown measurement errors, resulting from interactive measurements, and the necessary temperature and density assumptions, the calculated temperatures and densities are in the range usually encountered for these galaxies.

The metallicities of the BCGs were determined using three different methods and although these metallicity values are not precise they are in the range expected for BCGs. Not only in this study but also in other studies significant differences were noted between the results of different methods used to obtain oxygen abundances. In this study as well as in the study of Shi et al. (2005), the empirical calibrations yield oxygen abundances that are systematically higher than those obtained with the temperature-based methods.

The values computed for the nitrogen and neon abundances compared well with those computed for metal poor extragalactic H II regions in other studies (Shi et al. 2005; Garnett 1990; Lee & Skillman 2004). As the methods of the determination of these abundances make use of lines in the blue region of the spectrum, [O II]λ3727 and [Ne III]λ3869, this was interpreted as an indication that the reddening correct procedure did not overestimate the

reddening correction factor by a large amount, in spite of the underlying stellar Balmer absorption. The fact that the nitrogen lines blended with Hα also complicated the measurements and affected the resulting abundance determinations.

An investigation into other software packages, particularly `SNAP`, was carried out. Overall it was found that very useful nebular analysis tools are in existence and that there is satisfactory agreement between the calculations executed with `SNAP` and those executed with the `nebular` package in `IRAF`.

Chapter 5

Conclusions and Recommendations

As discussed in the introductory chapter, to acquire command of the basic methods and techniques of astronomical optical spectroscopy, constituted the chief purpose of this study. It is of the utmost importance to be conversant with the basic methods of astronomical spectroscopy to ensure the successful and optimal use of SALT (or any other large telescope). Priority was given to obtaining, reducing and analysing CCD spectra in the most optimal manner. It is imperative that these basic methods, such as flux and wavelength calibration, reddening correction and nebular analysis are fully mastered before attempting to solve real scientific questions. This includes having a sound knowledge of not only the application of these methods but also of the limitations.

In spite of various limitations and constraints experienced with the observation of the seven sources chosen for this study as well as with the data reduction procedures, the results obtained (reddening correction coefficient, temperature, density, metallicity as well as other elemental abundances) compared very well with those obtained from previous studies, and where the results could not be compared it proved at least very feasible. The results and comparisons with the expected results are presented in detail in chapter 4, which also contains remarks about the spectra.

Fortunately, most of the limitations will easily be overcome with SALT and the world-class instruments that will be placed at the astronomer's command. This last chapter will be mostly devoted to recommendations regarding possible and highly likely, future studies of this nature using SALT (or any other larger telescope than the one used in this study), with a more widely extended choice and composition of sources. Overall, it can be stated with satisfaction that the original objectives were achieved.

Although good results were achieved with this study, ultimately one should aspire to address the following issues or limitations for optimal results:

- The first restriction experienced was that of the choice of sources, especially the limited choice of known BCGs visible from the southern hemisphere having a relatively high luminosity. With the advent of SALT, not only lower luminosity galaxies but higher redshift galaxies will be within the astronomer's reach. Higher redshift galaxies will bring new study opportunities for example the Lyman-α line which will occur in the visible region for galaxies with $z = 1.6$ to 2.3. The possibility of an extensive southern hemisphere deep survey of BCGs also exists.

- During observations it was not possible to change the orientation of the spectrograph slit (for example to place the slit along the major or minor axes of an object). Controlled slit placement is very important because there exists spacial inhomogeneities, for example large temperature gradients, across nebulae. In order to study these inhomogeneities, a long slit can be used with sections of data grouped together during the spectral extraction process. Ideally multiple slits should be used to map physical properties across the nebula.

- Background subtraction proved impossible in the case of the galactic H II regions, where the objects extended throughout the whole slit. Limitations of the acquisition camera prevented sky spectra, without influences of other objects, to be taken in the region of the concerned sources. Thus instrumental enhancements, as well as controlled slit placement will simplify this matter.

- Stellar Balmer absorption can also be restricted (in emission-line studies) by carefully executed slit placements. In any case, the proposed methods to eliminate the effects of the underlying stellar absorption (briefly mentioned in section 2.2.2) should be investigated in detail and developed further.

- The reddening correction was executed under the assumption that all of the extinction occurred outside of the BCGs. As stated before, the distribution of dust in these galaxies might well be irregular, thus the assignment of a single value for the extinction, as was done in this project, is only a first approximation. Consequently, it can be interesting to check how conclusions reached from analysis of nebular spectra

are dependent upon the assumption about the location of the dust in the line of sight. Dust may be approximated to be entirely in front of a nebula (as in this study), in which case the line emission is attenuated exponentially with optical depth. Alternatively, dust may be approximated to be mixed uniformly with the emitting gas. The solution of the equation of radiative transfer then links the attenuation of line emission to the total optical depth throughout the nebula. Different extinction laws should also be investigated for each different scientific study in order to find the law most suited to each particular case. Apart from the interactive measurements made of the emission lines and the unknown stellar Balmer absorption, the reddening correction procedure introduced the largest uncertainty in the results of this study. The uncertainty in the measured results can also be reduced by fitting a Gaussian function on all of the emission lines and not just on the lines that were blended with each other.

- Very good results were obtained with the measured Doppler shifts, but even these can be improved by refining the dispersion of the grating used in the spectrograph. There exists a tradeoff between the resolution of the spectrograph, the wavelength range it is capable of and the exposure time.

- The weak, but very important [O III]λ4363 line is easily lost in the noise even for moderately low metallicity galaxies and cannot be detected at all in high metallicity galaxies. This line is very important for temperature determination, and thus for abundance determinations. Where possible extra care should be taken to observe this line in order to avoid using the empirical methods instead of the direct method, as the precision of the empirical methods is no better than $0.2 - 0.3$ dex in the determination of oxygen abundance (Izotov & Thuan 1999). It might also be useful to consider other temperature sensitive diagnostic line ratios, such as the [N II] I($\lambda\lambda$6548,6583)/I(λ5755) ratio, which might be more accessible in a particular case. In many cases it will still be impossible to avoid using the empirical methods therefore, the discrepancies between the different methods should be thoroughly investigated and where possible eliminated.

- The temperature sensitive diagnostic line ratio that was used in this study has an ionisation potential that falls in the medium-zone, while the density sensitive diagnostic line ratio has a low ionisation potential. The ideal situation would consist of the case where a temperature and a density diagnostic ratio can be measured for each of the three (low,

medium and high) zones. This will result in a proper model of the ionisation and physical properties of the nebula. The ionisation potentials of some of the popular diagnostic line ratios are shown in Tables 4.18 and 4.19. From these tables it can be seen that, to achieve this, a very broad wavelength range is needed in the spectra. Some of the lines such as those needed for the high-ionisation density ratio ([Ne IV] I(λ2423)/I(λ2425)) only occur far into the UV region, which is a totally different endeavour to obtain. In addition, a very good signal-to-noise ratio and spectral resolution will be needed, and the high-ionisation zone, in particular, calls for very hot stars to be present in the nebula (for example: 63.5 eV photons are required to ionise Ne^{+2} to Ne^{+3} to obtain the lines needed for the above mentioned density diagnostic). Therefore, astronomers should not be blinded by this limitation, but should still attempt to use the most representative line ratios that can be detected.

- From the spectra presented in this study, it can be seen that the noise increased towards the shorter wavelength end of the spectra. Fortunately, SALT is ideally suited to do very high quality spectroscopy in this UV region (from 3200 Å), which means it will be possible to differentiate between the large number of lines occurring in this region, such as the higher order Balmer lines. With SALT, the 4000 Å Balmer break, which contains information about the stellar population and metallicity of a galaxy, will easily be attainable.

- Lastly, more observable sources in a study of this kind will bring a whole lot more nebular analysis opportunities. A small sample of five BCGs is not statistically viable for the application of some of the analysis tools such as the drawing of different diagnostic diagrams.

In summary, there is no fixed set of lines with which a full nebular analysis, without any deviation, can be performed. A very insightful and useful nebular analysis can already be attempted with only the very basic strong emission lines available. The above mentioned recommendations, as well as the methods discussed in this study are flexible to a certain extent. There exists definite guidelines to be followed, for example to try to obtain the highest signal-to-noise ratio possible. However, if a particular important line, such as the [O III]λ4363 line, is absent during observations, only limited changes can be made to the experimental set-up. For example, the grating can be changed to produce better resolution, however if the particular line is still absent, then there exists a very good reason for that. Thus, one should not expect or attempt to obtain spectra with a fixed set of lines necessary

for a full nebular analysis. Each emission line, whether it is by its relative strength or even by its absence, contains important information.

Nebular analysis is neither a fixed, nor a finalised procedure with spectra as input and physical properties as output. Each assumption and step in the process should be carefully reflected on and then adapted to suit the particular need(s) of the research program in order to obtain optimal results. The methods used and manner of application, will depend on the specific scientific study requirement. Every study, and each type of source researched will bring its own set of unparallelled challenges.

Bibliography

[1] Aladin Sky Atlas [Web:] http://aladin.u-strasbg.fr/AladinPreview [Last date of access: 13 Oct. 2005]

[2] Ali, B., Blum, R.D., Bumgardner, T.E., Cranmer, S.R., Ferland, G.J., Haefner, R.I., & Tiede, G.P. 1991, PASP, 103, 1182

[3] Aller, L.H. 1984, Physics of Thermal Gaseous Nebulae (Dordrecht: Reidel)

[4] Atomic Line List v2.04 [Web:] http://www.pa.uky.edu/~peter/atomic/ [Last date of access: 29 Aug. 2005]

[5] Baldwin, J.A., Phillips, M.M., & Terlevich, R. 1981, PASP, 93, 5

[6] Barnes, J. 1993, A Beginner's Guide to Using IRAF Version 2.10, Central Computer Services, NOAO

[7] Cardelli, J.A., Clayton, G.C., & Mathis, J.S. 1989, ApJ, 345, 245

[8] Carnochan, D.J. 1986, MNRAS, 219, 903

[9] Carter, B.J., Fabricant, D.G., Geller, M.J., Kurtz, M.J., & McLean, B. 2001, ApJ, 559, 606

[10] Cloudy: Simulation Code [Web:] http://www.nublado.org/older/c90.htm [Last date of access: 19 Sept. 2005]

[11] Cu/Ar Spectral Atlas from the NOAO Digital Library [Web:] http://www.noao.edu/dpp/library.html [Last date of access: 24 Aug. 2005]

[12] De Pree, C.G., Nysewander, M.C., & Goss, W.M. 1999, AJ, 117, 2902

[13] De Robertis, M.M., Dufour, R.J., & Hunt, R.W. 1987, Journ. R. Astron. Soc. of Canada, 81, 195

[14] Dinerstein, H.L. 1990, The Interstellar Medium in Galaxies, ed. Thronson, H.A. & Shull, J.M. (Dordrecht: Kluwer)

[15] Dopita, M., & Sutherland, R. 2003, Astrophysics of the Diffuse Universe (Canberra: Springer)

[16] Dyson, J.E., & Williams, D.A. 1997, The Physics of the Interstellar Medium (Bristol: IoP Pub)

[17] Emerson, D. 1997, Interpreting Astronomical Spectra (England: John Wiley & Sons)

[18] ESO Optical and UV Spectrophotometric Standard Stars list (2002) [Web:] http://www.eso.org/observing/standards/spectra [Last date of access: 24 Aug. 2005]

[19] Garnett, D.R. 1990, ApJ, 363, 142

[20] Gil de Paz, A., Madore, B.F., & Pevunova O. 2003, ApJ, 147, 29

[21] Gordon, D., & Gottesman, T.S. 1981, AJ, 86, 161

[22] Haro, G. 1956, Bol. Obs. Tonantz. Tacub, 2, 14, 8

[23] Howell, S.B. 1992, Astronomical CCD Observing and Reduction Techniques (California: Astron. Soc. of the Pacific Series, 23)

[24] Izotov, Y.I., & Thuan, T.X. 1999, ApJ, 511, 639

[25] Jansen, R.A., Fabricant, D., & Franx, M. 2001, ApJ, 551, 825

[26] Kaler, J.B. 1989, Stars and their Spectra (Cambridge: Cambridge University Press)

[27] Kewley, L.J., & Dopita, M.A. 2002, ApJS, 142, 35

[28] Kitchen, C.R. 1995, Optical Astronomical Spectroscopy (Bristol: IoP Pub)

[29] Kobulnicky, H.A., Kennicutt, R.C., & Pizagno, J.L. 1999, ApJ, 514, 544

[30] Kong, X., & Cheng, F.Z. 2002a, A&A 389, 845

[31] Kong, X., Weiss, A., Charlot, S., & Cheng, F.Z. 2002b, A&A 396, 503

[32] Kong, X., Weiss, A., Charlot, S., & Cheng, F.Z. 2003, A&A 403, 877

[33] Kong, X. 2004, A&A 425, 417

[34] Kunth, D. & Östlin, G. 2000, A&ARv 10, 1

[35] Lee, H., Grebel, E.K., & Hodge, P.W. 2003a, A&A, 410, 141

[36] Lee, H., McCall, M.L., Kingsburgh, R.L., Ross, R., & Stevenson, C.C. 2003b, AJ, 125, 146

[37] Lee, H. & Skillman, E.D. 2004, ApJ, 614, 698

[38] Markarian, B.E. 1967, Astrofizika, 3, 55

[39] Massey, P. 1997, A User's Guide to CCD Reductions with IRAF, Central Computer Services, NOAO

[40] Massey, P., Valdes, F., & Barnes J. 1992, A User's Guide to Reducing Slit Spectra with IRAF, Central Computer Services, NOAO

[41] McCall, M.L., Rybski, P.M., & Shields, G.A. 1985, ApJS, 57, 1

[42] McGaugh, S.S. 1991, ApJ, 380, 140

[43] McLean, I.S. 1997, Electronic Imaging in Astronomy: Detectors and Instruments (England: Wiley-Praxis Ser. in Astron. & Astrophys, John Wiley & Sons)

[44] Osterbrock, D.E. 1989, Astrophysics of Gaseous Nebulae and Active Galactic Nuclei (Mill Valley, CA: University Science Books)

[45] Pagel, B.E.J. 1997, Nucleosynthesis and Chemical Evolution of Galaxies (Oxford: Cambridge University Press)

[46] Pagel, B.E.J., Edmunds, M.G., Blackwell, D.E., Chen, M.S., & Smith, G. 1979, MNRAS, 189, 95

[47] Peña, M., Ruiz, M.T., & Maza, J. 1991, A&A, 251, 417

[48] Pilyugin, L.S. 2000, A&A, 362, 325

[49] Pilyugin, L.S. 2001, A&A, 369, 594

[50] Rosa-González, D., Terlevich, E., & Terlevich, R. 2002, MNRAS, 332, 283

[51] Shaw, R.A., & Dufour, R.J. 1995, PASP, 107, 896

[52] Shi, F., Kong, X., Li, C., & Cheng, F.Z. 2005, A&A, 437, 849

[53] Shu, F.H. 1982, The Physical Universe (California: University Science Books)

[54] Simbad Astronomical Database. [Web:] http://simbad.u-strasbg.fr/Simbad [Last date of access: 13 Sept. 2005]

[55] Stasińska, D., Schaerer, D., & Leitherer, C. 2001, A&A, 370, 1

[56] Taylor, R.J. 1994, The Stars: their structure and evolution (Cambridge: Cambridge University Press)

[57] Terlevich, R., Melnick, J., Masegosa, J., Moles, M., & Copetti, M.V.F. 1991, A&A Suppl. Ser. 91, 285

[58] Veilleux, S., & Osterbrock, D.E. 1987, ApJ, 63, 295

[59] Zaritsky, D., Kennicutt, R.C., & Huchra, J.P. 1994, ApJ, 420, 87

[60] Zwicky, F. 1965, ApJ, 142, 1293

[61] Zwicky, F. 1966, ApJ, 143, 192